Methodologies for Design-Oriented Electromagnetic Modeling of Planar Passive Power Processors

Anish Prasai

Thesis submitted to the faculty of the Virginia Polytechnic Institute and State University in partial fulfillment of the requirements for the degree of

MASTER OF SCIENCE

in

Electrical Engineering

Dr. Willem G. Odendaal, Chair/Advisor

Dr. Dushan Boroyevich

Dr. Jaime de la Ree

July 5, 2006
Blacksburg, Virginia

Keywords: planar transformer, planar core, planar windings, high frequency, core losses, winding losses, winding capacitances, leakage inductance, cross-coupling, electromagnetic radiation, multiple windings, analytical modeling, shield design, finite element modeling, electroplating, sputtering

Methodologies for Design-Oriented Electromagnetic Modeling of Planar Passive Power Processors

Anish Prasai

ABSTRACT

The advent and proliferation of planar technologies for power converters are driven in part by the overall trends in analog and digital electronics. These trends coupled with the demands for increasingly higher power quality and tighter regulations raise various design challenges. Because inductors and transformers constitute a rather large part of the overall converter volume, size and performance improvement of these structures can subsequently enhance the capability of power converters to meet these application-driven demands. Increasing the switching frequency has been the traditional approach in reducing converter size and improving performance. However, the increase in switching frequency leads to increased power loss density in windings and core, with subsequent increase in device temperature, parasitics and electromagnetic radiation. An accurate set of reduced-order modeling methodologies is presented in this work in order to predict the high-frequency behavior of inductors and transformers.

Analytical frequency-dependent expressions to predict losses in planar, foil windings and cores are given. The losses in the core and windings raise the temperature of the structure. In order to ensure temperature limitation of the structure is not exceeded, 1-D thermal modeling is undertaken. Based on the losses and temperature limitation, a methodology to optimize performance of magnetics is outlined.

Both numerical and analytical means are employed in the extraction of transformer parasitics and cross-coupling. The results are compared against experimental measurements and are found to be in good accord. A simple near-field electromagnetic shield design is presented in order to mitigate the amount of radiation.

Due to inadequacy of existing winding technology in forming suitable planar windings for PCB application, an alternate winding scheme is proposed which relies on depositing windings directly onto the core.

To my parents,

For their love, support, and guidance.

ACKNOWLEDGMENTS

First and foremost, I would like to thank my advisor, Dr. Willem G. Odendaal, who has been there to advise me since the start of my Electrical Engineering study. I took my first undergraduate class in electrical circuits under him, and it was under his tutelage that I began one of my first research projects as an undergraduate student. He was then kind enough to take me under his wings and put me in a position as one of his graduate students, providing me with a priceless opportunity to work with one of the most celebrated research groups. As one of his students, I have learned a great deal about the qualities necessary to be a good research engineer and subsequently, how to conduct great research. His innate ability as a visionary is only surpassed by his intelligence in realizing the vision. So I am in eternal gratitude to Dr. Odendaal for providing me with a nest, a wing and a compass as I begin my career as a research engineer.

I would like to thank the rest of my committee members, comprising of Dr. Dushan Boroyevich and Dr. Jaime de la Ree. Dr. Boroyevich played a crucial role in introducing me to the world of power electronics as an undergraduate and graduate student. His larger-than-life personality combined with excellent communicating skills made learning about power electronics that much more interesting. My broad knowledge and understanding of power electronics converters can be attributed to his excellent teaching abilities. Many thanks goes out to Dr. de la Ree for igniting the spark inside me that is fast becoming a conflagration in the field of Power. His strong interest in academic well being of his students is only paralleled by few others. Very few other professors have the flawless skill in holding their students in such a consistent rapture, class after class, over learning about something as technically mundane as power with a chalk in one hand and his belt in another.

A big thank you goes out to Dr. Zhenxian Liang and Dr. J.D. van Wyk for providing expert advice during my struggle in tackling the monster that is the packaging technology. Many thanks goes out to the rest of the faculty and staff members of CPES, including Dan Huff, Bob Martin, Marianne Hawthorne, Jamie Evans, Beth Tranter, Trish Rose, Michelle Czamanske, Linda Long and Rolando Burgos. My technical and non-technical interactions with them on the daily basis

have facilitated the completion of my research and enriched my experience here in CPES.

I have perhaps learned the most from my fellow students and colleagues. Much of the success that is enjoyed by CPES can be attributed to the close ties that students have in teaching and helping each other. So, many special thanks goes out to Ning Zhu, Carson Baisden, Chucheng Xiao, Jing Xu, Yian Liang, Wenduo Liu, Tim Thacker, Callaway Cass, Arman Roshan, Jerry Francis, Andy Schmit, Parag Kshirsagar, David Lugo, Daniel Ghizoni, Bryan Charboneau, Sabastian Rosado, David Reusch and Luisa Coppola. Without their help, I would be re-inventing the wheel countless number of times.

I would like to thank my parents for their constant support of my multiple endeavors. I find myself very fortunate in that I grew up in a household where I had the freedom to pursue anything that I wanted. When one is given that kind of freedom, there is no height that is unreachable. For this, I am truly grateful.

Finally, I would like to thank Dr. Boris Jacobson of Raytheon for funding the project that has made this work possible.

This work made use of Engineering Research Center Shared Facilities supported by the National Science Foundation under NSF Award Number EEC-9731677 and the CPES Industry Partnership Program. Any opinions, findings and conclusions or recommendations expressed in this material are those of the author and do not necessarily reflect those of the National Science Foundation.

This work was conducted with the use of Maxwell 2D/3D, donated in kind by Ansoft Corporation of the CPES Industry Partnership Program.

TABLE OF CONTENTS

LIST OF TABLES

LIST OF FIGURES

Chapter 1
Introduction

1.1 Planar Power Processors

The advent and proliferation of planar technologies for power electronic converters are driven in part by the overall trends in analog and digital electronics [1]. These trends coupled with the demands for increasingly higher power quality and tighter regulations raise various design challenges. Because inductors and transformers constitute a rather large part of the overall converter volume, improvement of these structures can subsequently enhance the capability of power converters to meet these application-driven demands. Improvements are realized by designing these passive magnetic devices to attain higher power density and efficiency [1, 2, 3, 4, 5, 6, 7, 8, 9, 10].

The traditional mean to achieve higher power density and efficiency has been by increasing the switching frequency of the power electronic converters. The capability to push frequency higher in converters has been made possible by improvements in enabling technologies such as power semiconductor devices, materials, circuit and control techniques, integration and thermal management techniques.

The continuous increase in frequency has usually been taken to imply continuous decrease in the physical dimension of the converters. In theory, this is essentially true as less energy is stored in a given switching cycle, resulting in reduction of the size and the volume of the primary electromagnetic energy storage elements. Over the last two decades, this implication has been proven to be undeniable as demonstrated by the size evolution of telecom. power modules in Fig. 1.1 [1].

However, the frequency can only be pushed so far before encountering reduction in the power density-frequency product in the electromagnetic energy storage elements as portrayed in Fig. 1.2 [11]. The eventual decline encountered as the frequency is raised beyond a certain optimal point in inductors and transformers is attributed to increased losses due to eddy current effects and hysteresis, and limitations of the currently available materials [12, 13, 1]. The losses convert to heat through an electro-thermal phenomenon known as the Joule's effect or the Joule's law[14], raising the temperature of the device. Since material properties are a function of the temperature, the proper operation of a device is critically dependent

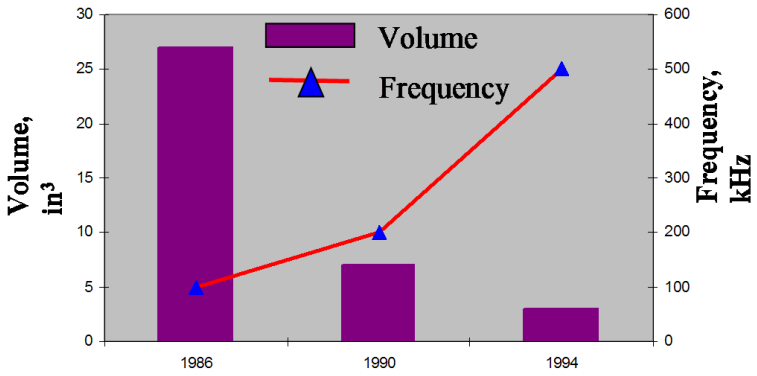

Figure 1.1: The size evolution of DC/DC Telecom. Power Units.

on not exceeding a certain temperature threshold of the material. Increased degradation of material properties are also encountered as a function of frequency. For example, the permeability of ferromagnetic materials decreases significantly beyond a certain frequency, as portrayed by complex permeability plots given in most ferrite datasheets. Further, the increase in frequency also results in heightened parasitics and electromagnetic radiation. So, it is critical to know just how far the frequency can be pushed before the various drawbacks overwhelm the desired benefits.

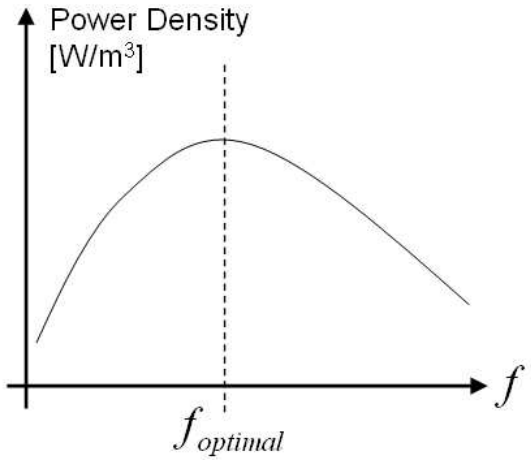

Figure 1.2: The impact of frequency on power density.

Planar structures have been studied extensively since the 1960's in an effort to understand what measures can be taken to overcome the mentioned design challenges [7, 10, 8, 13, 12]. One such measure is to use planar windings to minimize eddy current losses and provide a better control over parasitics, in comparison to

round conductors [15, 16, 17, 18]. In addition, the structural nature of planar devices, compared to standard magnetics, introduces larger surface area to volume ratio, subsequently facilitating in quicker extraction of heat. So attainment of higher power density in planar devices can also be achieved through improvements in thermal management and packaging technology [13, 5, 19, 8, 20].

1.2 Types of Planar Magnetics

There are essentially three types of planar magnetic structures in power conversion applications that employ ferromagnetic cores for flux channeling. The first two types are mentioned in [8] and the third one introduced in [21]. The three types of planar magnetic structures are:

1. Disk-type structure
2. Tube-type structure
3. Vertical-wound structure

The disk-type structures, shown in Fig. 1.3, are generally created by stacking together planar, disk-like dielectrics and windings that are then encapsulated or enclosed by E, C and/or I type cores. In tube-type structures, shown in Fig. 1.4, the windings are wrapped around the core, similar to how standard inductors and transformers are built. In the vertical-wound structure, the planar windings are vertically wrapped around the inner core leg as shown in 1.5.

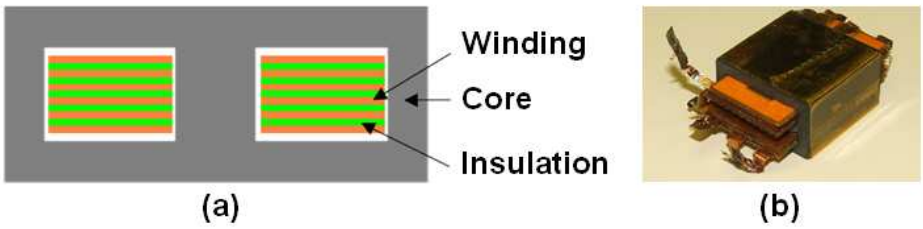

Figure 1.3: Disk structure with the windings encapsulated by the core where, a) typical cross-section view, b) example structure.

The disadvantages of disk-type structures are that 1) the heat generated by the conductors has to diffuse through the core to reach the ambient environment or the heat sink, and 2) significant inter-winding capacitances are developed due to large layer-to-layer contact surface area and small separation distance. Although

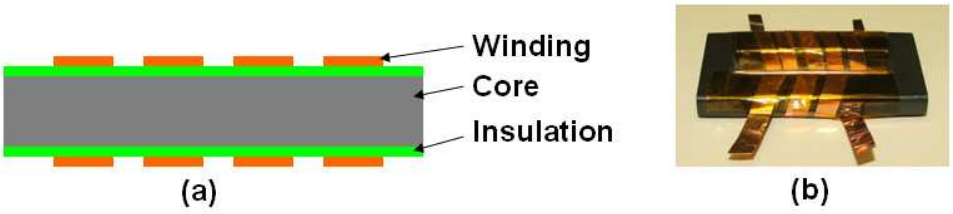

Figure 1.4: Tube structure with the core encapsulated by the windings where, a) typical cross-section view, b) example structure.

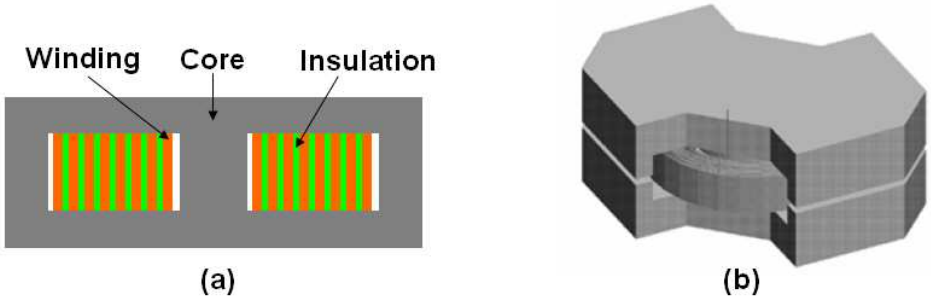

Figure 1.5: Vertical-wound structure with the windings wrapped around the inner leg where, a) typical cross-section view, b) example structure.

there are ways to minimize inter-winding capacitance, there is no practical and feasible method to deal with the problem of extracting heat more efficiently with this structure. As the power-frequency product of the device is pushed, the windings encounter increased ohmic losses due to eddy current effects, effectively generating greater amount of heat [13]. The heat, in turn, diffuses through the core of usually very low thermal conductivity and unnecessarily raises the core temperature, causing fluctuations of the core properties and limiting attainment of higher power density.

The tube-type structures effectively deal with the thermal management issue raised by the disk-type structures. The device can dissipate heat quicker with the windings located external to the core and directly exposed to the ambient environment or a heat sink. Tube-type design also offers higher power density, efficiency and lower profile in comparison with disk-type design as indicated by Fig. 1.6 [8]. One of the reasons for higher power density is that the tube structures can achieve a lower profile because the core can be relatively thinner than the cores of the disk-types. Inter-winding capacitances are also generally smaller.

However, the tube-type structure is not without its share of problems. The exposed windings create leakage flux that tend to couple with adjacent devices,

creating additional losses, raising temperature, and introducing noise. This issue is not as significant in the disk and the vertical-wound structures because the core also acts as a shield for magnetic fields. Thus, in order to confine the leakage flux as close to the structure as possible for the tube-types, electromagnetic shielding becomes a necessity [8, 22, 23].

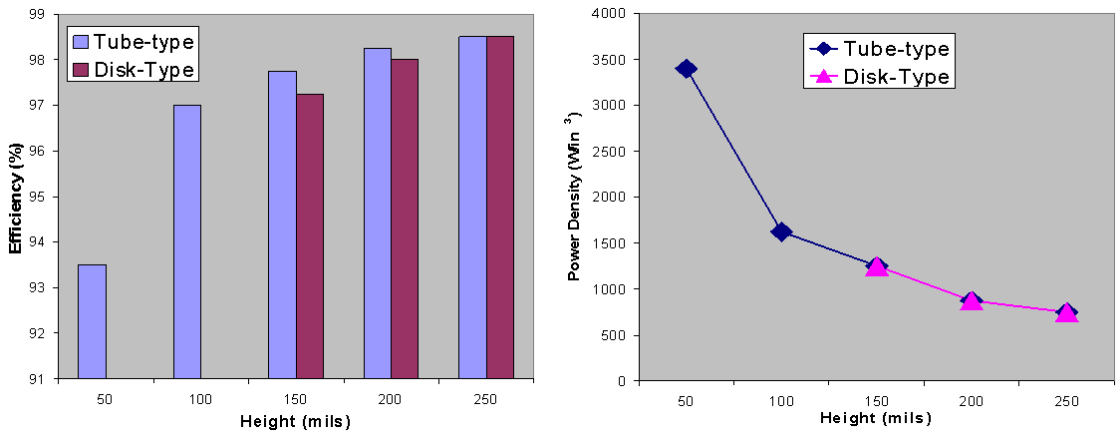

Figure 1.6: Power density/efficiency vs. height for 50 W transformer (foot-print = 0.5 in^2) at 1 MHz.

The vertical-wound structure faces similar problems as the disk-type, but due to the planar windings being vertical, the structure experiences a reduced thermal gradient from top to bottom. The reduced thermal gradient allows the structure to achieve higher power density in comparison to disk-types (approx. 1800 W/in^3 as announced in [21]). However, due to a current density requirement in the windings, as mandated by the power level of the application, the height of the profile cannot be lowered beyond a certain dimension. Thus, vertical-wound structures cannot compete as well with the tube-types in achieving the highest power density.

The primary focus of this work will be on the tube-type planar transformers. A tube-type structure is selected due to its capability in achieving higher power density, lower profile and better thermal management in comparison to the other two structures. Further, the planar tube-type structures have not been studied as extensively in literature.

1.3 The Need for Accurate Modeling

Modeling is an imperative step in any engineering design project. It ensures that the device being realized will behave and perform as desired. Modeling also

allows a designer to ascertain the level of impact and interaction a device has on rest of the system. The predicted behavior and performance of the design makes it possible to employ clever techniques, in a cost-effective fashion, earlier in the development cycle in order to design out potential problems that might become apparent through modeling.

In the beginning of a device's development cycle, there are plenty of available techniques to solve potential issues. But as the device is taken further down the development cycle, amount of techniques to solve the same set of problems progressively decays. Simultaneously, the designer is confronted with increase in cost to solve the same set of problems, as they appear, through other 'brute-force' means. Such a trend is depicted in Fig. 1.7 [22]. So, accurate modeling is critical in identifying and solving issues during the initial design phase in order to lower overall development cost. Further, accurate prediction of the high frequency behavior and the performance of the planar, tube-type magnetics is only achieved through development of good models.

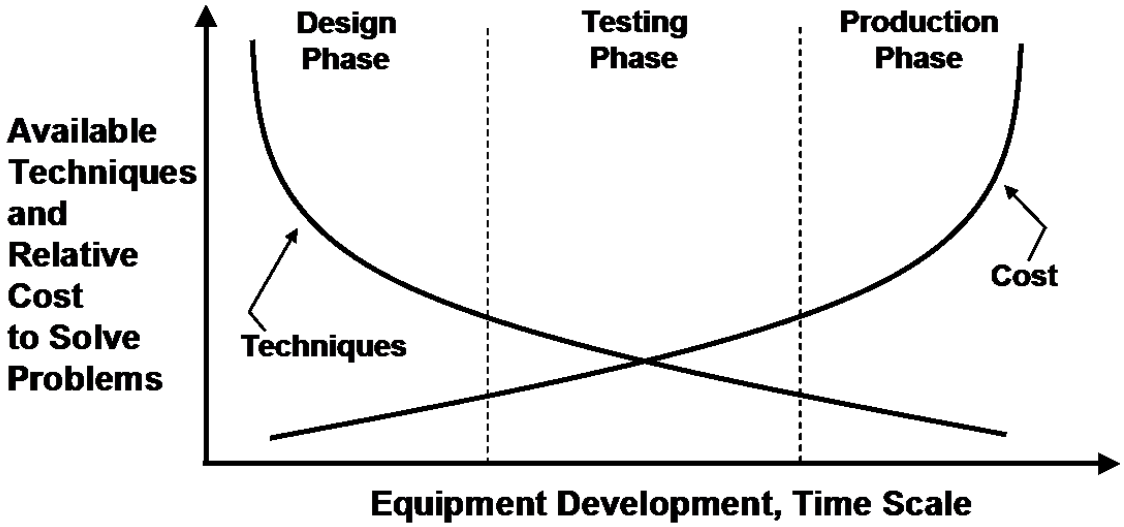

Figure 1.7: The amount of techniques available and the cost to solve problems as the device progresses down a development cycle.

1.4 Previous Work

The transformer is one of the most widely used components in power processing applications, yet it is one of the most difficult devices to model accurately. Much of the work in modeling of the transformers can be grouped into two broad categories:

1. **White box modeling**. The model is derived based upon electromagnetic field distribution so information regarding the internal layout and fabrication of the transformer must be known. Analytical and numerical modeling are primarily used in deriving this type of model. The approximations that are often made in order to reduce the order of complexity limits the analysis to certain types of transformers. This type of modeling allows a designer to predict device behavior before the device is even built.

2. **Black box modeling**. The model is acquired based on terminal behavior of the transformer. An equivalent circuit is used to model the transformer whose parameters are extracted experimentally through methods such as the classical open and short circuit tests. This type of modeling is more popular than white box as the methodologies in deriving the models are applicable to wider variety of transformers. However, the modeling requires a prototype to be available.

The accuracy of equivalent circuit models of a transformer given in [24] and other introductory textbooks are only valid at a single frequency for which the parameters are extracted at through the black box approach. In order to model a transformer accurately for a range of frequency, both frequency-dependence and non-linearity of the core and windings have to be taken into account, which are lacking from the classical transformer models. The means to predict the effect of distributed stray capacitances due to time-varying electric fields along the windings are also missing. Further, the models do not extend very well to take into account the effects of cross-coupling in multi-winding transformers.

In order to overcome the limitations of the classical models, extensive amount of literature have been written discussing how to model transformers more accurately.

A widely popular method to extract the frequency-dependent non-linearity of a core material through experimental means is described in [25]. The measurements are ideally performed on a very thin, toroidal core such that dimensional effects are not significant and the flux distribution through the core is as uniform as possible. The non-linear model can then be used for any inductor or transformer model utilizing the same core material, irrespective of the structural geometry. The capacitance-permeance model developed in [26, 27] is utilized in order to electrically represent the non-linearity.

At high frequency, due to the development of time-varying electric fields along the windings, external to the conduction path, the winding impedance is best represented with capacitances distributed in a manner similar to transmission lines. Significant amount of work have been done to model this high frequency winding impedance in [28, 29, 30, 27, 31]. These models have proved to be sufficiently accurate in predicting high frequency behavior but the derivation of these models are quite rigorous and complex.

A transformer model is described in [32] that accurately models the nonlinearity of the core through the capacitance-permeance analogy while using a simple equivalent circuit, extracted experimentally, to model the winding impedance. Although a way to connect multiple windings through the use of Tellegen gyrator [33] is inferred, there is no comment made on extending the model to include cross-coupling among the windings.

The classical cantilever model is extended to take into account the cross-coupling between windings in a multi-winding transformer in [34]. Another multi-winding transformer model is developed in [35] that is derived based on geometric distribution of the magnetic flux. However, both of the equivalent circuits only model the reactive behavior of the transformer and do not take into account various losses that are simultaneously taking place in both the windings and the core.

Losses due to eddy currents increase rapidly with frequency in transformers. One of the first notable work on the eddy current effects in transformers is written by Dowell in [36]. Subsequent papers were written that further broadened the knowledge base in [37, 38, 39]. Significant break-through in eddy current analysis was obtained for planar windings when Ferreira decoupled the individual impact of skin- and proximity-effect by recognizing them to be orthogonal to each other in [40, 41].

From all these papers, there is a certain knowledge gap that is starkly apparent. What is missing is a set of simpler methodologies to accurately model high-frequency, multi-winding transformers including both losses and cross-coupling via utilization of analytical and numerical tools. The emphasis is made on white-box type modeling in this work because it offers a way to model a transformer before it is ever built and realized, based simply on the structural specification of the device.

1.5 Aims of This Study

In an effort to fill the knowledge gap brought on by the lack of simple and accurate white-box modeling, this work attempts to present a set of dynamic higher-order methodologies in modeling of planar, multi-winding, tube-type magnetics in order to accurately predict device characteristics and performance. The models are limited to planar, foil type windings. The model parameters are extracted through both analytical and numerical means. The accuracy of the analytical and numerical results are compared, when appropriate, with experimental measurements.

1.5.1 Choosing the Right Modeling Tool

The choice between analytical or numerical tool greatly depends on the design priority; whether speed or accuracy is the prime factor in selecting the appropriate tool. For the complex structures as the one studied in this work, analytical expressions describing the field distribution exactly are all too complex and impractical. Thus reduced order models with various approximations are often employed to derive the analytical models. But as a result of reducing the order of complexity, some error is introduced.

Numerical tools such as finite element modeling (FEM) are able to model even the most complex structures and provide very accurate results, but at the cost of long simulation time and overhead time required to draw the models and set up the simulation parameters accurately. There is also a learning curve for individuals who do not have a strong background in use of such software. So, while very accurate results are obtained, the time to acquire them is significantly longer than analytical methods.

So FEM is the prime tool when accuracy is the highest priority. However, for designers who are willing to sacrifice bit of accuracy in order to maximize on speed, analytical tools are the more suitable choice. Thus, as portrayed in Fig. 1.8, the choice of modeling tool greatly depends on what is most important to a designer: accuracy or speed.

1.5.2 Chapter 2: Frequency-Dependent Modeling

Background information on issues and phenomena that are apparent in high-frequency transformers are briefly outlined. Analytical and numerical means in calculating winding losses due to eddy currents are outlined. Classical analytical

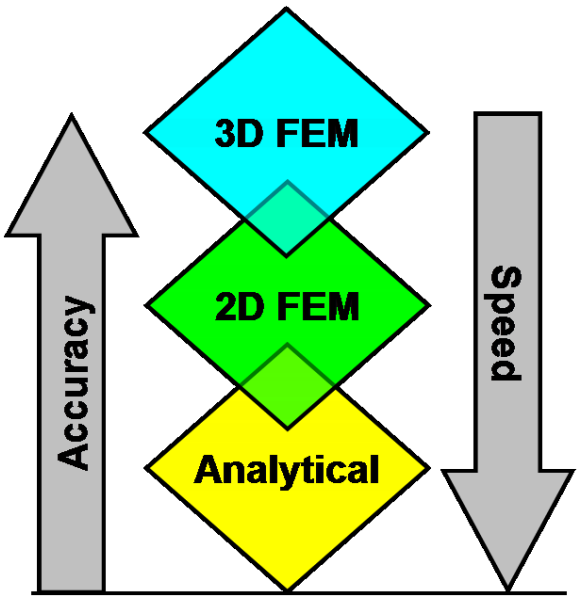

Figure 1.8: The prioritization between speed and accuracy in choice of modeling tool.

tools are described for core loss calculations. Sensitivity of magnetic material properties to machining process, core structure and frequency of excitation is outlined and a means to determine the proper relative permeability of a core is described. Appropriate thermal modeling is critical in identifying maximum temperature gradients in a device such that appropriate measures can be taken in order to ensure that the temperature does not exceed material limitations. A simple 1-D thermal modeling is described to predict the maximum temperature of a transformer. The various losses raise temperature and degrade device performance, so a methodology to optimize the performance of passive magnetic devices is presented.

1.5.3 Chapter 3: Modeling of Electrodynamics

Due to the shapes of the windings, the high frequency magnetic fields present, and eddy current effects taking place in magnetics, a time-varying electric field exists along the windings. The time-varying electric fields induce what is known as 'displacement current' that exhibit a high frequency behavior equivalent to charge displacement taking place in capacitors. Thus, transformer winding impedances are often modeled with distributed capacitances similar to transmission lines. An analytical methodology is provided for calculating the inter-winding capacitance, and the results are compared with FEM and verified experimentally.

1.5.4 Chapter 4: Leakage Reactance and Cross-Coupling

Significant amount of magnetic coupling take place among the windings, and between the windings and adjacent devices. The former is the primary mode through which a transformer functions. The latter is due to leakage reactance. The magnetic flux contributing to the leakage reactances are one of the prime factors in performance degradation due to losses, and poor regulations. Both numerical and analytical methodologies are explored in modeling the reactive nature of a transformer. The results are verified with experimental measurements.

1.5.5 Chapter 5: Shield Design

One of the biggest drawbacks of structures with the windings exposed to the environment is the introduction of electromagnetic radiation. Large leakage flux can couple with the adjacent devices leading to increased losses, overheating, and introduction of noise in the circuit. Thus electromagnetic shielding becomes a necessity in order to mitigate the level of coupling. A simple near-field electromagnetic shield design method is presented. The design is conducted from both magnetoquasistatic (MQS) and classical plane wave perspective. Several potential shield materials are studied and compared in terms of their shielding effectiveness and the additional losses that they might respectively bring about. FEM is used to study the losses encountered in the windings and shield for the different shield materials in order to acquire insight into the effectiveness of the shield and the shielding material. A potential shield structure is proposed based on the study.

1.5.6 Chapter 6: Directly Depositing Windings onto the Core

The use of planar tube-type magnetics poses some challenges in terms of the winding scheme because the mature 2-D planar manufacturing process enjoyed by the disk-type structures is not directly applicable to the 3-D tube-types. The current state-of-the-art winding schemes are described and their drawbacks are discussed. A new winding scheme is proposed in which the copper windings are directly deposited onto the core. A procedure for fabricating such a device using standard packaging lab equipment is outlined. Benefits of this winding scheme is described as well.

1.6 The Case Study: The Three-Winding Transformer

The three-winding tube-type planar transformer depicted in Fig. 1.9 is used as the case study for the modeling methodologies discussed in this work.

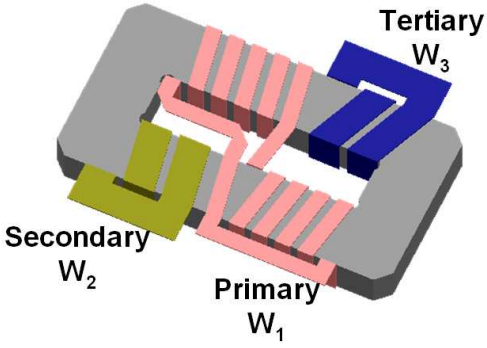

Figure 1.9: The three winding planar transformer used as the case study.

The dimensions of the core are depicted in Fig. 1.10. A soft ferrite, MnZn of type 3F45 manufactured by Ferroxcube, Inc., was chosen as the core material as this ferrite has demonstrated excellent high frequency performance in power applications [8, 42]. The inside corners are rounded to reduce thermo-mechanical stress caused by high (saturating) flux density. There are no air gaps present in this core.

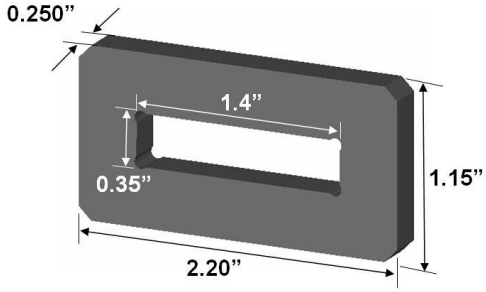

Figure 1.10: The dimension of the core under study.

The copper windings shown in Fig. 1.9 are 10 mils thick. The primary winding has a width of 100 mils. The secondary and tertiary windings have a width of 200 mils. Windings are interleaved in order to lower back EMF. Air separation of 2 mils is used as insulation between the copper windings and the ferrite core in the models. However, for experimental measurements, 2 mils thick Kapton tape or solder mask is utilized.

The transformer is rated to handle 10 A and 150 V on the primary with the first harmonic frequency of the input signal occurring at 750 kHz.

The three-winding transformer shown in Fig. 1.11 is used to experimentally verify the accuracy of numerical and analytical modeling.

Figure 1.11: The transformer used for experimental verification of the models.

Chapter 2
Frequency-Dependent Modeling

2.1 Introduction

Ideally, a modeling environment should be such that it can effectively emulate experimental measurements carried forth on an actual fabricated device. Advances in processor technology, speed, memory, and storage and subsequent availability of powerful computing resources at low capital cost have greatly facilitated the creation of modeling tools for a wide number of engineering disciplines, making it feasible to simulate and test products before they are ever created. In fact, it is now possible to simulate complex systems almost entirely, before any construction is attempted. Such an attempt was made for the new all-electric Boeing 787 Dreamliner. However, even with these advancements, the number crunching ability of most consumer-end computers are still limited for certain types of computing intensive numerical problems and thus cannot simulate the entire physical system with all its complexity. In Chapter 5, it will be shown how numerical analysis of eddy currents in a transformer shield fall under this category, of problems that quickly exceed processing limits.

Reduced order analytical modeling is employed in an attempt to optimize complexity, accuracy and speed during the iterative design process, where shorter design cycles are necessary. This chapter will present frequency-dependent modeling of transformers that provide computation of core and winding losses, model of thermal gradients due to these losses, and a methodology to optimize performance of passive magnetics. Discussions of high-frequency phenomena, and sensitivity of magnetic properties to electrical and physical parameters are also made.

Chapters 3 and 4 deal with frequency-independent reduced order modeling of transformer parasitics through the implementation of dedicated analytical tools and algorithms that can circumvent the drawbacks of the generic numerical tools.

2.2 High Frequency Effects

In an effort to gain insight into the results acquired through modeling, some understanding of the various high frequency effects that are taking place in the transformer is required.

Every attempt to increase power-frequency product have been faced with in-

creased losses that are primarily attributed to the effects of eddy currents [13]. Eddy currents are induced by the time-varying magnetic fields that are moving through a conductive medium and vice versa, as depicted in Fig. 2.1. The losses due to eddy currents in windings can be classified into five major categories [43]:

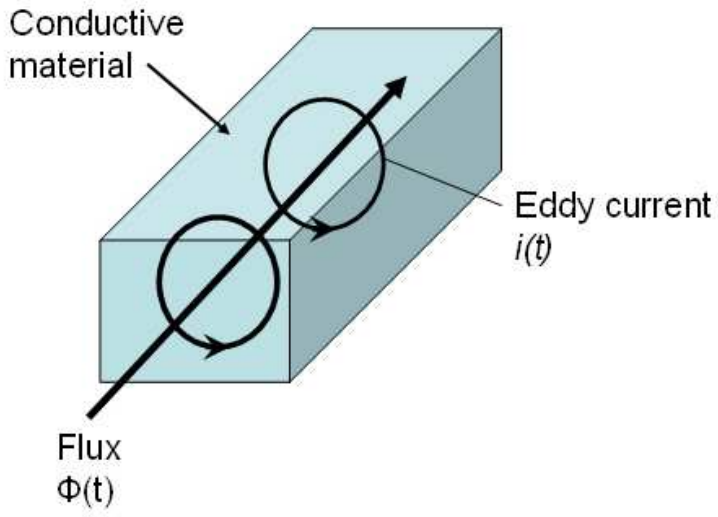

Figure 2.1: Eddy currents in a conductive material.

1. **Skin-effect**. The flow of sinusoidal current, $i(t)$, at a frequency, f, through a conductive medium results in current crowding at the surface of the medium. The current distributes in an exponentially decaying fashion with the distance away from the surface inside the medium with the characteristic *skin depth*, δ, defined in [44] as:

$$\delta = \frac{1}{\sqrt{\pi f \mu \sigma}} \tag{2.1}$$

The equation is an approximation of skin depth for good conductors with $\sigma >> 2\pi f\epsilon$. Skin depth is also a measure of the decay of the electromagnetic fields into the conductor. At a distance of one skin depth, the E or H field at the surface of the conductor has been reduced to 37% or $1/e$ of the original magnitude. Figure 2.2 depicts the skin depth of various materials as a function of frequency. The describing phenomenon of skin-effect is that the skin depth decreases with increasing frequency resulting in simultaneous increase

in winding resistance, known as AC resistance. The increase in winding resistance then leads to increased ohmic loss that manifests through elevated temperature in the conductors. However, the AC resistance is not solely due to the skin-effect as it is a combinatino of the other eddy current effects.

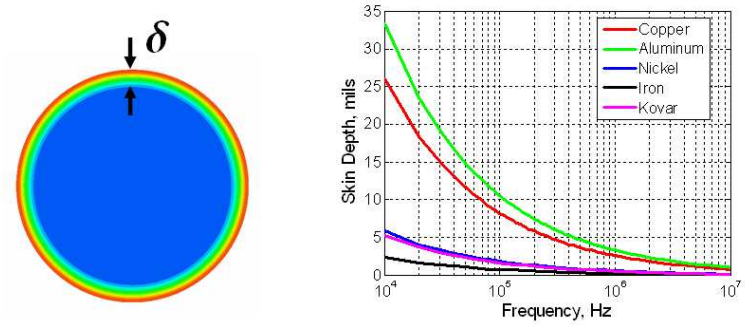

Figure 2.2: Skin depth of various conductors vs. frequency.

2. **Proximity-effect**. The phenomenon known as the proximity-effect is due to nearby high-frequency, current-carrying conductors that induce high frequency eddy currents in the conductor of interest, creating additional loss. A simple example of this effect is shown in Figure 2.3 that depicts the effect a high frequency current carrying conductor has on a piece of electrically open conductor sitting next to it [44]. The plot of current density is along the center line that goes from left to right on each of the conductors. The high frequency current, $i(t)$, in conductor A generates magnetic flux, $\Phi(t)$, between the two conductors. The flux, $\Phi(t)$, in turn induces current on the left surface of conductor B with a skin depth, δ. As the conductor is electrically open, the net current has to be zero. So a current of opposite magnitude is induced on the right surface of conductor B. As these induced eddy currents have no functional value in power magnetics, they serve only to create additional losses that needlessly heat up the material. Proximity-effects are dominant in multi-layer windings.

3. **End-Effects**. These effects are most commonly observed at the ends of transformer windings where the magnetic flux enter the conductor perpendicular to the flat planar surface of the windings, inducing losses and altering field distributions.

4. **Core Gap Effects**. Windings at the proximity of core gaps experience in-

creased losses. This is due to large eddy currents being induced by fringing fields that intersect the windings.

5. **Extraneous Conductor Effects**. This effect is similar to proximity effect in that a conductor with heavy current loading or high frequency current or both induce eddy current on a nearby conductive material, resulting in additional loss.

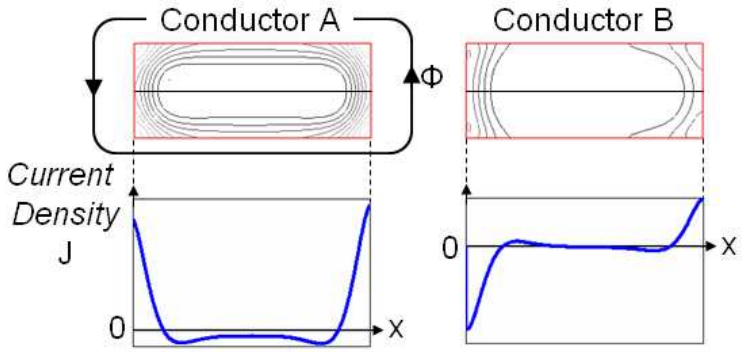

Figure 2.3: Current distribution due to proximity effect in two adjacent conductors.

Similar to windings, skin-effect is also observable in ferrite cores with relatively low resistivity. The relative high frequency for a given core cross-section decreases the skin depth, or *penetration depth*, effectively preventing magnetic fields from fully penetrating the core. The effective permeability of the core drops as the result of the core not being fully magnetized [42]. This phenomenon is partly responsible for the behavior shown in Fig. 2.4 that depicts the drop in complex permeability with increase in frequency. The subsequent increase in hysteresis loss in MnZn ferrites due to increase in frequency [45] is the other factor that reduces effective permeability. The eddy current effects and dimensional resonance of ferrite cores also cause additional power loss [42, 13], as demonstrated by Fig. 2.5.

2.3 Losses in a Flat Foil Winding

One dimensional method described in [13] is used in analyzing the eddy current losses in a flat foil winding. The losses and current distribution encountered at high frequency in a conductor is primarily due to skin- and proximity-effect. These two effect are decoupled due to the orthogonality principle observed by Ferreira in [40, 41]. So, in order to derive the total loss and overall current distribution in a

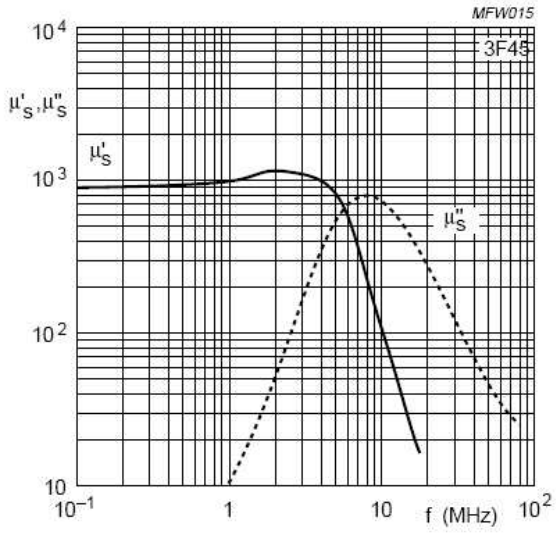

Figure 2.4: Complex permeability vs. frequency of 3F45 ferrite [46].

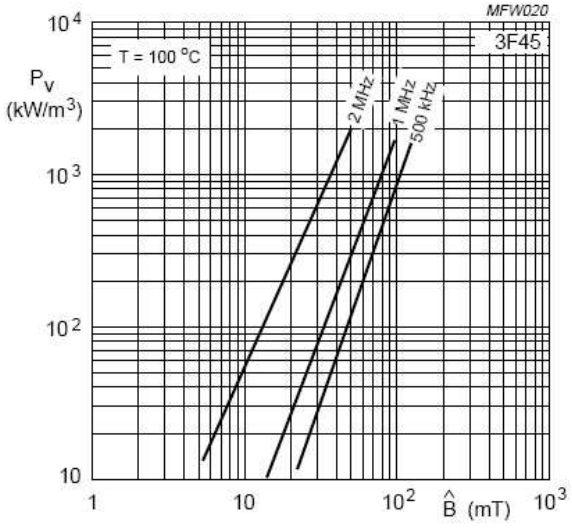

Figure 2.5: Power loss as a function of peak flux density with frequency as a parameter for 3F45 ferrite [46].

foil winding, the losses and current distribution for the two effects are calculated separately and then added together.

An isolated foil strip is shown in Fig. 2.6 with height, h, width, w, and infinite length. The infinite length assumption allows the curvature and end-effects of the winding to be ignored. Further, it is assumed that $w >> h$. Due to these assumptions, the magnetic field strength, H, is parallel to the x-axis, and so 1-D analysis is valid.

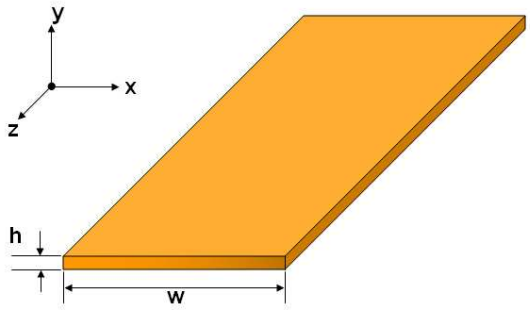

Figure 2.6: An isolated foil strip with infinite length.

In order to derive the diffusion equation describing the magnetic fields in a foil conductor, Maxwell's equations modified for a single frequency is employed:

$$\nabla \cdot E = \frac{\rho}{\epsilon} \tag{2.2}$$

$$\nabla \times E = -j\omega B \tag{2.3}$$

$$\nabla \cdot B = 0 \tag{2.4}$$

$$\nabla \times B = j\omega\epsilon\mu E + \mu J \tag{2.5}$$

where:

$$J = \sigma E \tag{2.6}$$

Substituting Eq. 2.6 into Eq. 2.5 results in:

$$\nabla \times B = (\sigma + j\omega\epsilon)\,\mu E \tag{2.7}$$

Taking a curl of the expression from both sides, and using Eq. 2.3 leads to the following derivation:

$$\nabla \times \nabla \times B = \nabla (\nabla \cdot B) - \nabla^2 B \tag{2.8}$$

$$= -(\sigma + j\omega\epsilon) j\omega\mu B \tag{2.9}$$

Using the expression, $\nabla \cdot B = 0$, and solving for $\nabla^2 B$ leads to,

$$\nabla^2 B = j\omega\mu (\sigma + j\omega\epsilon) B \tag{2.10}$$

The term $-\omega^2\mu\epsilon$ in the derivation, describing the displacement current density, is for all practical purpose negligible inside the conductors themselves such that the diffusion equation of Eq. 2.10 is simplified as:

$$\nabla^2 B = j\omega\sigma\mu B \tag{2.11}$$

Using the identity, $B = \mu H$, the diffusion equation is rewritten as,

$$\nabla^2 H = \alpha^2 H \tag{2.12}$$

where:

$$\alpha = \frac{1+j}{\delta} \tag{2.13}$$

$$\delta = \frac{1}{\sqrt{\pi f \mu \sigma}} \tag{2.14}$$

The solution to Eq. 2.12 has the general form given as:

$$H_x = C_1 e^{\alpha y} + C_2 e^{-\alpha y} \tag{2.15}$$

2.3.1 Skin-Effect

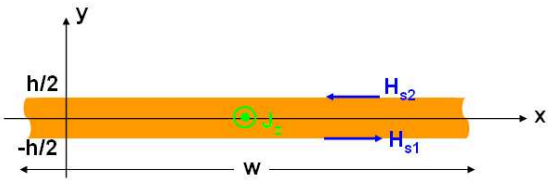

Figure 2.7: The cross-section of an isolated foil conductor.

The cross-section of the foil conductor, shown in Fig. 2.7, carries a net current I. The coefficients C_1 and C_2 in the diffusion equation of Eq. 2.15 are found by

applying the boundary conditions at $y = h/2$ and $y = -h/2$. The H field on the two surfaces are found based on the Ampére's law, $\oint H \cdot dl = I$, given as:

$$H_{s1} = H_{s2} = \frac{I}{2w} \tag{2.16}$$

Applying the boundary conditions to Eq. 2.15 results in a expression for magnetic field strength inside the conductor as given by:

$$H_x = -\frac{I \sinh \alpha y}{2w \sinh \frac{\alpha h}{2}} \tag{2.17}$$

The use of the identity, $-\frac{\partial}{\partial y}(H_x) = J_z$, derived from Maxwell's equation leads to the calculation of the current distribution due to the skin effect inside the foil conductor as:

$$J_z = \frac{\alpha I \cosh \alpha y}{2w \sinh \frac{\alpha y}{2}} \tag{2.18}$$

The loss due to the skin-effect is derived as:

$$\begin{aligned} P_s &= \frac{w}{2\sigma} \int_0^h \left| J_z^2 \right| dy \\ &= \frac{I^2}{4w\sigma\delta} \frac{\sinh v + \sin v}{\cosh v - \cos v} \end{aligned} \tag{2.19}$$

where:

$$v = \frac{h}{\delta} \equiv \text{normalized dimension} \tag{2.20}$$

2.3.2 Proximity-Effect

The foil conductor of Fig. 2.7 is assumed to have '0' net current when modeling proximity-effect. Instead, a uniform magnetic field strength, $H_s cos(\omega t)$, is applied to the surfaces at $y = h/2$ and $y = -h/2$. Applying these two boundary conditions to Eq. 2.15 results in expressions for magnetic field strength and subsequent current distribution inside the foil conductor as:

$$H_x = H_s \frac{\cosh \alpha y}{\cosh \alpha \frac{h}{2}} \tag{2.21}$$

$$J_z = \alpha H_s \frac{\sinh \alpha y}{\cosh \alpha \frac{h}{2}} \tag{2.22}$$

Because the magnetic field strength is applied to the surface of the foil conductor, skin-effect is assumed to be not present. The loss due to proximity-effect is then calculated similarly to skin-effect as given by:

$$\begin{aligned} P_p &= \frac{w}{2\sigma}\int_0^h \left|J_z^2\right| dy \\ &= \frac{wH_s^2}{\sigma\delta}\frac{\sinh\, v + \sin\, v}{\cosh\, v + \cos\, v} \end{aligned} \tag{2.23}$$

2.3.3 Combined Skin- and Proximity-Effect

Due to orthogonality of skin- and proximity-effects, the total loss due to eddy currents is found by summing together losses due to the individual effects:

$$P = \frac{1}{2\sigma}\int_\Omega \left(J_s J_s^* + J_p J_p^*\right) d\Omega \tag{2.24}$$

$$= P_s + P_p \tag{2.25}$$

$$= FI^2 + GH_x^2 \tag{2.26}$$

where:

$$F = R_{dc}\frac{v}{4}\frac{\sinh\, v + \sin\, v}{\cosh\, v - \cos\, v} \tag{2.27}$$

$$G = w^2 R_{dc} v \frac{\sinh\, v - \sin\, v}{\cosh\, v + \cos\, v} \tag{2.28}$$

$$R_{dc} = \frac{1}{\sigma h w} \tag{2.29}$$

This power loss equation can be employed in calculating eddy current losses in the planar windings of transformers.

The overall current distribution in the foil conductor is found by summing the individual current distributions due to skin- and proximity-effect as given by:

$$J_z = \frac{\alpha I}{2w}\frac{\cosh\, \alpha y}{\sinh\, \frac{\alpha h}{2}} + \alpha H_s \frac{\sinh\, \alpha y}{\cosh\, \frac{\alpha h}{2}} \tag{2.30}$$

The average magnetic field strength across the foil thickness is given by:

$$H_s = \frac{H_{s1} - H_{s2}}{2} = \frac{I}{2w} \tag{2.31}$$

Recognizing this fact, the current distribution inside the foil conductor can be expressed in terms of the magnetic field strength on the surfaces of the conductor

as:

$$J_z = \frac{\alpha}{2} H_{s1} \left(\frac{\cosh \alpha y}{\sinh \frac{1}{2}\alpha h} + \frac{\sinh \alpha y}{\cosh \frac{1}{2}\alpha h} \right) + \frac{\alpha}{2} H_{s2} \left(\frac{\sinh \alpha y}{\cosh \frac{1}{2}\alpha h} - \frac{\cosh \alpha y}{\sinh \frac{1}{2}\alpha h} \right) \quad (2.32)$$

The expression allows one to determine the current density inside a conductor based simply on the known surface value of the magnetic field strength. This is a powerful equation that can be utilized in determining the amount of losses occurring in non-magnetic, conductive shields presented in Chapter 5.

2.3.4 FEM Extraction of Winding Losses

FE software may be employed in extracting winding losses due to eddy currents. In order to extract the power loss, Eq. 2.33 is used, which is a general form of Eq. 2.24. The derivation of the losses using the equation depends on an accurate modeling of the field distributions, which is achieved through FEM. The loss is related to an equivalent resistance, R, through Eq. 2.35.

$$P = \frac{1}{2\sigma} \int_{\Omega} J \cdot J^* d\Omega \quad (2.33)$$

$$= I^2 R \quad (2.34)$$

$$R = \frac{1}{2\sigma I^2} \int_{\Omega} J \cdot J^* d\Omega \quad (2.35)$$

As an example, the equivalent resistances of each of the windings of the case study described in Sec. 1.6 are calculated in such a fashion in Table 2.1.

Table 2.1: Derivation of equivalent resistance of the case study.

	Power Loss	Equiv. Resistance
W_1	2.26 W	22.6 mΩ
W_2	1.23 W	1.97 mΩ
W_3	1.55 W	2.48 mΩ

2.4 Core Losses

The losses encountered in the core of an inductor or transformer is due to hysteresis and eddy current losses. This work will examine these losses separately.

2.4.1 Hysteresis Core Loss

In order to understand the cause of hysteresis loss, an understanding of the ferromagnetic material structures is necessary. The fact that electrons orbit the nucleus of atoms is widely known. The orbiting electrons generate magnetic fields, as the flow of electrons is seen as current and currents create magnetic fields. So these orbiting electrons can be viewed as current loops. For non-magnetic materials, the magnetic fields due to individual atoms cancel, resulting in a zero net field. However, for magnetic materials, there are formation of very small pockets or domains in which the average magnetic field is not zero. Typically, these domains are oriented randomly, but under excitation from an external field, these domains tend to align and generate an even larger magnetic flux. The ability of a material to boost the magnetic flux density through the aligned domains is quantified by the term relative permeability, μ_r. Iron's typical relative permeability is around 1000 because for an applied external field excitation of H, iron generates a 1000 times larger magnetic flux density, B, compared to air.

However, energy is expended in orienting and reorienting the domains on each AC cycle. The energy used in these alignments is known as the hysteresis loss. The hysteresis loss density for a sinusoidal excitation without a DC offset is computed with Steinmetz equation as given by Eq. 2.36 [47].

$$\begin{aligned} P_h &= K_1 f^{K_2} \hat{B}^{K_3} \left(C_2^2 T - C_1 T + C_0\right) \qquad (2.36) \\ \text{where:} & \\ P_h &\equiv \text{hysteresis power loss density } \left[W/m^3\right] \\ K_1 = K_2 = K_3 &\equiv \text{loss coefficients} \\ C_2 = C_1 = C_0 &\equiv \text{temperature coefficients} \\ T &\equiv \text{core temperature } (^\circ K/^\circ C) \\ f &\equiv \text{frequency of operation} \\ \hat{B} &\equiv \text{peak flux density}(T) \end{aligned}$$

The loss coefficients, (K_1, K_2, K_3), or equivalent loss density graphs are typically provided by ferrite manufacturers for a single sinusoidal frequency excitation. Typical coefficient values for various ferrites are listed on Table 2.2 [48].

However, for power electronic applications, one almost never encounters a core under a sinusoidal excitation. So, for an extension to arbitrary magnetizing current

Table 2.2: Typical power loss coefficients extracted through curve fitting.

Material grade	Frequency (kHz)	K_1	K_2	K_3	C_2 $\times 10^4$	C_1 $\times 10^2$	C_0
3C80	10 - 100	16.7	1.3	2.5	1.17	2.0	1.83
3C85	20-100	11	1.3	2.5	0.91	1.88	1.97
	100-200	1.5	1.5	2.6	0.91	1.88	1.97
3F3	20-300	0.25	1.6	2.5	0.79	1.05	1.26
	300-500	2×10^{-2}	1.8	2.5	0.77	1.05	1.28
	500-1000	36×10^{-7}	2.4	2.25	0.67	0.81	1.14
3F4	500-1000	12×10^{-2}	1.75	2.9	0.95	1.10	1.15
	1000-3000	11×10^{-9}	2.8	2.4	0.34	0.01	0.67

waveforms, the concept of equivalent frequency based on the weighted average re-magnetization velocity, described in [48], is used to obtain the hysteresis loss:

$$P_h = \frac{1}{\tau} K_1 f_{eq}^{K_2-1} \hat{B}^{K_3} \left(C_2^2 T - C_1 T + C_0\right) \tag{2.37}$$

where:

$\tau \equiv$ switching period $[s]$

$f_{eq} \equiv$ equivalent frequency $[Hz]$

The equivalent frequency, f_{eq}, is defined as:

$$f_{eq} = \frac{2}{\pi^2} \sum_{k=2}^{K} \left(\frac{B_k - B_{k-1}}{B_{max} - B_{min}}\right)^2 \frac{1}{t_k - t_{k-1}} \tag{2.38}$$

where:

$B_{max} \equiv$ maximum flux density in a switching period

$B_{min} \equiv$ minimum flux density in a switching period

$B_k \equiv$ flux density at t_k $[T]$

$t_k \equiv k^{th}$ instant in time $[s]$

$K \equiv$ the number of time instances in a switching period

The coefficients for Eq. 2.37 would then be selected from Table 2.2 according to the equivalent frequency, f_{eq}.

For a DC/DC converter employing pulse width modulation (PWM) scheme, the equivalent frequency reduces to [9]:

$$f_{eq} = \frac{2}{\pi^2} f \frac{1}{D\,(1-D)} \tag{2.39}$$

where:

$$D \equiv \text{duty cycle}$$

In order to find the total core loss due to hysteresis, the power loss density given by Eq. 2.37 is simply multiplied by the core volume.

2.4.2 Eddy Current Core Loss

The core, due to its finite resistivity, also experiences eddy current losses under high frequency excitation. For instance, measured bulk resistivity of 3F3 type ferrite was found to vary from 0.3 to 2.1 Ωm within frequency and temperature range of 10 kHz - 1 MHz and 25°C - 100°C respectively in [47].

Thus, under the assumptions that the flux density is uniformly distributed throughout the cross-sections of the core, and that there is negligible amount of magnetic field generated by the eddy currents, the eddy current core loss density is obtained by [47, 20]:

$$P_e = \frac{\pi}{4\rho} \left(f \hat{B} \right)^2 A_c \tag{2.40}$$

where:

$$P_e \equiv \text{eddy current core loss density } \left[W/m^3\right]$$
$$\rho \equiv \text{effective resistivity of the ferrite } [\Omega m]$$
$$A_c \equiv \text{Cross-sectional area of the core } \left[m^2\right]$$

2.5 Properties of Magnetic Materials

Ferrite manufacturers usually quote a permeability value in data sheets for a particular ferrite based on experimental measurements of very low profile, toroidal structures operating in the linear region. The actual permeability of the ferrite can often deviate significantly from the quoted value due to fabrication tolerances, machining processes, and the geometrical configuration of the final structure. Further deviation is observed due to the frequency of operation, the level of field excitation and the operating temperature.

Most FEM eddy-current solvers, such as Ansoft Maxwell, do not have the ability to model non-linear behavior of the core as the solver computes the result using phasor notations in the frequency domain. Thus a single value of the relative permeability, μ_r, must be chosen to model the core at a certain operating condition. The value of permeability is best measured directly from the actual core, and not from the core material data sheet.

In order to determine the permeability of a core structure, the self-inductance, L_{ii}, across one of the planar windings wrapped around the core is first found experimentally with the rated sinusoidal excitation at a single frequency. The measured self-inductance is then related to the expression of inductance given by:

$$L = \mu_0 \mu_r \frac{N^2 A}{l_{eff}} \tag{2.41}$$

where:

$L \equiv$ measured self-inductance

$\mu_0 \mu_r \equiv$ permeability of the core

$N \equiv$ number of winding turns

$A \equiv$ cross-sectional area of the core

$l_{eff} \equiv$ effective magnetic flux path length

The effective path length, l_{eff}, is a function of core geometry, and so can be approximated analytically. However, for a more precise derivation, FEM is utilized. For an arbitrary excitation by the current, i, the average H-field over the volume of the core is found. The parameter, l_{eff}, is then determined by Eq. 2.42.

$$l_{eff} = \frac{Ni}{H_{av}} \tag{2.42}$$

For example, in order to determine the permeability of the 3F45 ferrite for the transformer in Fig. 2.8, self-inductance of W_1 is determined experimentally at an operating frequency of 750 kHz to be 43.2 μH.

The values of N and A are already known. The effective path length, l_{eff}, is found to be about 0.112 m. Solving for μ_r in Eq. 2.41 then results in relative permeability, μ_r, of 595. This is quite a deviation from the value of 900 indicated in the data sheet!

Figure 2.8: The transformer used for experimental verification of the models.

2.6 Thermal Modeling

The various losses encountered in magnetics generate heat that permeate through the device materials and surroundings, elevating temperature and creating thermal gradients. The elevated temperature change the electrical and magnetic properties of the device. The knowledge of the temperature gradient across a device is essential in order to ensure that a certain temperature limit is not exceeded that may invalidate the electromagnetic models due to a drastic change in material properties. Thus, it is vitally important for the success of a design to create a thermal model in order to ensure the validity of the EM models. A 1-D thermal model of a tube-type planar magnetics is undertaken in this section that determines the maximum temperature present in the structure.

While the thermal model presented is not dependent on frequency directly, the values of winding and core losses can be a function of frequency. However, the major reason that the discussion of the thermal model is placed in this chapter is that the derived expression for the maximum temperature is used in the next section in optimizing the performance of planar magnetics.

Due to the fact that the transformer is thermally insulated on all the sides except at the bottom where the heat sink convectively dissipates most of the heat, the maximum temperature is encountered on the top side. Since the strongest temperature gradient exists from the top to the bottom of the transformer, a 1-D thermal modeling is considered adequate in describing the temperature distribution across the device.

The transformer structure is simplified, as shown in Fig. 2.9, in order to

facilitate 1-D analysis. Following assumptions are made regarding the simplified structure:

1. Windings are infinitesimally thin
2. Interfacial thermal resistances are neglected
3. Winding losses p_{cu} are uniform per unit area
4. Temperature gradient does not exist in the windings ($\Delta T = 0$)
5. Heat transfer coefficient, h, is equivalent to cooling effects of the heat sink
6. Heat flows downward to the ambient
7. Temperature dependence of the materials are neglected

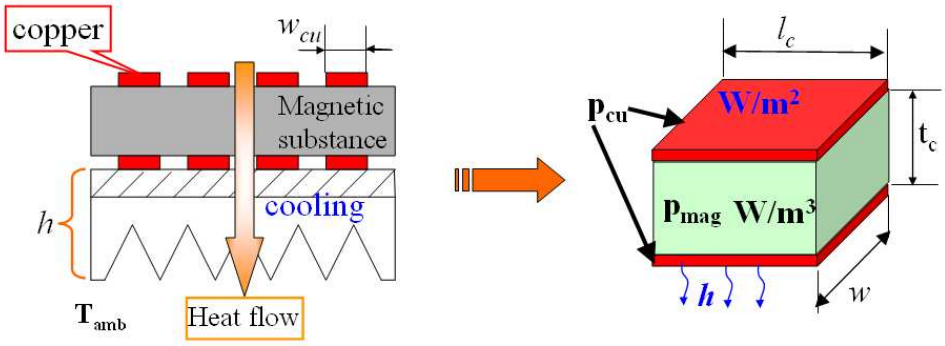

Figure 2.9: Simplification of the transformer structure for thermal modeling.

2.6.1 Formulation of the Governing Equations

All physical events in the known Universe observe the law of conservation of energy, including heat transfer. A differential control volume (CV) of the 1-D structure is extracted in Fig. 2.10. The conservation of energy in the form expressed by Eq. 2.43 is applied to the CV in order to derive the governing equation [49].

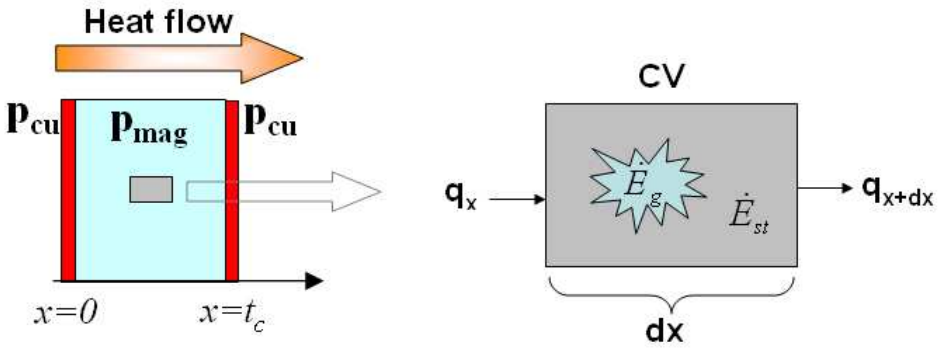

Figure 2.10: Applying conservation of energy to a differential control volume.

$$\dot{E}_{st} = \left(\dot{E}_{in} - \dot{E}_{out}\right) + \dot{E}_g \tag{2.43}$$

where:

$$\dot{E}_{st} \equiv \text{Rate of change of stored energy in a volume}$$
$$\left(\dot{E}_{in} - \dot{E}_{out}\right) \equiv \text{Net rate of energy entering the CV by conduction}$$
$$\dot{E}_g \equiv \text{Rate of energy generated in the control volume}$$

Observing that there is a heat flux in the x direction in the CV,

$$\left(\dot{E}_{in} - \dot{E}_{out}\right) = q_x - q_{x+dx} \tag{2.44}$$
$$= q_x - \left(q_x + \frac{\partial q_x}{\partial x}dx\right) \tag{2.45}$$

Observing Fourier's Law:

$$q_x = -k\frac{\partial T}{\partial x} \tag{2.46}$$

So,

$$\left(\dot{E}_{in} - \dot{E}_{out}\right) = \frac{\partial}{\partial x}\left(k\frac{\partial T}{\partial x}\right)dx \tag{2.47}$$

$$\dot{E}_g = p_{mag}dV = p_{mag}dx \tag{2.48}$$

$$\dot{E}_{st} = \rho C_p \frac{\partial T}{\partial t}dx \tag{2.49}$$

Through various assignments and coursework, it has been observed that the

maximum temperature typically occurs during steady-state [49]. So the transient aspect of the conservation formula, $\dot{E}_{st}$, is set to '0'. Further, the thermal conductivity, k, is assumed to be uniform throughout the material such that it may be pulled outside the partial differentiation. The final form of the governing equation is then given as:

$$\frac{\partial^2 T}{\partial x^2} + \frac{p_{mag}}{k} = 0 \tag{2.50}$$

2.6.2 Boundary Conditions

Boundary conditions are necessary to solve the governing equation described by the differential equation in Eq. 2.50. As this is a one-dimensional, second order differential equation without time information, two boundary conditions are required: one at $x = 0$, and the other at $x = t_c$.

At the boundary $x = 0$, the structure experiences only the heat flux that is generated in the windings through ohmic losses. A convective boundary condition exists at $x = t_c$ where the heat generated in the entire structure is absorbed by the ambient environment at a temperature, T_{amb}, and with a heat transfer coefficient, h. So the boundary conditions at these two locations are described by Eq. 2.51 and Eq. 2.52, respectively.

$$p_{cu}A_s = -kA_s\frac{\partial T}{\partial x}|_{x=0} \tag{2.51}$$

$$\frac{p_{cu}A_s + p_{mag}A_s t_c + p_{cu}A_s}{hA_s} = T_{x=t_c} - T_{amb} \tag{2.52}$$

where:

$$A_s = l_c w$$

2.6.3 Maximum Temperature

The result of applying the two boundary conditions to the governing equation and solving for the maximum temperature at $x = 0$ is the expression:

$$T_{max} = \frac{p_{mag}}{2k}t_c^2 + \frac{p_{cu}}{k}t_c + \frac{2p_{cu} + p_{mag}t_c}{h} + T_{amb} \tag{2.53}$$

The winding loss, p_{cu}, is derived using Eq. 2.54 [11]. However, analytical and numerical modeling provided in Sec. 2.3 may also be utilized in determining the winding loss.

$$
\begin{aligned}
p_{cu} &= \frac{1}{2}\frac{I_{terminal}^2 R_w}{l_c w} \\
&= k_{cu}\frac{J_{max}^2 t_{cu}}{2\sigma}
\end{aligned}
\tag{2.54}
$$

where:

$$
\begin{aligned}
k_{cu} &= \frac{N w_{cu}}{l_c} \equiv \text{Winding factor} \\
w_{cu} &\equiv \text{Width of copper winding} \\
l_c &\equiv \text{Total length of the core} \\
t_{cu} &\equiv \text{Thickness of copper winding}
\end{aligned}
$$

The value of p_{mag} can be derived in three different ways. One is based on the derivation of complex permeability as given by Eq. 2.66. The other is by analytical core loss calculation techniques described in Sec. 2.4. And still another way is to go directly to the ferrite manufacturer's data sheet and use the provided power loss density plot.

2.6.4 Case Study: Thermal Model

For example, the three-winding planar transformer described in Sec. 1.6 is modeled with the secondary and tertiary windings shorted and primary winding excitation of 10 A. The core is 250 mils thick, so $t_c = 6.35$ mm. The value of thermal conductivity of the MnZn ferrite core is $k = 4$ W/(m $\cdot$ K) [50]. The copper loss per unit area is calculated to be $p_{cu} = 236$ W/m^2.

The calculation of p_{mag} is achieved through a plot, shown in Fig. 2.11, that is provided in the data sheet of 3F45 ferrite [46]. After simple calculations, it was determined that the flux density in the core during short-circuit condition was varying anywhere from 37 mT to 62 mT. The value of flux density is low because under quasi-ideal conditions, only the magnetizing current is exciting the core. The operating frequency is rounded up so that the curve in Fig. 2.11 for an excitation level of 50 mT at 1 MHz is applicable.

It should be noted that the power loss that is being utilized for the temperature calculation has a significant dependence on the temperature itself. In order to take the dependence into account, an iterative method must be employed. First, a cubic polynomial given by Eq. 2.55 is fitted to the plot once its data has been multiplied by the thickness of the core, t_c. Then the following algorithm is used to converge

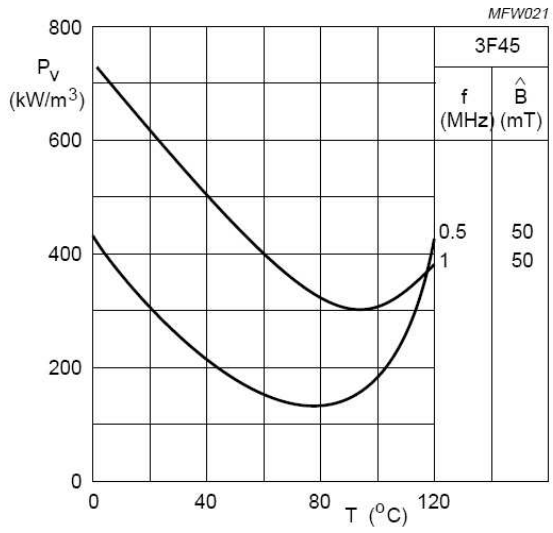

Figure 2.11: Power loss density vs. Temperature.

upon the right power loss value for a given maximum temperature of the core:

1. Assign a value of power loss at 20°C: $p_{mag} = 610 t_c$ (kW/m^2).
2. Calculate T_{max} using Eq. 2.53.
3. Calculate a new power loss value $p_{mag-new}$ based on Eq. 2.55.
4. Until $\left(p_{mag} - p_{mag-new}\right) / p_{mag} \times 100 > 1$
   - $p_{mag} = p_{mag-new}$.
   - Recalculate T_{max} based on this new value of p_{mag}.
   - Find the value of $p_{mag-new}$ using the newly calculated T_{max}
   - Repeat
5. Once the relational specification is met, the converged value of T_{max} is found.

$$p_{mag}\left(T\right) = 3.2179 \times 10^{-3} T^3 - 0.30459 T^2 - 27.6 T + 4557.3 \tag{2.55}$$

So for a parametric sweep of the heat transfer coefficient, h, and the ambient temperature, T_{amb}, Fig. 2.12 shows how the maximum temperature varies at the boundary $x = 0$.

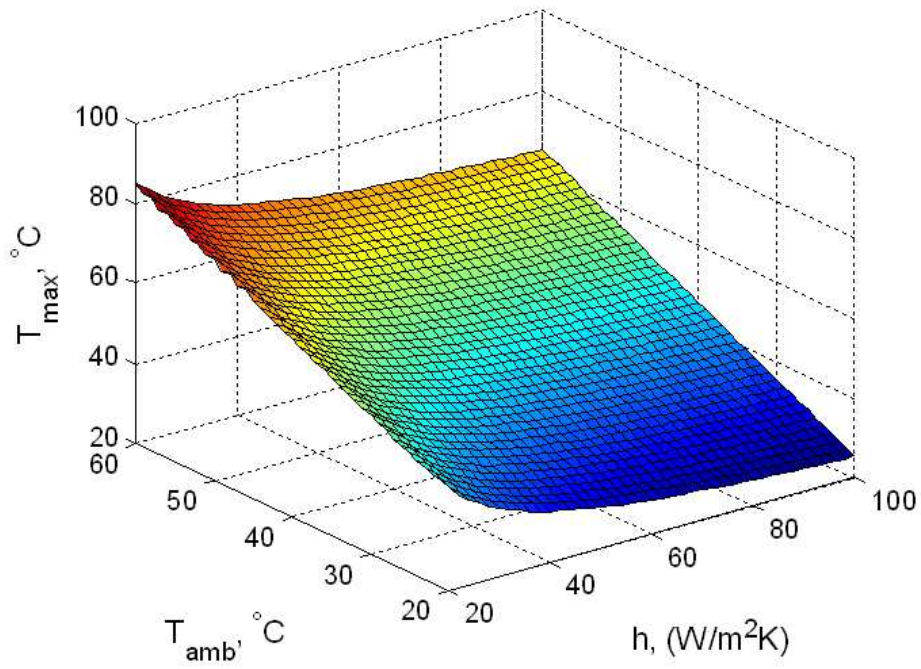

Figure 2.12: Maximum temperature with changes in h and T_{amb}.

2.7 Optimizing the Performance of Planar Magnetics

The various losses in the windings and the core elevate temperature, reduce power density and decrease efficiency. Thus, a methodology introduced in [11] is presented in this section in order to optimize the performance of planar magnetics in terms of maximizing such parameters as power density and efficiency.

Some light is also shed on the misconception that continuous increase in frequency will result in continuous increase in power density, efficiency and reduction in volume. For, there exists a certain optimal frequency for a given geometry and material properties that results in maximum power density and efficiency. Pushing the frequency past this point only results in decreased power density and greater losses.

2.7.1 Complex Permeability

In order to calculate the core losses, the concept of complex permeability is utilized. A magnetic material can be characterized by complex permeability, $\mu_c = \mu_{real} - \mathrm{j}\mu_{imag}$, that represents the energy storage by the real component, and dissipation by the imaginary. For a transformer with open secondaries, the

impedance across the primary winding can be represented with resistance in series with inductance, $Z = R_s + j\omega L_s = j\omega\mu_c L_0$, where L_0 is the self inductance of an air core. For a simple toroidal core with a cross-section, A_c, path length, l_c, and number of windings, N, the series inductance and resistance are expressed by,

$$L_s = \mu_{real} L_0 = \mu_{real} \frac{N^2 A_c}{l_c} \tag{2.56}$$

$$R_s = \omega \mu_{imag} L_0 = \omega L_s \frac{\mu_{imag}}{\mu_{real}}. \tag{2.57}$$

The complex permeability can be extracted directly from the manufacturer's data sheets. The permeability can also be derived experimentally through a relaxation formula described in [51]. For example, the complex permeability of type 3F45 ferrite given in the data sheet is shown in Fig. 2.4. The real and imaginary part of the complex permeability are approximated by,

$$\mu_{real} = \frac{\mu_0 \mu_{c0}}{1 + (f/f_r)^4} \tag{2.58}$$

$$\mu_{imag} = \mu_0 \mu_{c0} \frac{(f/f_r)^2}{1 + (f/f_r)^4} \tag{2.59}$$

where:

$$\mu_{c0} \equiv \text{low frequency permeability}$$

$$f_r \equiv \text{cut-off frequency}$$

$$\mu_0 = 4\pi \times 10^{-7}$$

If there is an air gap in the core, effective complex permeability is calculated as,

$$\mu_{e\_real} = \frac{\mu_{real}\left(1 + k\mu_{real}\right) + k\mu_{imag}^2}{\left(1 + k\mu_{real}\right)^2 + \left(k\mu_{imag}\right)^2} \tag{2.60}$$

$$\mu_{e\_imag} = \frac{\mu_{imag}\left(1 + k\mu_{real}\right) - k\mu_{real}\mu_{imag}}{\left(1 + k\mu_{real}\right)^2 + \left(k\mu_{imag}\right)^2} \tag{2.61}$$

$$\tag{2.62}$$

where:

$$\begin{aligned} k_{ag} &= \frac{k_f k_g}{\mu_0} \\ k_g &\equiv \text{Ratio of length of air gap over length of core} \\ k_f &\equiv \text{Fringing factor} \end{aligned} \tag{2.63}$$

If the core does not have any air gap present such that $k_{ag} = 0$, then Eq. 2.60 and Eq. 2.61 simply reduces to μ_{real} and μ_{imag} respectively.

2.7.2 Definition of Terms

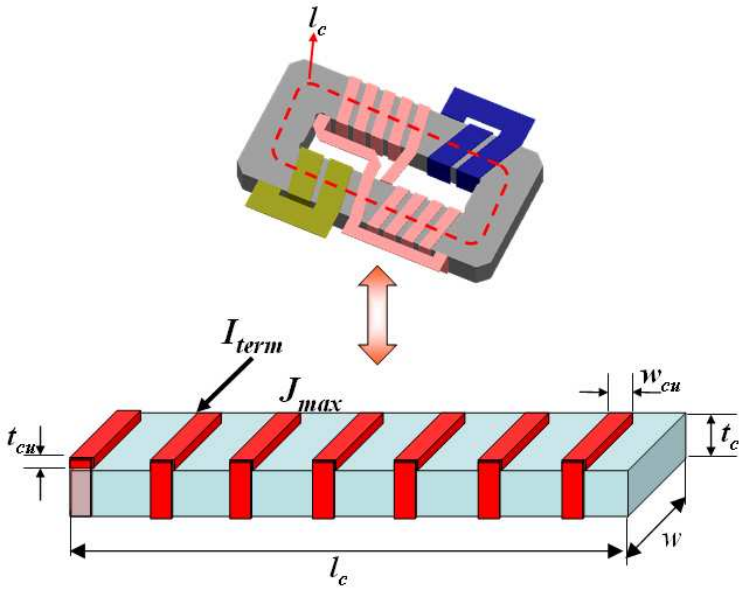

Figure 2.13: Simplification of a core by a solenoidal structure.

Referring to Fig. 2.13, the following terms are defined as such:

$$\begin{aligned} w_{cu} &\equiv \text{Width of the copper traces} \\ t_{cu} &\equiv \text{Thickness of the copper traces} \\ w &\equiv \text{Width of the core leg} \\ l_c &\equiv \text{Total length of the core} \end{aligned} \tag{2.64}$$

$$
\begin{aligned}
t_c &\equiv \text{Thickness of the core} \\
N &\equiv \text{Number of windings} \\
k_{cu} &= \frac{N w_{cu}}{l_c} \equiv \text{Winding factor} \\
\sigma_{cu} &\equiv \text{Conductivity of copper}
\end{aligned} \tag{2.65}
$$

2.7.3 Design Constraint

In any engineering design problems, there exists certain types of constraints that define the limitations and freedom available to the designer. So, the performance optimization of the planar magnetics entails that the problem is adequately defined by the following three design constraints:

1. **Inflexible constraints.** The designer has no control over this type of constraints, as they are usually determined by the design specifications, such as the electrical functions of component terminals, the maximum operating temperature of a device, operating limits, etc.

2. **Discretized parameters.** The designer has some control over the selection of these parameters but only at discrete levels. These constraints include such things as standard thickness of a dielectric or magnetic materials, packaging methods, materials being used, number of winding turns, etc.

3. **Design Variables.** These are the parameters that a designer has the most control over, such as the operating frequency, component dimensions, etc., that can impact the performance of the passive components.

2.7.4 Frequency Scaling Effect on Magnetics

The expression for the volumetric core loss density encountered in the core is given by,

$$
p_{mag} = \frac{1}{2}\mu_{e\_imag}\omega k_{cu}^2 J_{max}^2 t_{cu}^2. \tag{2.66}
$$

Where, the expression for μ_{e_imag} is defined by Eq. 2.61. The copper loss per unit area is,

$$
p_{cu} = k_{cu}\frac{J_{max}^2 t_{cu}}{2\sigma_{cu}} \tag{2.67}
$$

Substituting these two expression for core loss density and copper loss into the expression for maximum temperature given by Eq. 2.53, the maximum current density J_{max} is found:

$$J_{max}^2(f) = \frac{T_{max} - T_{amb}}{\frac{1}{2}\left(\frac{t_c^2}{2k_c} + \frac{t_c}{h}\right)\omega\mu_{e\_imag}(f)\,k_{cu}^2 t_{cu}^2 + \left(\frac{t_c}{k_c} + \frac{2}{h}\right)\frac{k_{cu}t_{cu}}{2\sigma_{cu}}} \tag{2.68}$$

The energy density of a magnetics device with respect to frequency is defined as,

$$E_s(f) = \frac{1}{2}\mu_{e\_real}(f)\,k_{cu}^2 J_{max}^2(f)\,t_{cu}^2 t_c. \tag{2.69}$$

So the subsequent volumetric power density equation is expressed as,

$$P_v(f) = \frac{E_s(f)\,f}{t_c} \tag{2.70}$$

The expression for power loss density is,

$$P_{d\_V}(f) = p_{mag}(f) + \frac{p_{cu}(f)}{t_c} \tag{2.71}$$

So the power conversion efficiency is given by,

$$\eta(f) = \left(1 - \frac{P_{d\_V}(f)}{P_V(f) + P_{d\_V}(f)}\right) \times 100 \tag{2.72}$$

2.7.5 Case Study: Optimizing Performance

The three-winding, planar transformer shown in Fig. 1.9 is optimized based on the design constraints listed in Table 2.3.

Table 2.3: The design constraints of the case study.

Inflexible Constraints	Discretized Parameters	Design Variables
	Standard thickness of core:	Winding factor:
	$t_c = 6.35$ mm	$k_{cu} = 0.35$
Thermal conductivity	Standard thickness of copper:	Frequency: f
of the core:	$t_{cu} = 0.254$ mm	Air gap factor:
$k_c = 4\ \left[\frac{\mathrm{W}}{\mathrm{mK}}\right]$	Complex permeability parameters:	k_{ag}
$T_{max} = 100°\mathrm{C}$	$\mu_{c0} = 900$, $f_r = 6$ MHz	Heat transfer
$T_{amb} = 25°\mathrm{C}$	Number of turns in the windings:	coefficient:
	$N_1 = 10$, $N_2 = 2$, and $N_3 = 2$	h $= 10\ \left[\frac{\mathrm{W}}{\mathrm{m^2K}}\right]$

As an example, the planar transformer used as the case study is optimized primarily in terms of frequency and air gap factor. The effect of core thickness, t_c, on the performance of the planar transformer is also studied. The graph of the power density with respect to frequency is given by Fig. 2.14.

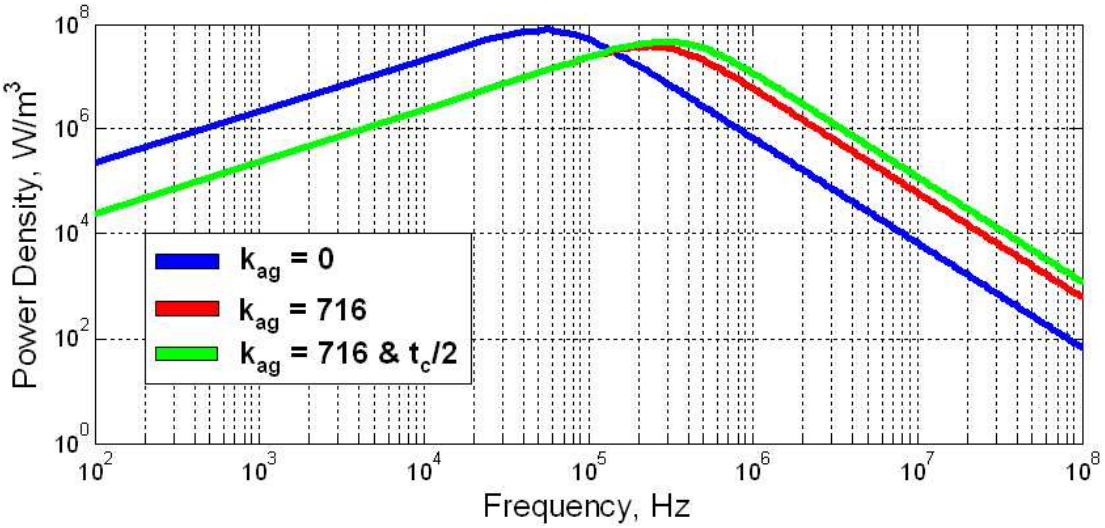

Figure 2.14: The power density vs. frequency of the transformer .

The maximum power density for the case with no air gap, $k_{ag} = 0$, occurs at a frequency of about 55 kHz. When the frequency is pushed past this point, power density drops at a rate of 40 dB per decade. One of the ways to increase power density is by introducing an air gap in the core. The effect of introducing an air gap is depicted in Fig. 2.14 with $k_{ag} = 716$. The frequency at which the maximum power density occurs is now at around 250 kHz. While the absolute maximum power density for $k_{ag} = 716$ is lower than for the case with $k_{ag} = 0$, having an air gap visibly increased the power density past 130 kHz. Further increase in power density beyond 130 kHz is achieved by reducing the profile by half, as seen on the plot of $t_c/2$.

The plot of efficiency with respect to frequency is shown in Fig. 2.15. The losses without any air gap is negligible from 7 kHz to around 100 kHz as the efficiency is maxed out to 100%. The frequency bandwidth resulting in maximum efficiency is further raised by introducing an air gap in the core. However, the losses are quite significant in comparison to the core without an air gap at the lower frequency. The efficiency plots also indicate that there is a certain range of frequency that maximize efficiency, beyond which the efficiency drops drastically. It should be noted that eddy current effects are not taken into account, and that the winding factor, k_{cu}, is quite low (0.35), thus the reason for such a high efficiency.

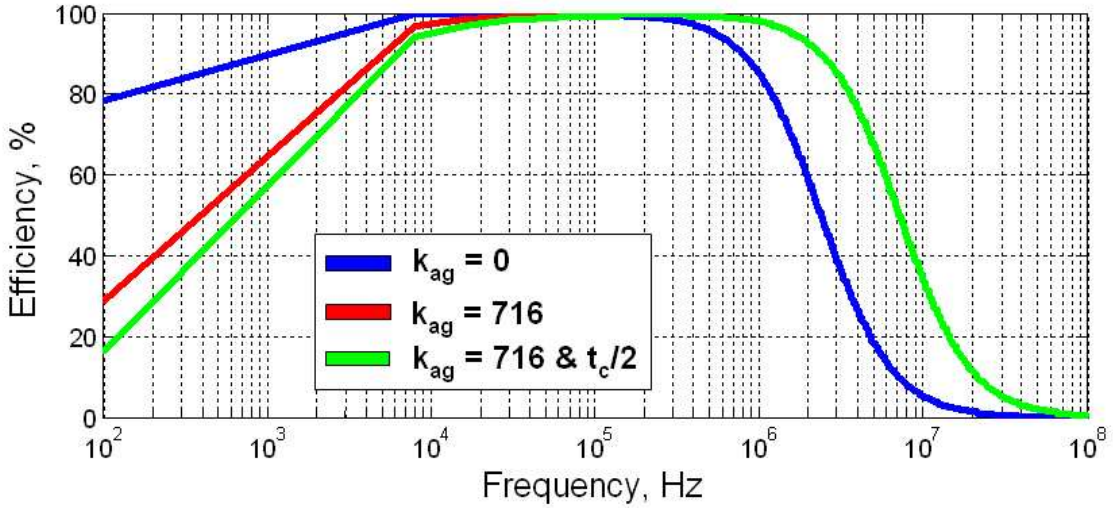

Figure 2.15: The power conversion efficiency vs. frequency of the transformer.

Chapter 3
Modeling of Electrodynamics
3.1 Introduction

Essentially, all known electromagnetic fields behavior are governed by four expressions, collectively known as the Maxwell's equations, given as:

$$\nabla \cdot D = \rho_v \tag{3.1}$$

$$\nabla \times E = -\frac{\partial B}{\partial t} \tag{3.2}$$

$$\nabla \cdot B = 0 \tag{3.3}$$

$$\nabla \times H = J + \frac{\partial D}{\partial t} \tag{3.4}$$

where:

$$D = \epsilon E$$

$$B = \mu H$$

The time-varying behavior of the electromagnetic fields are expressed by Eq. 3.2 and Eq. 3.4. The first of these two equations states that the time varying magnetic flux density induces electric field that is closed around the magnetic field and that the electric field is proportional to time derivative of the flux density. The second equation states that the time varying electric field contributes to the total current density that induces the closed-loop magnetic field strength, H.

The term, $\partial D/\partial t$, is known as displacement current density, J_D. It was added to Eq. 3.4 by James Clark Maxwell in order to successfully explain physical behavior associated with the time-varying electric fields. In fact, the quantity J_D does not correspond to a real current, but rather is a mathematical term used to make sense of the electromagnetic field behavior.

The time-varying electric fields exist between any two winding turns, and between a winding turn and the core, due to eddy current effects, the presence of high frequency magnetic fields and the winding geometry. The time-varying electric fields induce displacement current that in turn contribute to the total induced magnetic fields. The displacement current, I_D, and potential, V, created by the time-varying electric field can be related to each other through a capacitance, C. The relationship

is derived as follows:

$$J_D = \epsilon \frac{\partial E}{\partial t} \tag{3.5}$$

$$J_D = \frac{I_D}{A} \tag{3.6}$$

$$E = \frac{V}{l} \tag{3.7}$$

$$\frac{I_D}{A} = \frac{\epsilon}{l} \frac{\partial V}{\partial t} \tag{3.8}$$

$$I_D = C \frac{\partial V}{\partial t} \tag{3.9}$$

where:

$$C = \frac{\epsilon A}{l} \tag{3.10}$$

Here, the capacitance is defined by the classical expression of a parallel plate capacitor. Thus, transformer models are ideally represented by distributed capacitances along the winding in order to model the high-frequency behavior associated with the time-varying electric fields.

Both numerical and analytical means are explored in this chapter in order to extract the capacitance that exists between two winding turns and between a winding turn and the core.

3.2 Winding Capacitances

At high frequency, capacitances build up in a distributed fashion along the windings, similar to the transmission lines. In order to simplify the order of complexity such that electrostatic approach may be utilized in modeling the high-frequency effects, the winding turns are represented as individual, electrically-isolated loops as portrayed in Fig. 3.1.

Three assumptions are made regarding the potential gradient in the simplified structure of Fig. 3.1.

1. Potential exists between each ring
2. A ring is entirely at a single potential
3. Potential exists between the rings and the core

The rings are electrically insulated from the core in Fig. 3.1 in order to model

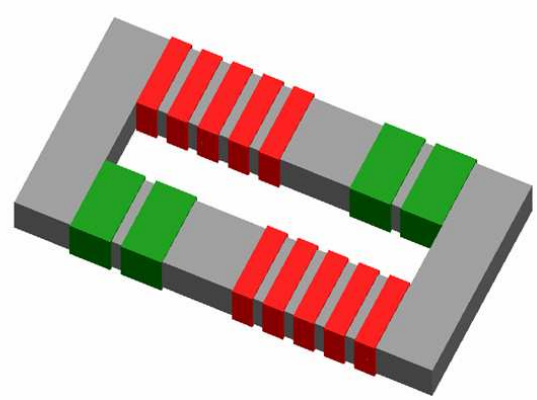

Figure 3.1: Structure is simplified in order to extract winding capacitance.

the capacitance between them. Interwinding capacitance may be represented with the three capacitors shown in Fig. 3.2:

1. $C_{waw} \equiv$ Capacitance between two winding rings through the air.
2. $C_{wiw} \equiv$ Capacitance between two winding rings through the insulation.
3. $C_{wc} \equiv$ Capacitance between the winding and the core through the insulation.

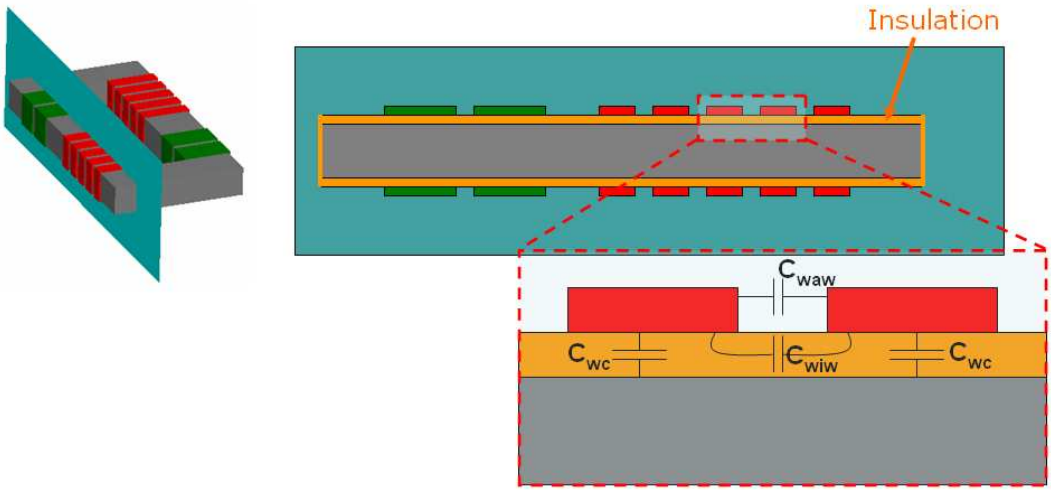

Figure 3.2: Representation of capacitance between two winding rings.

The capacitances C_{waw} and C_{wiw} exist at the same potential gradient so that their summation, $C_{ww} = C_{waw} + C_{wiw}$, is derived together. A second derivation is

required in order to extract the capacitance that exists between the core and the ring, C_{wc}. Once these capacitances are extracted, they may be used in a distributed, transmission line-like equivalent circuit to represent the capacitive impedance across a winding.

The capacitance C_{ww} and C_{wc} are extracted using both numerical and analytical approach. The core is assigned the property of copper in order to model it for the worst-case scenario of having high relative conductivity.

3.3 Capacitance Between Two Winding Rings

3.3.1 Analytical Method

The capacitance C_{ww} between the two windings is derived through Schwarz-Christoffel conformal mapping method coupled with approximations regarding the nature of the field distribution. The approximations are required in order to reduce the order of complexity.

Schwarz-Christoffel is a type of conformal mapping that is used in this work to coordinate transform or map the domain where the fields are elliptical to a domain where they are linear [52]. An example of such a transformation is depicted in Fig. 3.3. In the figure, two piece of material with a potential difference generate electric field, E, and potential gradient, V that are $\perp$ to each other and elliptical in nature. The domain is coordinate transformed through a mapping function f to a new domain where E and V fields distribution are described by straight lines. Because energy is conserved during coordinate transformation, parallel plate method is applied in the new domain to derive the total energy stored in the fields and the subsequent value of capacitance.

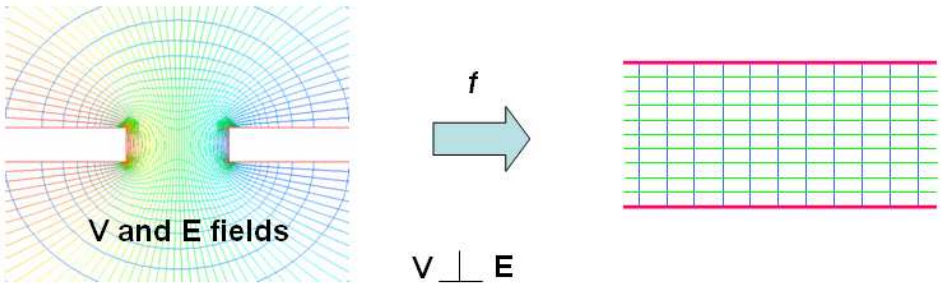

Figure 3.3: Example of coordinate transformation through Schwarz-Christoffel mapping.

The first notable application of Schwarz-Christoffel mapping in extracting the inter-winding capacitance is seen in [53]. Similar work is found in a more recent paper [54]. In both papers, capacitance is found between two adjacent thin-film conductors on a substrate with a very high relative permittivity. The high relative permittivity allows greater energy storage in the substrate due to much higher concentration of electric flux density, D, where $D = \epsilon E$. Thus it can be assumed that the capacitance C_{waw} through the air is negligible in comparison to C_{wiw} through the substrate. Fig. 3.4 depicts the coordinate transformation from $z - plane$ to $\zeta - plane$ in the two papers that are made possible by Eq. 3.11-3.16.

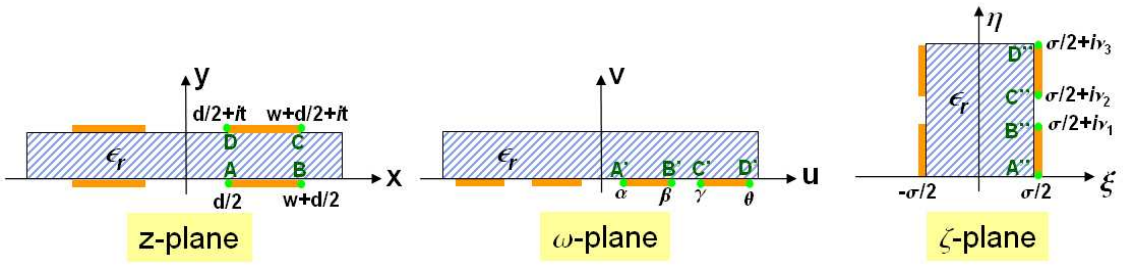

Figure 3.4: Schwarz-Christoffel mapping to extract capacitance between adjacent windings.

z-plane to ω-plane transform:

$$\alpha = \frac{\pi}{2t} tanh\left(\frac{\pi d}{4t}\right) \tag{3.11}$$

$$\beta = \frac{\pi}{2t} tanh\left(\frac{\pi\left(w + d/2\right)}{2t}\right) \tag{3.12}$$

$$\gamma = \frac{\pi}{2t} \frac{1}{tanh\left(\frac{\pi(w+d/2)}{2t}\right)} \tag{3.13}$$

$$\theta = \frac{\pi}{2t} \frac{1}{tanh\left(\frac{\pi d}{4t}\right)} \tag{3.14}$$

ω-plane to ζ-plane transform:

$$\nu_1 = \nu_3 - \nu_2 = \frac{1}{\theta} F\left(sin^{-1}\sqrt{\frac{\theta^2-\gamma^2}{\theta^2-\alpha^2}}, k_2'\right) \tag{3.15}$$

$$\sigma = \frac{2}{\theta} K\left(k_2\right) \tag{3.16}$$

where:

$$k_2 = \frac{\alpha}{\theta}$$

$$k_2' = \sqrt{1-k_2^2}$$

$$F(\phi, k) \equiv \text{Incomplete elliptic integral of } 1^{st} \text{ kind}$$

$$K(k) \equiv \text{Complete elliptic integral of } 1^{st} \text{ kind}$$

Capacitance, C_{ww}, is calculated in the ζ-plane using parallel plate method as given by Eq. 3.17.

$$C_{ww} = \epsilon_0 \epsilon_r \frac{\nu_1}{\sigma} \text{ (F/m)} \tag{3.17}$$

The approximations made in [53, 54] are not applicable in this work due to the differences in the planar transformer's 2-D structure shown in Fig. 3.2. The transformer structure differs from the structure of Fig. 3.4 in that:

1. The relative permittivity of insulation is comparable to air
2. A core is sandwiched between the layers of insulation
3. The insulating material is very thin

These differences lead to a new set of approximations, with reference to Fig. 3.5:

1. At high frequency, due to eddy-current effects and relatively high conductivity, the core is modeled as a conductive plane. The relative high conductivity assumption implies that there will be insignificant potential gradient inside the core, and thus negligible energy storage due to electric fields.
2. Most of the energy between the two windings will be stored in the air, labeled as region I, as the insulating material is very thin and has a relative permittivity comparable to the air itself. In other words, C_{wiw} in Fig. 3.2 is assumed to make a negligible impact on the total winding to winding capacitance, C_{ww}.

3. Since most of the energy is stored in air, region I replaces the high dielectric substrate in the z-plane of of Fig. 3.4. Subsequently, Eq. 3.11 is solved with $t \rightarrow \infty$ because region I extends to infinity.

With these new set of approximation and changes, Schwarz-Christoffel mapping method based on Fig. 3.4 and Eq. 3.11-3.16 is used to extract the winding to winding capacitance, C_{ww}, as:

$$C_{ww} = k\epsilon_0\epsilon_r\frac{\nu_1}{\sigma}\ (\mathrm{F/m}) \tag{3.18}$$

where:

$k \equiv$ multiplier to take into account the energy in region II

If the separation distance, d, in Fig. 3.5 is at least twice as large as the height, h, of the winding, the multiplier, k, is a constant factor because the energy in region II is proportional to the energy in region I. However, if $d < 2h$, then k is not a constant but function of some parameter due to large amount of field distortions taking place in region II.

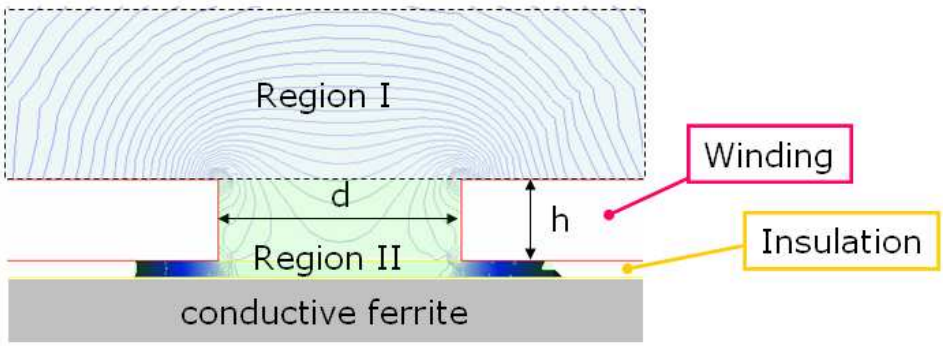

Figure 3.5: Electric field distribution between two winding rings of the planar transformer.

3.3.2 FEM

The 2D FEM model used to extract the capacitance between two winding rings is shown in Fig. 3.6. The left and right windings are assigned a voltage of 1V and 0V respectively. The actual width of the winding ring does not make a large impact on the capacitance as long as it is assumed to be much much larger than the

height, h, of the winding. So there are only three parameters in Fig. 3.6 that have a critical impact on the capacitance, C_{ww}:

1. Winding spacing, d
2. Winding height, h
3. Insulation thickness, t

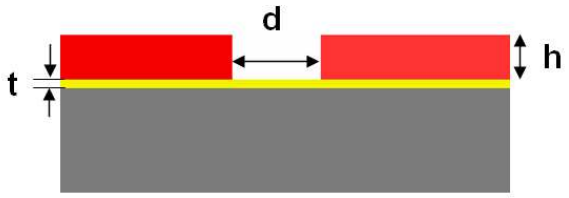

Figure 3.6: Maxwell 2D model to extract capacitance between two winding rings.

Energy stored in a medium by the electric fields is calculated using Eq. 3.19. Energy stored in a capacitor is given by Eq. 3.20. Combining these two equations and solving for the capacitance results in Eq. 3.21. This expression is used to calculate the capacitance during the post processing stage.

$$U = \frac{1}{2}\int_{\Omega} D \cdot E d\Omega \tag{3.19}$$

$$= \frac{1}{2}CV^2 \tag{3.20}$$

$$C = \frac{1}{V^2}\int_{\Omega} D \cdot E d\Omega \tag{3.21}$$

where:

$V \equiv$ potential difference between the two winding rings

The capacitance in Eq. 3.21 is a per meter quantity as the derivation was made using a 2D model. The value is multiplied by mean turn length (MTL) of a winding ring in order to acquire total capacitance between the two rings.

The three critical parameters can be swept in order to derive a three dimensional look-up table for a range of values. However, one would require an order of $O(N^3)$ number of simulations! By restricting two of the parameters, a single polynomial equation could then be used to describe the change in capacitance with the change in a parameter.

As an example, for the structure described in Sec. 1.6, the thickness of the insulating material, t, is set to $t = 2$ mils, as the standard Kapton tape thickness ranges anywhere from 2 to 5 mils. The thickness or height of the copper conductor, h, is set to 10 mils. The winding spacing, d, is then swept from 5 to 60 mils. Fig. 3.7 depicts the capacitance per meter of the 2D model in terms of spacing, d. A sixth order polynomial in Eq. 3.22 is used to fit the discrete data acquired from FEM such that capacitance can be interpolated for the values of winding spacing that were not simulated.

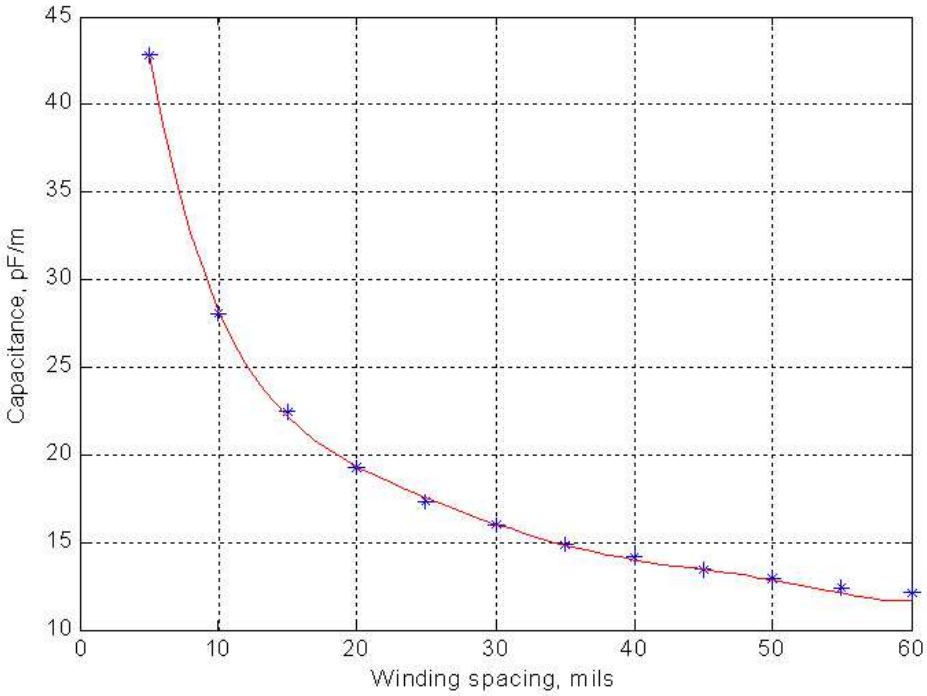

Figure 3.7: Parameter sweep of winding spacing to acquire capacitance.

$$y = 2.634 \times 10^{-8}x^6 - 5.905 \times 10^{-6}x^5 + 5.337 \times 10^{-4}x^4 - 2.494 \times 10^{-2}x^3 + 6.427 \times 10^{-1}x^2 - 9.062x + 74.81 \text{ (pF/m)} \tag{3.22}$$

3.3.3 Case Study: Interwinding Capacitance

As an example, the case study described in Sec. 1.6 is used to compare the results of Schwarz-Christoffel mapping result with FEM in Table 3.1 for $k = 2.02$.

The error apparent in conformal mapping is plotted in Fig. 3.8. The capacitance C_{ww} is acquired by multiplying the values in Table 3.1 by the mean turn length (MTL).

Table 3.1: Comparison of result between Schwarz-Christoffel mapping and FEM.

Conductor Spacing (d)	Conformal Mapping	FEM
5 mils	25.1 pF/m	42.8 pF/m
10 mils	21.3 pF/m	28.1 pF/m
15 mils	19.1 pF/m	22.4 pF/m
20 mils	17.6 pF/m	19.3 pF/m
25 mils	16.4 pF/m	17.4 pF/m
30 mils	15.5 pF/m	16.0 pF/m
35 mils	14.8 pF/m	14.9 pF/m
40 mils	14.1 pF/m	14.1 pF/m
45 mils	13.5 pF/m	13.5 pF/m
50 mils	13.1 pF/m	12.9 pF/m
55 mils	12.6 pF/m	12.5 pF/m
60 mils	12.2 pF/m	12.1 pF/m

It is clear from the results that as long as $d > 2h$, where $h = 10$ mils for the transformer under study, the result acquired through Schwarz-Christoffel mapping with constant k multiplier is quite accurate. So for the structure under study with winding spacing of 30 mils, and MTL of 1.3 inches, the capacitance between two winding turns, C_{ww}, is found to be 0.53 pF.

3.4 Extraction of Winding to Core Capacitance

3.4.1 Analytical Method

The capacitance, C_{wc}, is derived through parallel plate capacitor method using Eq. 3.23 for a typical structure shown in Fig. 3.9. A core with a single winding ring is simulated in the Electrostatic solver in order to affirm the validity of the parallel plate approach. A sheath of insulating material is used between the core and the ring with a relative permittivity of about 3.5. The resulting energy density on the surface of the insulating material is plotted in Fig. 3.10 that shows that a high concentration of energy is localized right below the winding ring. The simulation result asserts that the utilization of parallel plate method is quite valid.

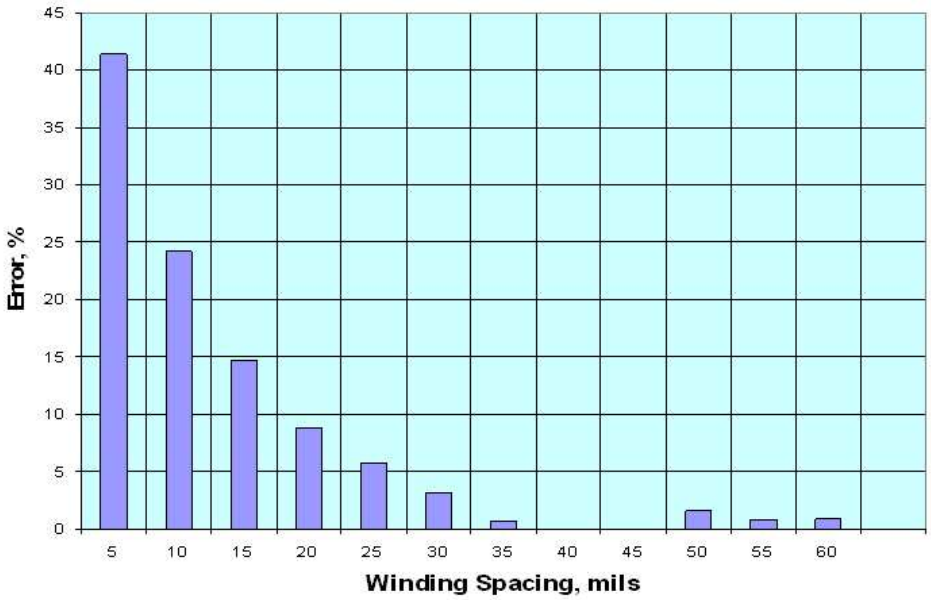

Figure 3.8: Error in the result of Schwarz-Christoffel mapping in comparison to FEM.

$$
\begin{aligned}
C_{wc} &= C^*_{wc} \cdot MTL \text{ (F)} \qquad (3.23)\\
C^*_{wc} &= \frac{\epsilon_0 \epsilon_r w}{t} \text{ (F/m)}\\
\text{where:}&\\
MTL &\equiv \text{mean turn length}
\end{aligned}
$$

3.4.2 FEM

In order to extract the capacitance C_{wc} using FE software, the single winding in Fig. 3.9 is assigned 1 V. The core, which is modeled as being highly conductive, is assigned a value of 0 V. Equation 3.21 is used once again to calculate the capacitance per meter. The value is multiplied by MTL in order to derive the total capacitance between the winding ring and the core.

3.4.3 Case Study: Winding to Core Capacitance

In order to quantitatively compare the capacitance, C_{wc}, derived through the analytical and FEM approach, the structure described in Sec. 1.6 is once again

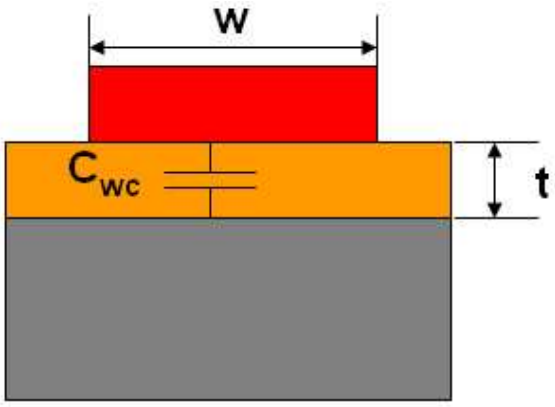

Figure 3.9: Structure used for extraction of capacitance C_{wc} through parallel plate method.

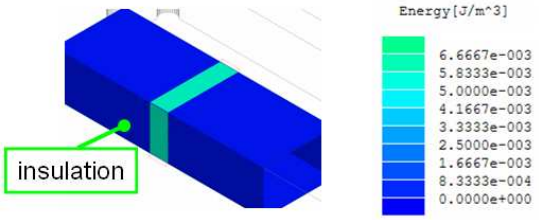

Figure 3.10: Energy density on the surface of insulating material that separates the core from the winding ring.

employed as an example. Table 3.2 compares the analytical derivation of capacitance C_{wc} with the FEM results of both the primary and the secondary winding rings.

Table 3.2: Comparison of resulting capacitance C_{wc} derived through analytical and FEM methods.

	Primary Ring	Secondary Ring
Analytical	51.2 pF	102.4 pF
FEM	52.6 pF	105.2 pF

3.5 Total Capacitance

In order to calculate the total capacitance of a winding to compare against experimental measurements, the cells of capacitance in Fig. 3.2 is linked together similar to Fig. 3.11 for a N-turn winding without regards to resistive and inductive components distributed in the windings. The total equivalent capacitance, C_T, is derived through frequency sweep of the circuit in Fig. 3.11 using circuit simulator such as Simplorer Schematic.

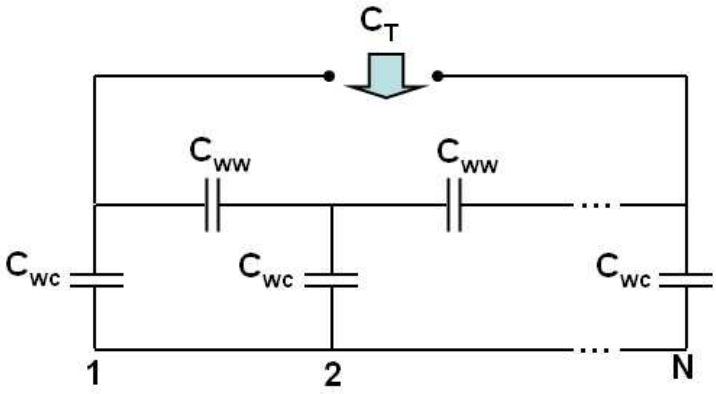

Figure 3.11: Total equivalent capacitance of a winding.

Using the case study described in Sec. 1.6 as an example, the winding to winding capacitance is set to be $C_{ww} = 0.53$ pF. The winding to core capacitance for the primary winding is set to $C_{wc} = 52$ pF. The equivalent capacitance across the primary winding is calculated to be $C_{T1} = 13.2$ pF. Similar calculation is undertaken for both the secondary and the tertiary windings, where the value of winding to winding capacitance is the same as the primary, and value of winding to core capacitance is $C_{wc} = 103.5$ pF. The total capacitance across the three windings is

then:

$$C_{T1} = 13.2 \text{ pF}$$
$$C_{T2} = 52.3 \text{ pF}$$
$$C_{T3} = 52.3 \text{ pF}$$

The equivalent winding capacitance is difficult to measure experimentally because the capacitance is distributed similar to the transmission lines. Rigorous equivalent circuit models of transformer windings are given in [29, 28]. For this work, a simple equivalent circuit shown in Fig. 3.12 is utilized to approximate capacitance based on experimentally extracted impedance trace.

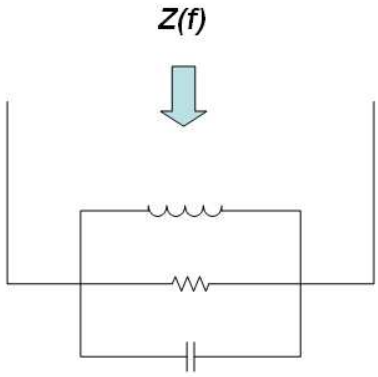

Figure 3.12: Equivalent circuit used to approximate impedance trace across a winding.

The impedance measurement across the primary winding, W_1, is made with Agilent 4294A. The impedance trace and the approximating curve is shown in Fig. 3.13. The equivalent capacitance based on the simple circuit is measured to be about 4.3 pF.

Both FEM and analytical calculation predicted that the equivalent capacitance would be around 13.2 pF. The deviation is due to inaccurate representation of the winding geometry in the models. The transformer used in validating the model is hand wound with copper foils so that there are bound to be inconsistencies in the winding geometry that is not forecasted by the model. Deviations from model include:

1. Winding turns shifting around such that inter-turn spacing are not consistent
2. Windings bulging at the corners that they are folded around.

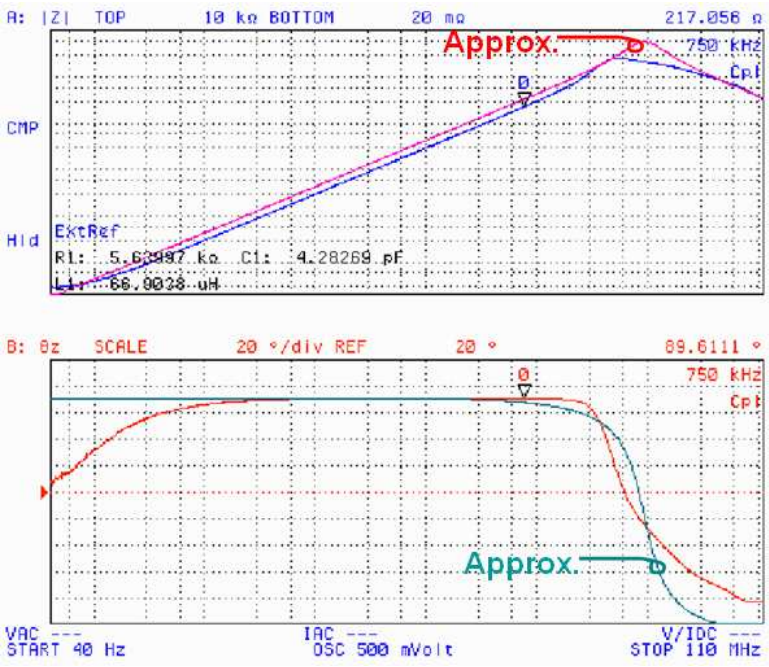

Figure 3.13: Impedance across the primary winding, W_1, with the approximating curve fit.

3. Windings wrapped loosely around the core such that spacing between core and winding is larger than predicted.

In order to take into account some of these deviations, the thickness of the Kapton tape in the model is increased from 2 mils to 4 mils, and the equivalent capacitance is recalculated. The resulting capacitance value is now 6.6 pF. Further increasing the insulation thickness to 6 mils results in capacitance value of 4.5 pF. This is much closer to the experimental measurement of 4.3 pF than the ideally calculated value of 13.2 pF.

Further tweaking of the modeling result is not practical as there are too many approximations being made in both the model and experimental measurement, such that an accurate reference is non-existent.

Chapter 4
Leakage Reactance and Cross-Coupling
4.1 Modeling of Leakage Reactance

The leakage reactance or inductance is a phenomenon that occurs in transformers due to non-ideal coupling of the windings. It represents the amount of magnetic flux that while contributing to the total self-inductance of a winding, does not link or couple with turns of other windings. In other words, the magnetic flux that leak out do not contribute to the mutual inductance of a pair of windings. The desirability of the leakage inductance is dependent on the application. Transformers designed for resonant converters, ballasts in gas discharge lamps, arc welding, and etc. introduce leakage inductance as part of the design. However, in other applications, leakage is one of the prime factors in performance degradation due to losses, poor load regulation and cross-regulation of multiple outputs [55]. Accurate modeling of this phenomenon is essential in any case in order to control the amount of leakage for a given application.

The leakage reactance referred to the primary winding is found by calculating the magnetic energy stored in the structure after shorting the rest of the windings. For example, the magnetic flux density inside the core of a three-winding transformer with the secondary and tertiary windings shorted is depicted in Fig. 4.1. The image is a result of a FE simulation. The lighter color represents higher flux density. The flux density underneath winding W_2 and W_3 is negligible in comparison to W_1 because according to Lenz's law, the current induced in the shorted windings by the magnetic flux from W_1 produce a counter-flux that opposes the flux originally produced by W_1.

The magnetic energy stored, for a period length of one second, in a structure is derived based upon magnetic field distribution calculation using Eq. 4.1 where Ω represents the integration region. The magnetic energy is related to the current and inductance through Eq. 4.2. Combining Eq. 4.1 with Eq. 4.2 and solving for inductance, L, results in Eq. 4.3 that can be used to solve for leakage and other inductances. Inductance is always given with respect to a certain winding. This reference point is set by the value of the source current, I, assigned to the referenced winding in Eq. 4.3.

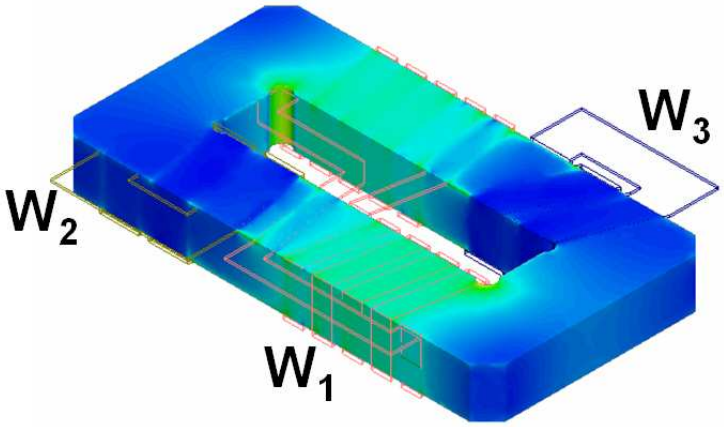

Figure 4.1: Three-winding transformer with secondary and tertiary windings shorted.

$$U = \frac{1}{2}\int_{\Omega} B \cdot H^* d\Omega \tag{4.1}$$

$$= \frac{1}{2} L I^2 \tag{4.2}$$

$$L = \frac{1}{I^2}\int_{\Omega} B \cdot H^* d\Omega \tag{4.3}$$

A methodology in analytically modeling magnetic field distribution due to leakage in a magnetic structure is described in this chapter. Based on the derived field distribution and the energy equation of Eq. 4.3, the leakage reactance is then extracted. Analytical modeling provides an elegant description of the various field effects that are taking place in the transformer in a much quicker fashion than FEM. The primary setback with analytical modeling for complex structures such as the planar three-winding transformer used as the case study in this work is that the modeling is very specific to the type of structures for which it is designed. The structure-specific modeling is due to various approximations that are made in order to reduce the order of complexity of the problem such that simpler analytical equations and methods may be employed in deriving the results. So if the geometry or properties of the structure changes significantly that violate the approximations, the model becomes invalid. However, if the analytical modeling is restricted to a certain type of structure that the model is tailored for, the time required in FEM to reconfigure the model upon every change in certain parameter or the lengthy time required to calculate results for complex 3-D structures is avoided. Analytical

modeling is used in this work to complement FEM, not to replace it entirely. The analytical calculation of leakage reactance is undertaken through the use of method of images.

4.1.1 Method of Images

The concept of method of images relies on uniqueness theorem that states that an entity is uniquely described by certain set of conditions and properties such as the ones present at the boundaries. The method is widely popular in undergraduate electromagnetic textbooks in describing how an image charge can be used to replace the effect of a boundary on an existing charge [56]. The image charge is a valid replacement because it uniquely describes the boundary effects. A problem that was quite complex when a boundary condition had to be satisfied is now much easier with simple charge dipole calculation. The same concept is also applied to moving charges or current where a problem involving magnetic boundary is replaced with a current image to significantly simplify the complexity of the problem without losing accuracy [57, 58].

In this work, method of images is employed to solve for magnetic field distribution inside a core window by replacing the effect of core boundary by simple distribution of images behind the boundary lines. The field at a point inside the core window is found by summing the total effect of all the applied and image fields. A magnetostatic condition is implied in order to reduce the complexity. This is a valid assumption when the window utilization factor is quite low such that eddy current effects on the windings and core is assumed to be negligible.

When a magnetic field generated by a current-carrying conductor comes in contact with a material of infinite permeability, the fields realign at the air-material interface. According to Maxwell's equation, $\nabla \cdot B = 0$, B field closes on itself in a continuous loop through a path of least reluctance, where reluctance is defined as $R = l/\mu A$. When a magnetic material of high or infinite permeability is placed nearby, it provides a path of least reluctance to the magnetic fields such that the fields realign to take advantage. This is demonstrated by the field behavior manifested in Fig. 4.2 when a material of high permeability is placed next to the current-carrying conductor.

An image of the conductor placed behind the air-material interface in Fig. 4.2 would effectively emulate the field distribution observed due to the presence of the magnetic boundary. Such an image replacement for a single boundary is shown for

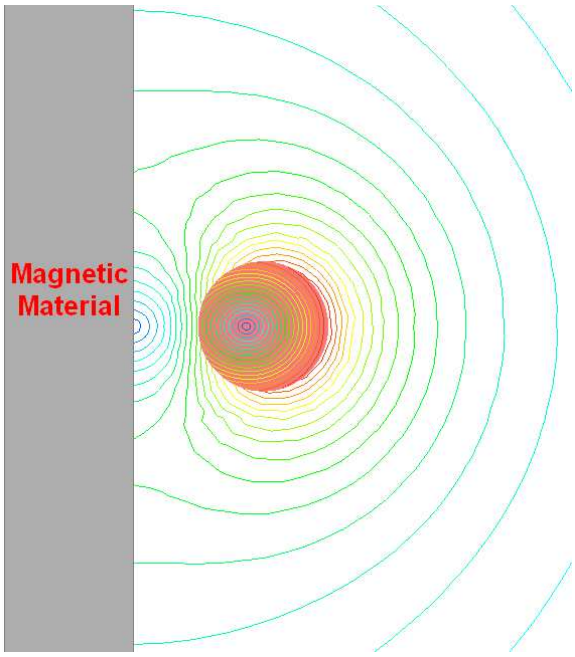

Figure 4.2: Field distribution due to presence of magnetic material.

an arbitrary conductor structure in Fig. 4.3. In the figure, the original window contains two structure carrying current $+I_1$ and $+I_2$ that are some distance away from the magnetic boundary on the left. An image of the two structure is placed the same distance away behind the boundary line carrying the current $+I_1\left(\mu_r - 1\right)/\mu_r$, and $+I_2\left(\mu_r - 1\right)/\mu_r$. The fields are computed in the region of the original window by summing the effect of both the image and the original applied fields. The weight factor, $\left(\mu_r - 1\right)/\mu_r$, accounts for finite permeability of the magnetic material. The field distribution due to the image introduces negligible error in comparison to the magnetic boundary it has replaced.

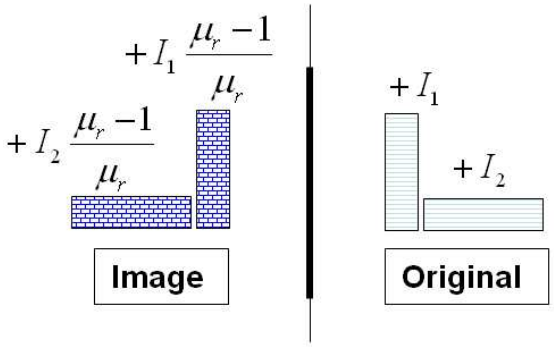

Figure 4.3: Mirror image of a single magnetic material boundary.

Should a magnetic boundary exists on both sides of the conductors of Fig. 4.3, infinite number of images would be required to calculate the field distribution inside the original window. A good analogy of this concept is the number of reflections that are observed in the two mirrors that are placed on each side of a person. Infinite number of reflections are encountered as a mirror reflects the reflection of the other mirror and vice versa, infinitely! When a conductor is surrounded by magnetic material on all four directions like when inside a core window, infinite number of images in all directions are required to represent the field distribution in the region occupied by the core window. This concept is similar to Taylor series expansion of a function $f(x)$ about a point $x = a$ through infinite number of power series terms in order to represent the complex function $f(x)$. And similar to Taylor series, approximations are made by truncating higher order images that make negligible impact on the field distribution inside the core window such that results are acquired with an acceptable amount of accuracy. Such an approximation for a core with an air gap is made in Fig. 4.4 that uses only the images adjacent to the core boundary. Relatively accurate results are found through this method [58, 59]. In order to take the effect of an air gap into account, the current of the image conductors that are on the same side as the air gap is multiplied with a weight factor that contains an effective permeability value, μ_r^*, expressed by Eq. 4.4. If the air gap is not present, then $g = 0$, and the expression simplifies to the relative permeability of the core, μ_r.

$$\mu_r^* = \frac{l}{g + (l - g)/\mu_r} \tag{4.4}$$

where:

$$\begin{aligned} \mu_r^* &\equiv \text{effective permeability due to air gap} \\ l &\equiv \text{length of the yoke} \\ g &\equiv \text{length of the air gap} \end{aligned} \tag{4.5}$$

4.1.2 Field Distribution of a Rectangular Conductor in Air

Magnetic vector potential, A, of a rectangular cross-section of a current carrying conductor in Fig. 4.5 is given by Eq. 4.6 [57]. The equation was incorrectly derived in [57] but corrections have been made in this work. To find the magnetic field components, H_x and H_y, Eq. 4.7 and 4.8 are employed, respectively, resulting in the expression for x and y component of the fields given by Eq. 4.9 and Eq. 4.10.

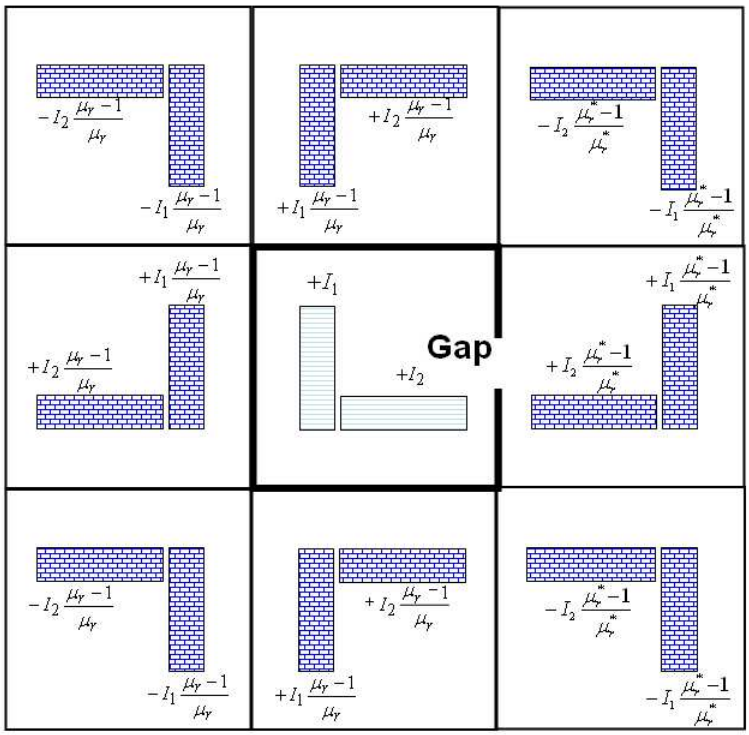

Figure 4.4: Mirror images of a rectangular core.

These magnetic fields were derived incorrectly as well in [57, 58].

$$
\begin{aligned}
A = \frac{I\mu_0}{16\pi ab} \Big\{ & (a-X)(b-Y)\log\left[(a-X)^2+(b-Y)^2\right] \\
& + (a+X)(b-Y)\log\left[(a+X)^2+(b-Y)^2\right] \\
& + (a-X)(b+Y)\log\left[(a-X)^2+(b+Y)^2\right] \\
& + (a+X)(b+Y)\log\left[(a+X)^2+(b+Y)^2\right] \\
& + (a-X)^2\left[\tan^{-1}\left(\frac{b-Y}{a-X}\right)+\tan^{-1}\left(\frac{b+Y}{a-X}\right)\right] \\
& + (a+X)^2\left[\tan^{-1}\left(\frac{b-Y}{a+X}\right)+\tan^{-1}\left(\frac{b+Y}{a+X}\right)\right] \\
& + (b-Y)^2\left[\tan^{-1}\left(\frac{a-X}{b-Y}\right)+\tan^{-1}\left(\frac{a+X}{b-Y}\right)\right] \\
& + (b+Y)^2\left[\tan^{-1}\left(\frac{a-X}{b+Y}\right)+\tan^{-1}\left(\frac{a+X}{b+Y}\right)\right] \\
& - 12ab\Big\}
\end{aligned}
\tag{4.6}
$$

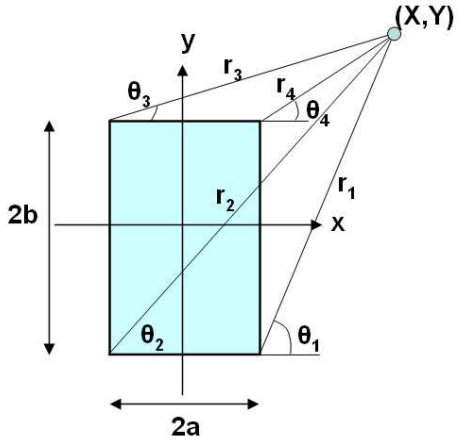

Figure 4.5: Rectangular conductor isolated by air.

$$H_x = \frac{1}{\mu_0}\frac{\partial A}{\partial y} \tag{4.7}$$

$$H_y = -\frac{1}{\mu_0}\frac{\partial A}{\partial x} \tag{4.8}$$

$$\begin{aligned} H_x = \frac{I}{8\pi ab}\Bigg\{ & (b+Y)\left(\tan^{-1}\left(\frac{a+X}{b+Y}\right)+\tan^{-1}\left(\frac{a-X}{b+Y}\right)\right) \\ & -(b-Y)\left(\tan^{-1}\left(\frac{a-X}{b-Y}\right)+\tan^{-1}\left(\frac{a+X}{b-Y}\right)\right) \\ & +(a-X)\log\left(\sqrt{\frac{(a-X)^2+(b+Y)^2}{(a-X)^2+(b-Y)^2}}\right) \\ & +(a+X)\log\left(\sqrt{\frac{(a+X)^2+(b+Y)^2}{(a+X)^2+(b-Y)^2}}\right)\Bigg\} \end{aligned} \tag{4.9}$$

$$
\begin{aligned}
H_y = \frac{I}{8\pi ab}\Bigg\{ & (a-X)\left(\tan^{-1}\left(\frac{b-Y}{a+X}\right)+\tan^{-1}\left(\frac{b+Y}{a-X}\right)\right) \\
& -(a+X)\left(\tan^{-1}\left(\frac{b-Y}{a+X}\right)+\tan^{-1}\left(\frac{b+Y}{a+X}\right)\right) \\
& +(b-Y)\log\left(\sqrt{\frac{(a-X)^2+(b-Y)^2}{(a+X)^2+(b-Y)^2}}\right) \\
& +(b+Y)\log\left(\sqrt{\frac{(a-X)^2+(b+Y)^2}{(a+X)^2+(b+Y)^2}}\right)\Bigg\}
\end{aligned}
\tag{4.10}
$$

4.1.3 Energy in a 2-D Core Window

The 2-D core window is divided into N × M discrete points as shown in Fig. 4.6. The effective field strength at the coordinate (i, j), is found by summing together the field at the coordinate due to all the real conductors and the eight images of each of the real conductors. Mathematically, this is represented as,

$$
H_{eff}(i,j) = \sum_{c=1}^{T}\left(H^{c}_{Real}(i,j)+\sum_{k=1}^{8}H^{c}_{image_{-k}}(i,j)\right) \tag{4.11}
$$

where:

$T \equiv$ Number of winding turns

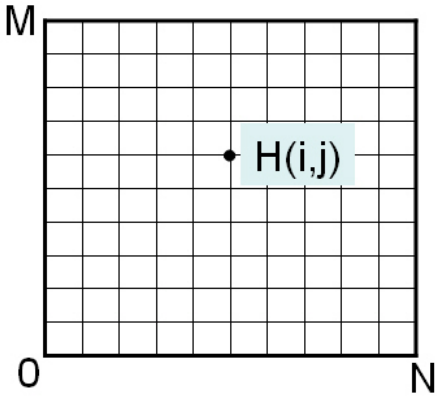

Figure 4.6: The core window divided into N x M discrete points.

The magnetic fields due to the real conductor, H_{Real}, and the image conductor, H_{image}, at the coordinate (i, j) is both found by,

$$H = \sqrt{H_x^2 + H_y^2} \tag{4.12}$$

Where the H_x and H_y are given by Eq. 4.9 and Eq. 4.10 respectively. The magnetic field distribution is then numerically integrated to acquire the total energy stored in the 2D cross-section of the core window using the following expression [59]:

$$U_{xy} = \frac{\mu_0 dS}{2} \sum_{i=1}^{N_x} \left(\sum_{j=1}^{N_y} \frac{H_{i,j}^2 + H_{i-1,j}^2 + H_{i,j-1}^2 + H_{i-1,j-1}^2}{4} \right) \tag{4.13}$$

4.1.4 Analytical Modules

The analytical expressions are written as a simple procedural program in mathematical software such as Matlab in order to derive the field distribution and calculate window energy for arbitrary core and winding specifications. The flowchart of the analytical modules written in Matlab is depicted in Fig. 4.7. All the necessary input parameters are logged into a input file. The file is fed into the field integration module, $\int H$. Depending on how many turns and dimensions of conductor cross-section, the integration module calls upon another module to compute coordinates of each of the original and image conductors. Upon acquiring the coordinates, it calls upon another set of of modules to calculate the field component H_x and H_y due to each of the conductors. These fields are summed together to yield the desired field distributions at well spaced discrete points inside the core window.

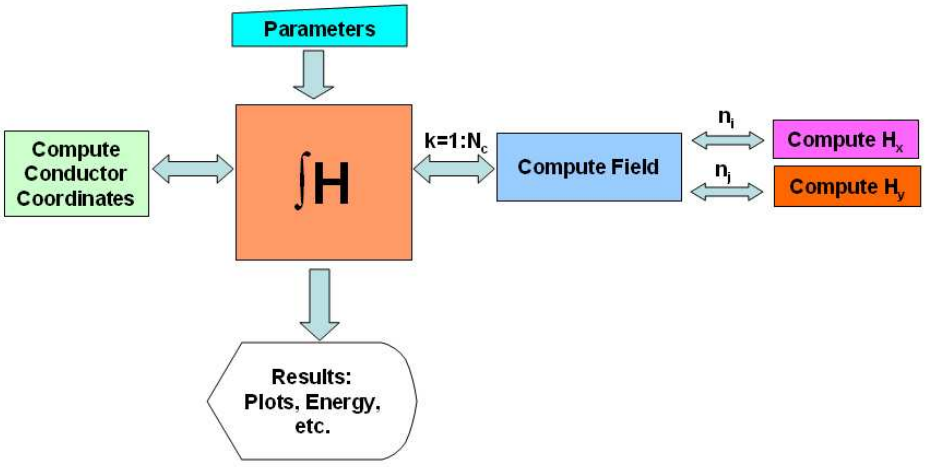

Figure 4.7: Data flow between modules created to calculate energy and field distribution in a core window.

4.1.5 Total Leakage Energy

For a standard core structure, as shown in Fig. 4.8a, the majority of the energy is concentrated inside the core window volume. So once the energy is found in the 2-D core window cross-section using Eq. 4.13, the total energy is found simply by multiplying the 2-D window energy by the thickness of the core.

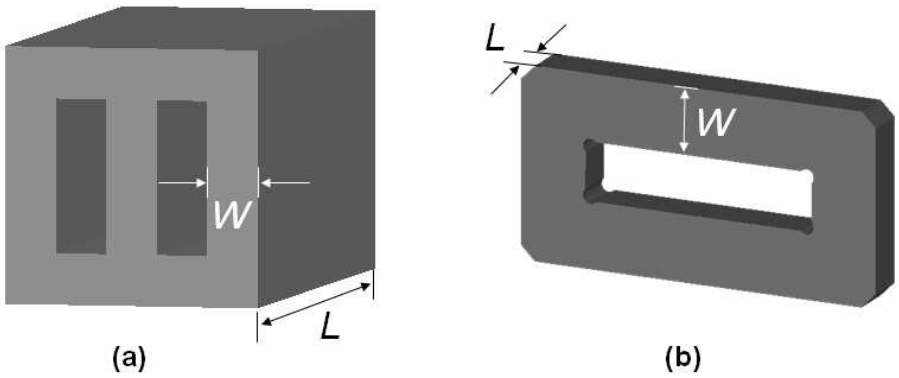

Figure 4.8: Differences in standard vs. planar cores where a) standard core have W < L and b) planar cores have L < W.

However, such an approximation is not valid for the planar cores in which the thickness is relatively smaller than the width of the core legs. In order to see how the energy is distributing around the planar core legs, the energy density is plotted for a planar core with a single winding turn in Fig. 4.9. From the figure, it is observed that the energy is distributed in a cylindrical fashion around the core leg.

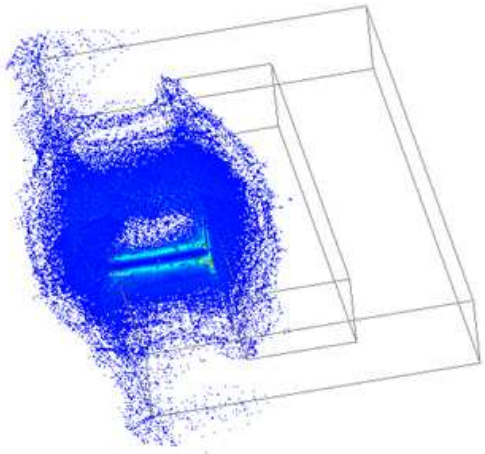

Figure 4.9: Energy distribution in a planar core with a single winding turn.

Thus, to find the total energy associated with the leakage reactance that is stored in the air, the energy stored in the 2D cross-section of the core window is integrated around the core legs using Eq. 4.14, as shown in Fig. 4.10. The factor k in the equation is a property of the structure geometry and is used to take into account the number of core legs, and the level of 3-D distortion of the fields.

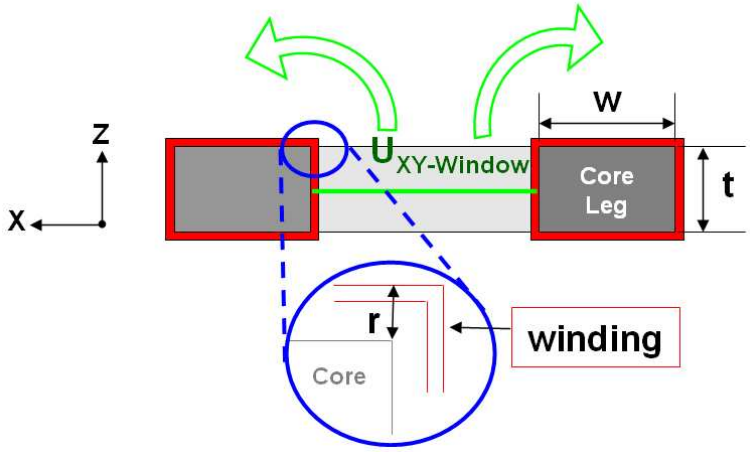

Figure 4.10: Cross-section of the transformer core: calculated energy is integrated around the core legs.

$$U = U_{XY} \cdot (2t + 2w + 2\pi r) \cdot k \tag{4.14}$$

Refer to Appendix B for details on the Matlab codes used in creating the modules.

4.1.6 Case Study: Leakage Extraction

The three-winding planar transformer described in Sec. 1.6 is employed as the case study to demonstrate the methodology used in analytically calculating leakage reactance and comparing the results with FEM.

The field distribution derived through the analytical means is shown next to the one acquired through FEM in Fig. 4.11. In both models, the primary winding is excited with 1 A of current while the secondary and tertiary windings are set to carry -2.5 A of current. A more quantitative comparison of the analytical and FEM method is made in Table 4.1 that compares the total magnetic energy stored in the core window. The FEM energy derivation of the core window is made in both 2D and 3D structure depicted in Fig. 4.12. The energy in the 3D structure is derived on

the $Z = 0$ plane that bisects the core. Further comparison is made by plotting the magnitude of magnetic field strength, H, along the X and Y axis that run through the center of the core window of Fig. 4.11 in Fig. 4.13.

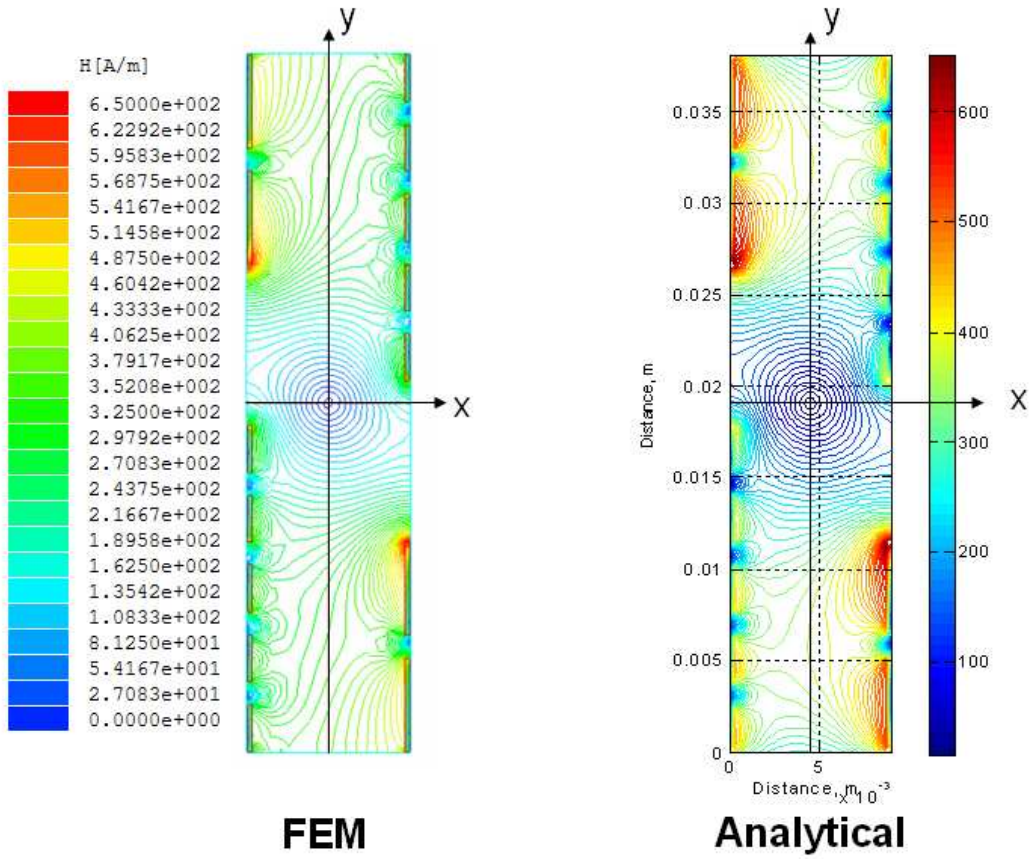

Figure 4.11: Comparison of field distribution result derived through analytical and FEM method.

Table 4.1: Comparison of energy stored in the core window.

	Energy/m	Error in Analytical
Analytical	21.90 μJ/m	-
2D-FEM	19.10 μJ/m	15%
3D-FEM	19.81 μJ/m	11%

The energy calculated of the 2D core-window in Fig. 4.11 is an energy per meter quantity. In order to extract the total leakage energy of the transformer, the derived energy is integrated around the core legs using Eq. 4.14, where $k = 2$. The total leakage energy, U, or the energy associated with leakage inductance is compared against leakage energy derived through FEM for both magnetostatic and

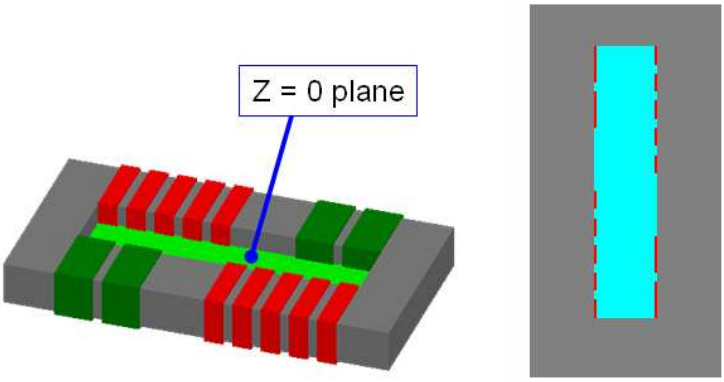

Figure 4.12: The two structures used in FEM to derive the energy in Table 4.1.

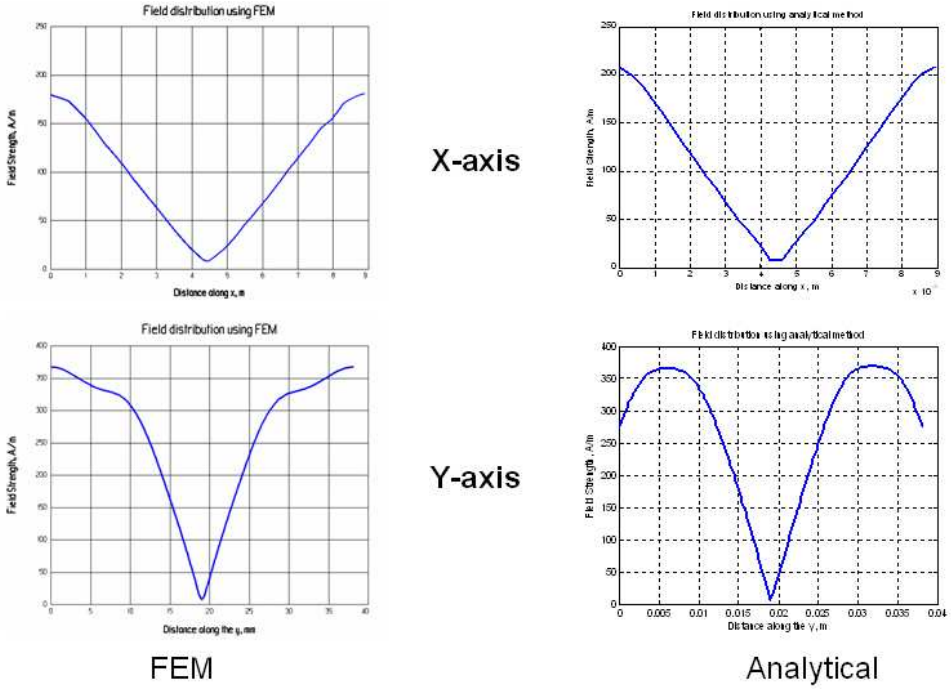

Figure 4.13: The magnetic field strength along the X and Y axes of Fig. 4.11.

high frequency case in Table 4.2 for the three different structures shown in Fig. 4.14. Structure C is the case study. Structure A is the simplified version of structure C but with a different core dimension that is given by Fig. 6.11. Structure B utilizes the same core as structure A and is used to demonstrate deviation of the analytical results due to drastic changes in transformer parameters, such as the number of turns. The comparison makes it obvious that the analytical methodology employed in extracting leakage reactance is valid and acceptably accurate.

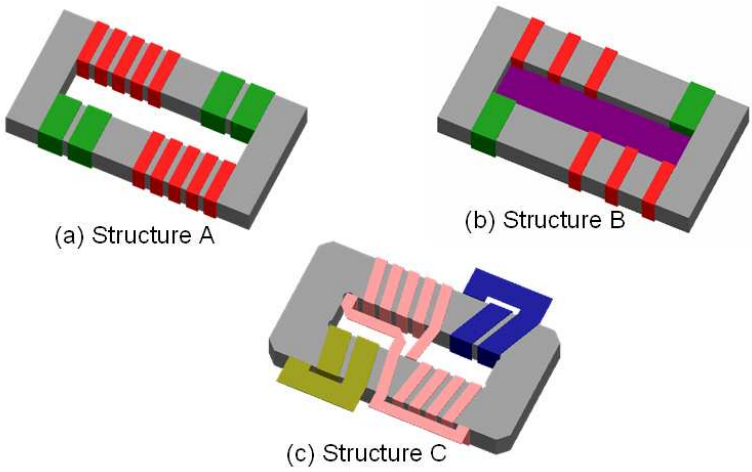

Figure 4.14: Three structures used in comparing effectiveness of the analytical method.

Table 4.2: Comparison of total leakage energy in the structures of Fig. 4.14.

	Analytical	FEM (DC)	FEM (750 kHz)
Structure A	1.37 μJ	1.49 μJ	1.38 μJ
Structure B	0.69 μJ	0.56 μJ	0.63 μJ
Structure C	1.49 μJ	1.53 μJ	1.39 μJ

The leakage inductance is found by utilizing Eq. 4.2. Since the primary winding is excited with 1 A in these simulations, the leakage inductance is found by simply multiplying the energy values of Table 4.2 by 2. The leakage inductance for the three structure acquired through the three different methods are shown in Table 4.3.

Experimental measurement of the leakage in the primary winding of structure C is found to be 2.77 μH, which is comparable with the analytical and FEM results. The other two structures cannot be physically realized due to their winding

Table 4.3: Comparison of leakage inductance in the structures of Fig. 4.14.

	Analytical	FEM (DC)	FEM (750 kHz)
Structure A	2.74 μH	2.98 μH	2.76 μH
Structure B	1.38 μH	1.12 μH	1.26 μH
Structure C	2.98 μH	3.06 μH	2.78 μH

geometry, so the FEM modeling at 750 kHz is assumed to be acceptably accurate in comparing with the analytical results.

4.2 Modeling of Cross-Coupling

In order to model multi-winding transformers accurately in circuit simulators such as Pspice and Saber, the various magnetic cross-coupling of the windings must be taken into account. The classical cantilever model of two-winding is extended to N-winding transformers in [34]. For example, the extended cantilever model of a three-winding transformer is shown in Fig. 4.15. The model can also be easily converted to the N-port model, which is beneficial in determining current ripple expressions and zero-ripple condition [60]. The N-port model is not discussed further in this work.

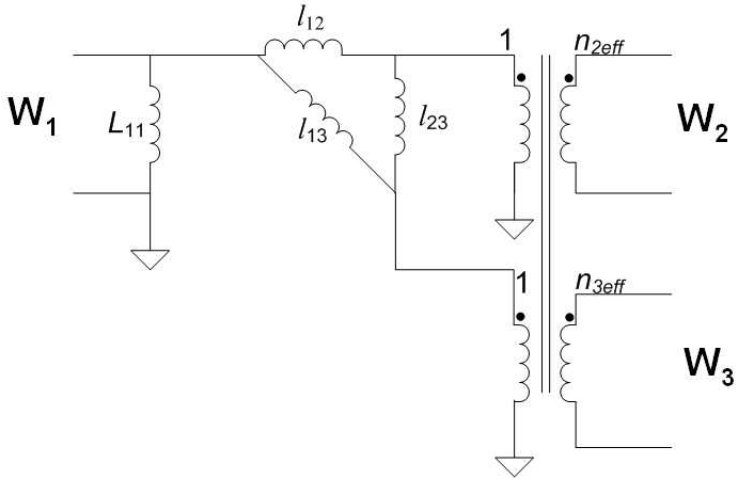

Figure 4.15: Extended Cantilever Model of Three-Winding Transformer.

Extraction of the parameters in Fig. 4.15 is done experimentally in [34]. An alternative is to use a FE software for the parameter extraction before the device is even built; albeit with slightly different approaches as electromagnetic FE software tools often do not support voltage measurements in the eddy current solvers.

There are two ways to extract the extended cantilever model parameters. The first is by making several short-circuit measurements, similar to the experimental method in [34]. The second method is to use self- and mutual-inductance matrix combined with the equations outlined in [34]. Some FE software, such as Ansoft Maxwell, has the ability to generate the inductance matrix automatically in one simulation. For the software titles that do not have this functionality, the first method is recommended.

The problem with the second method is that the inductance matrix is calculated through superposition of results acquired from multiple open-circuit tests [61] that does not take the eddy current effects into account that would exist if two adjacent windings were shorted simultaneously. However, when windings are single layer, not interwoven and are relatively spaced out, the eddy current effects may be negligible so that the inductance matrix can be used with acceptable accuracy.

There are two definitions of effective turn ratio, n_{eff}, where one is a more classical definition that is defined in [44] and the other defined in the extended cantilever paper [34]. The effective turn ratio simply means that the electrical turn ratio is lower than the physical turn ratio due to non-ideal coupling between the windings. The classical definition of effective turn ratio between winding W_2 and W_1 is given by Eq. 4.15 and the one in the paper by Eq. 4.16. The effective turn ratios are calculated with reference to the primary windings for either definitions. From experimental measurements, Eq. 4.16 is found to be the proper definition for the extended cantilever model.

$$n_{j_{eff}} = \sqrt{\frac{L_{jj}}{L_{11}}} \tag{4.15}$$

where:

$$L_{ii} \equiv \text{self inductance}$$

$$n_{j_{eff}} = \frac{M_{1j}}{L_{11}} \tag{4.16}$$

$$n_{j_{eff}} = \frac{v_j}{v_1} \tag{4.17}$$

where:

$$M_{ij} \equiv \text{mutual inductance}$$

4.2.1 Method 1: Multiple-Short Circuit Tests

Since voltage cannot be measured directly, it must be derived through alternative means. The voltage across a winding is equal to the impedance of that winding multiplied by the current through that winding, or $V = IZ$. An impedance across a winding can be approximated with a series combination of an inductor and a resistor as shown in Eq. 4.18. There is no capacitance involved in the equation as energy storage due to electric field is not modeled in typical decoupled quasi-static methods. For short-circuit simulations, the inductance is the leakage inductance referred to the winding under analysis. As the series resistance, primarily due to AC resistance of the windings, is much lower than the reactive impedance of the equivalent inductance, the series resistance can be assumed to make a negligible contribution to the winding voltage. Thus voltage across the windings may be assumed to be entirely caused by the impedance of the equivalent inductance.

$$\begin{aligned} v_i &= (R_i + j\omega L_{li})\, i_i \\ \omega L_{li} &>> R_i \\ &= j\omega L_{li} i_i \end{aligned} \tag{4.18}$$

Equation 4.19 is provided in [34] to calculate the cross-coupling inductance values of Fig. 4.15. Substituting the expression of voltage derived in Eq. 4.18 into Eq. 4.19 results in the Eq. 4.20 that can be used to extract the cross-coupling terms.

$$l_{ij} = \frac{v_i}{j\omega n_{i_{eff}} n_{j_{eff}} i_j} \tag{4.19}$$

$$= \frac{L_{li} i_i}{n_{i_{eff}} n_{j_{eff}} i_j} \tag{4.20}$$

In the equations, subscript i represents the winding that is excited with a current i_i, while the other windings are shorted. The parameter L_{li} is the leakage inductance of the excited winding i under the same shorted condition. The current i_j is the short-circuit current in winding j. The number of turns in the primary winding, $n_{1_{eff}}$, is normalized to 1. The effective turn ratios are then derived as shown in Eq. 4.16 in reference to the primary winding.

The self-inductance of the primary winding in Fig. 4.15 is extracted with the

other windings electrically open. The effective turn ratios are calculated through Eq. 4.16 and inductance matrix. And the cross-coupling terms are acquired through Eq. 4.20 and $(N-1)$ short-circuit tests for a N-winding transformer.

4.2.2 Case Study: Cross-Coupling

The inductance matrix of the three-winding transformer in Fig. 1.9 is given by Table 4.4. The self-inductance, L_{11}, of the primary winding is found to be 43.4 μH. The effective turn ratios are calculated as follows:

$$\begin{aligned} n_{2_{eff}} &= \frac{M_{12}}{L_{11}} \\ &= \frac{8.41}{43.4} \\ &= 0.194 \end{aligned}$$

$$\begin{aligned} n_{3_{eff}} &= \frac{M_{13}}{L_{11}} \\ &= \frac{8.45}{43.4} \\ &= 0.195 \end{aligned}$$

Table 4.4: Inductance matrix generated by Maxwell for the three-winding transformer.

L_{ii}/M_{ij}	W_1	W_2	W_3
W_1	43.4 μH	8.41 μH	8.45 μH
W_2	8.41 μH	1.90 μH	1.60 μH
W_3	8.45 μH	1.60 μH	1.90 μH

Two short-circuit tests are required in order to determine the three cross-coupling terms of Fig. 4.15. However, in order to highlight that the value of cross-coupling inductance depends on which winding is excited, three short-circuit tests are performed instead. In each of the tests, a winding is excited with 1 A of current while the other two windings are shorted. The value of 1 A normalizes the energy calculations so that the current term can be left out from the equations. The flux density for each of the three simulations are depicted in Fig. 4.16. The derivation of cross-coupling inductances are given in Table 4.5.

In an ideal situation, cross-coupling inductances, l_{ij} and l_{ji}, are the one and

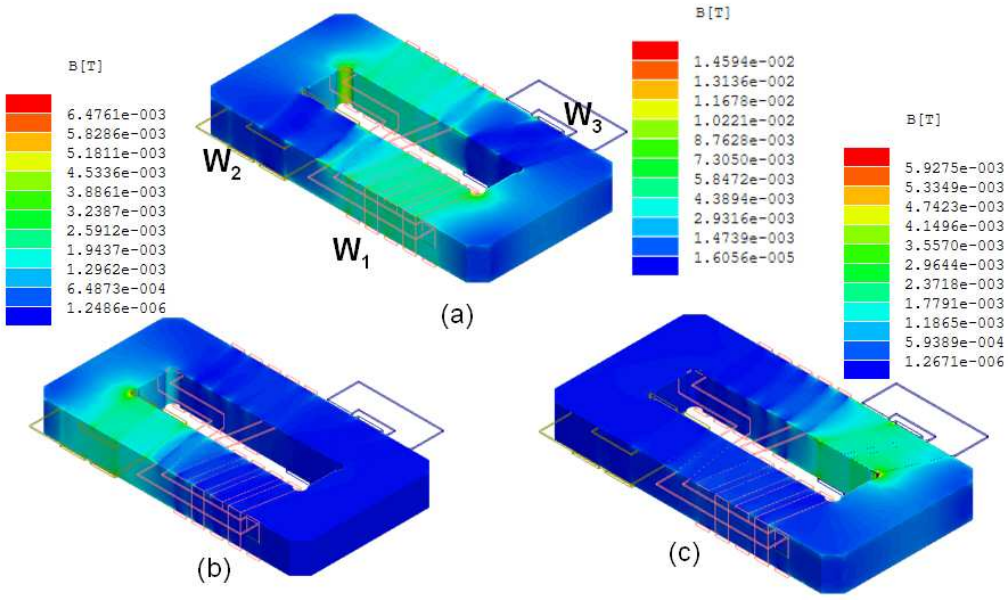

Figure 4.16: Flux Density in the core with a) W_2 and W_3 shorted, b) W_1 and W_3 shorted, and c) W_1 and W_2 shorted.

Table 4.5: Extended cantilever parameter derivation through method 1.

	Test 1	Test 2	Test 3
Winding Excited (1 A)	W_1	W_2	W_3
Shorted Windings	W_2 W_3	W_1 W_3	W_1 W_2
Leakage Inductance	$L_{l1} = 2.75\ \mu$H	$L_{l2} = 0.265\ \mu$H	$L_{l3} = 0.244\ \mu$H
Short-Circuit Currents	$i_2 = 2.32$ A $i_3 = 2.50$ A	$i_1 = 0.223$ A $i_3 = -0.148$ A	$i_1 = 0.222$ A $i_2 = -0.137$ A
Cross-Coupling Inductances	$l_{12} = \frac{2.75\mu}{1 \cdot 0.194 \cdot 2.32} = 6.11\ \mu$H $l_{13} = \frac{2.75\mu}{1 \cdot 0.195 \cdot 2.50} = 5.64\ \mu$H	$l_{21} = 6.10\ \mu$H $l_{23} = -46.9\ \mu$H	$l_{31} = 5.26\ \mu$H $l_{32} = -47.1\ \mu$H

the same. However, as Table 4.5 manifests, such a condition does not exist as the winding geometry of Fig. 1.9 is not entirely symmetrical. Thus, the asymmetrical nature of the geometry causes the magnetic flux coupling to be different between winding i and j when winding i is excited as opposed to winding j. In order to remain on the conservative side, the higher of the two inductance l_{ij} and l_{ji}, is chosen for the model in Fig. 4.15. Table 4.6 summarizes the final chosen value of the extended cantilever model derived through Method 1.

Table 4.6: Summary of parameters of extended cantilever model using method 1.

L_{11}	l_{12}	l_{13}	l_{23}	$n_{2_{eff}}$	$n_{3_{eff}}$
43.4μH	6.11 μH	5.64 μH	-47.1 μH	0.194	0.195

4.2.3 Method 2: Inductance Matrix

A quicker, alternative method in deriving the model of Fig. 4.15 is to use the inductance matrix [34]. Some software, such as Ansoft Maxwell, can automatically generate these matrices, but for the software that cannot, method 1 is the better choice. The derivation of the extended cantilever parameters for an N-winding transformer are as follows:

$$L = \begin{vmatrix} \alpha_{11} & \alpha_{12} & \cdots & \alpha_{1n} \\ \alpha_{21} & \alpha_{22} & \cdots & \alpha_{2n} \\ \vdots & \vdots & \ddots & \vdots \\ \alpha_{n1} & \alpha_{n2} & \cdots & \alpha_{nn} \end{vmatrix} \tag{4.21}$$

$$B = L^{-1}$$

$$\begin{aligned} L_{11} &= \alpha_{11} \\ n_{i_{eff}} &= \frac{\alpha_{1i}}{\alpha_{11}} \\ l_{ij} &= -\frac{1}{n_{i_{eff}} n_{j_{eff}} B\left(i,j\right)} \end{aligned}$$

4.2.4 Discussion of Results

A comparison of the two methods are given in Table 4.7 along with the experimental measurements for the three-winding transformer used as the case study.

Table 4.7: Comparison of extended cantilever model parameters between experimental and FEM results.

Extended Cantilever Parameters	Multiple Short-Circuit Simulation	Inductance Matrix	Experimental Measurements
L_{11}	43.4 μH	43.4 μH	43.19 μH
l_{12}	6.11 μH	6.15 μH	6.67 μH
l_{13}	5.64 μH	5.79 μH	5.81 μH
l_{23}	-47.1 μH	-47.8 μH	-58.2 μH
$n_{2_{eff}}$	0.194	0.194	0.191
$n_{3_{eff}}$	0.195	0.195	0.192

There are differences in the results of the two FEM methods, but the values are close enough such that the simpler Method 2 becomes the optimal choice for the structure under study. The differences are attributed to the approach that FE software like Maxwell takes in calculating the inductance matrix. The inductance matrix is calculated through superposition of open-circuited fields such that eddy-current effects apparent during short-circuits in Method 1 are not taken into account. For structures with much higher window utilization factor, the differences in these two methods may become more stark due to increased eddy-current effects taking place. Thus to insure that accurate parameter values are extracted, the more cumbersome Method 1 must be utilized.

The experimental results are very close to modeling results. The most significant deviation is observed for the cross-coupling inductance between windings 2 and 3, l_{23}. This is due to increased sensitivity of the Eq. 4.19 on the induced short circuit current of the other winding. The primary winding is shorted, entirely impeding any coupling between winding 2 and 3 through the core. The flux from winding 2 has to go through alternate paths to couple with winding 3. Thus, the coupling term, l_{23}, not only depends on the transformer structure but also on materials of devices that are adjacent to the transformer. This behavior is most apparent in comparison of the cantilever parameters due to different shield materials in Table 5.4. So while the results in finite element modeling was acquired with the structure isolated by vacuum, such an isolation does not exist during experimental measurements.

Chapter 5
Shield Design
5.1 Introduction

Issues pertaining to electromagnetic shield design is presented in this section. As electric field shielding is relatively easy to achieve, the focus will be on near-field magnetic shielding. However, the final design of the magnetic shield will also be applicable as an electric shield with minor changes.

Before an electromagnetic analysis is undertaken, it is pertinent to know whether the analysis will be done in the near or the far field region. The methodologies employed in the near field regions is often quite different and more complicated than the far field regions. A helpful rule of thumb in determining whether the analysis is for the near or far field region is portrayed by Fig. 5.1 [22]. Typically, field analysis that is undertaken within a distance of about one-sixth of the wavelength is considered to be in the near field region. At distances greater than this, or the far field region, electromagnetic fields are modeled as a plane-wave where the electric and magnetic fields are perpendicular to each other and to the direction of propogation. The properties of the field in this region are dependent mainly on the medium through which the fields are propogating. At the distances less than one-sixth of the wavelength, or the near field region, the electromagnetic field are much more complex and the properties of the fields are primarily characterized by the source characteristics.

The distance of the boundary separating the near from the far field region, expressed by $\lambda/2\pi$, is given in Table 5.1 for frequency ranging from 10 kHz to 10 MHz. Most power electronic equipment operate inside this range of frequency. Thus, the shield design for an electromagnetic passive structure is confined to the near field region. The boundary distance is calculated based on field propagation through a medium with unity relative permeability, μ_r, and relative permittivity, ϵ_r. However, for non-unity properties, the wavelength of the fields inside a medium with unity properties is simply divided by the refractive index, n, given by $\sqrt{\epsilon_r \mu_r}$ of the medium. Even with the refractive index taken into account, the distances are large enough such that the analysis is still confined to the near field region.

In the far field region, the ratio of electric field, E, and magnetic field, H, is

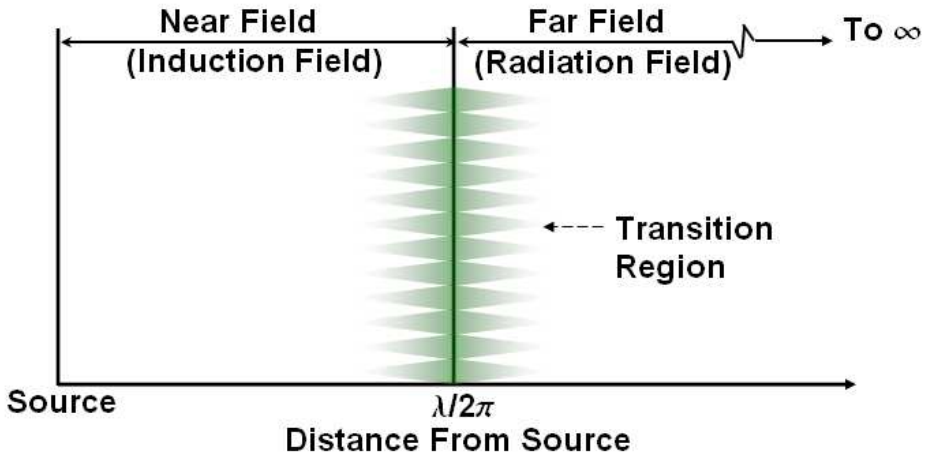

Figure 5.1: Electromagnetic field analysis is dependent on the distance from the source of radiation.

Table 5.1: The distance of the boundary separating the near from the far field region for a range of frequency.

Frequency	Distance to Boundary
10 kHz	4770 m
50 kHz	954 m
100 kHz	477 m
500 kHz	95.4 m
1 MHz	47.7 m
5 MHz	9.54 m
10 MHz	4.77 m

constant and is quantified by the characteristic impedance of the air, $E/H = 377$ Ω. However, in the near field region, this ratio is not constant, so these fields must be considered separately. Far-field shielding is not applicable in this work so will not be considered in this section. However, aspects of the plane-wave concept is still valid and will be utilized as part of the near-field shield design.

Shield design can be undertaken through two different methods [23]:

1. **Magnetoquasistatic (MQS)**. This concept assumes that the object is electrically small, which is a valid assumption for near-field shield design. In terms of magnetic shielding at DC to low frequency, this concept relies on shunting, guiding, or diverting of magnetic fields by introducing a path of least reluctance. Magnetic materials are the typical means in achieving this objective. Shielding at higher frequency is based on the eddy current effects through utilization of conductive shield materials. The induced currents in the shield generate counter fields that cancel the original incident fields, as observed by Lenz's Law.

2. **Plane Wave**. This is the traditional method employed in shielding based on absorptions and reflections to attenuate and mitigate fields.

Both methods are equally valid so their fundamental physical concepts are presented.

5.2 MQS Method

The high frequency eddy current effects are well known as it is the same fundamental principle under which a transformer functions during a short circuit condition. Incident magnetic fields induce current in a shorted conductive loop and the current in turn generate counter fields that attempt to cancel the incident fields, as depicted by Fig. 5.2. This behavior is observed in the three-winding transformer shown in Fig. 4.16 as negligible amount of magnetic flux passes through the area enclosed by the shorted windings. Similar principle is present when the time-varying incident fields induce eddy currents in the shield. The eddy currents generate counter magnetic fields that cancels out the original incident fields. The shield thickness required in order to generate ample amount of eddy currents for proper field cancellation is directly proportional to the skin depth δ, which decreases with increasing frequency.

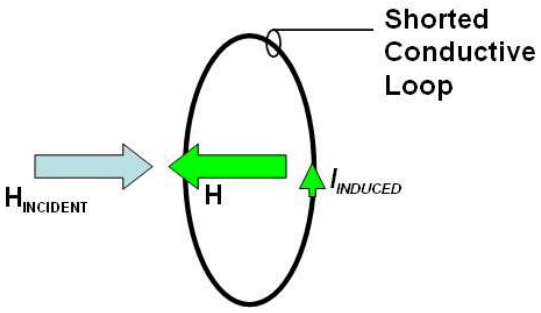

Figure 5.2: Incident magnetic field induces current in the shorted loop, which in turn generates an opposing magnetic field to cancel the original incident field.

Due to this proportionality, difficulty arises in shielding static to low frequency magnetic fields. The shield has to be thick enough so that the low frequency fields are not transmitted right through the shield. Matter of fact, for static fields, the skin depth is theoretically infinite, so that eddy currents are not induced at all. Thus, magnetic materials must be employed to provide a low-reluctance magnetic shunt path in order to divert the magnetic flux away from where they are not desired. An example of this concept is demonstrated by Fig. 5.3 that has an iron shield 'guiding' the static fields away from the region that is to the right of the shield.

To better understand the principle behind flux shunting, boundary conditions given by Eq. 5.1 are used on the field $\vec{H}_{e2}$ of Fig. 5.4, that is coming in contact with a magnetic material with assumed zero conductivity and high permeability [23].

Boundary Conditions:

$$\begin{aligned} B_{n1} &= B_{n2} \\ H_{t1} &= H_{t2} \end{aligned} \tag{5.1}$$

where:

$$\begin{aligned} B &= \mu H \\ \text{Subscript 1} &\equiv \text{Region external to the magnetic material} \\ \text{Subscript 2} &\equiv \text{Region internal to the magnetic material} \\ \text{Subscript } n &\equiv \text{Normal component of the field} \\ \text{Subscript } t &\equiv \text{Tangential component of the field} \end{aligned}$$

Field inside the material:

Let the field $\vec{H}_{e2}$ be defined as such:

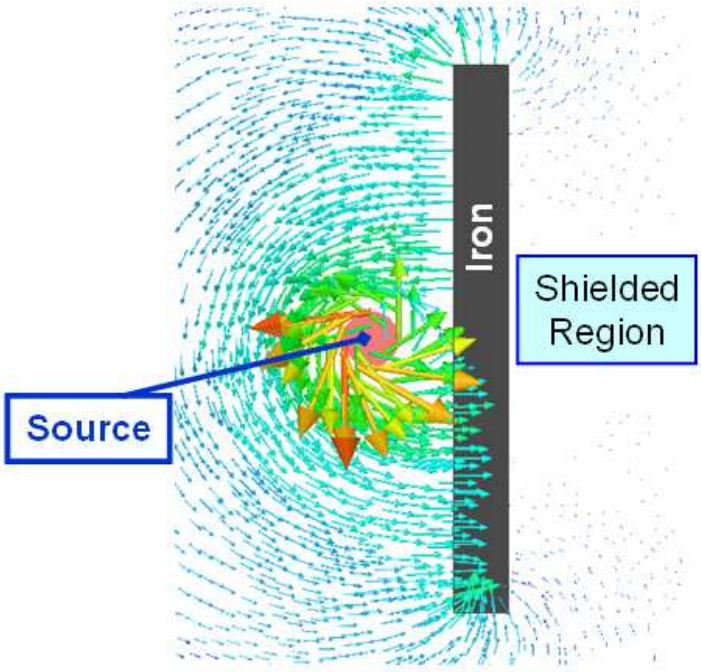

Figure 5.3: Use of magnetic materials to divert the fields away from where they are not desired.

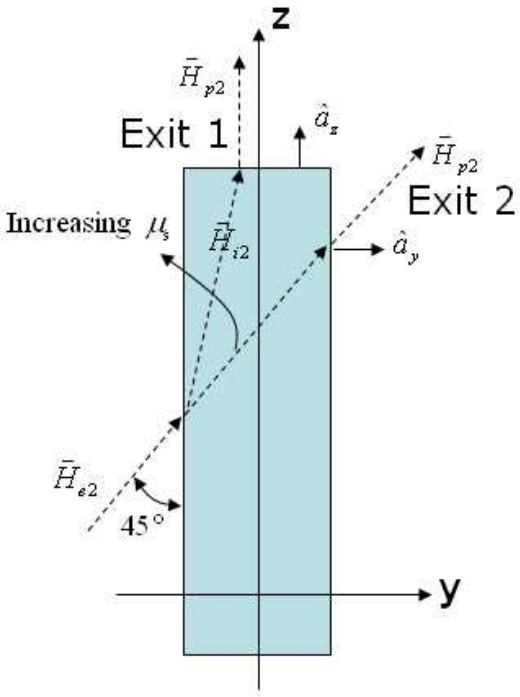

Figure 5.4: Understanding the principle behind flux shunting.

$$\vec{H}_{e2} = H_e\hat{a}_y + H_e\hat{a}_z \tag{5.2}$$

Applying the boundary conditions,

$$B_{ye} = B_{yi} \Rightarrow \mu_0 H_e = \mu_s\mu_0 H_{yi} \Rightarrow H_{yi} = \frac{H_e}{\mu_s} \tag{5.3}$$

$$H_{ze} = H_{zi} \Rightarrow H_{zi} = H_e \tag{5.4}$$

Thus,

$$\vec{H}_{i2} = \frac{H_e}{\mu_s}\hat{a}_y + H_e\hat{a}_z \tag{5.5}$$

$$\vec{B}_{i2} = \mu_s\mu_0\vec{H}_{i2} = \mu_0 H_e\hat{a}_y + \mu_s\mu_0 H_e\hat{a}_z \tag{5.6}$$

If $\mu_s >> 1$,

$$\vec{H}_{i2} \approx H_e\hat{a}_z \tag{5.7}$$

$$\vec{B}_{i2} \approx \mu_s\mu_0 H_e\hat{a}_z \tag{5.8}$$

The field $\vec{H}_{i2}$ is entirely tangential inside the material. In such a fashion, the magnetic material 'guides' the field away. When the field leaves the material through exit 1, the field $\vec{H}_{p2}$ is:

$$\vec{H}_{p2} = \frac{H_e}{\mu_s}\hat{a}_y + \mu_s H_e\hat{a}_z \tag{5.9}$$

$$\vec{B}_{p2} = \mu_0\vec{H}_{p2} = \frac{\mu_0 H_e}{\mu_s}\hat{a}_y + \mu_s\mu_0 H_e\hat{a}_z \tag{5.10}$$

If $\mu_s >> 1$,

$$\vec{H}_{p2} \approx \mu_s H_e\hat{a}_z \tag{5.11}$$

$$\vec{B}_{p2} \approx \mu_s\mu_0 H_e\hat{a}_z \tag{5.12}$$

The y component of the field has effectively vanished or has been attenuated. In case the shield material is relatively thin and the field manages to penetrate through the shield via exit 2, the field $\vec{H}_{p2}$ is found to be:

$$\vec{H}_{p2} = H_e\hat{a}_y + H_e\hat{a}_z \tag{5.13}$$

$$\vec{B}_{p2} = \mu_0\vec{H}_{p2} = \mu_0 H_e\hat{a}_y + \mu_0 H_e\hat{a}_z \tag{5.14}$$

Field $\vec{H}_{p2}$ is identital to $\vec{H}_{e2}$, which implies that if the incident field manages to

penetrate through the loss-less magnetic shield, it will exit without being attenuated. Thus it can be concluded that the shielding effectiveness increases with increase in shield permeability and thickness.

Magnetic material may also be used in shielding for fields of higher frequencies in order to provide additional protection. However, magnetic materials suffer from multiple drawbacks which include:

1. Permeability, μ, dependent on frequency
2. μ depends on field strength. In other words, with high enough excitation, the material is easily saturated.
3. Sensitive to machining
4. Sensitive to operating conditions such as temperature
5. Expensive
6. Nonlinear
7. Large and Heavy

To avoid these drawbacks, alternate methods are often employed that include:

1. Increase distance between source and receiver as the field strength H is inversely proportional to the cube of distance $\left(H \approx \frac{k}{r^3}\right)$.
2. Use shorted turn around object to produce a counter field
3. Rotate the source or receiver
4. Move the position of conductors
5. Redesign

An example of how rotating a device may reduce coupling between them is shown in Fig. 5.5 and Fig. 5.6 [62, 63].

The mutual inductance, M_1 and M_2, that exists between the two capacitors and the inductor have been reduced by rotating the windings by 90° in Fig. 5.5. Similarly, mutual inductance, M_3, between two capacitors has been reduced by simply rotating one of the capacitors to be physically perpendicular to the other in Fig. 5.6.

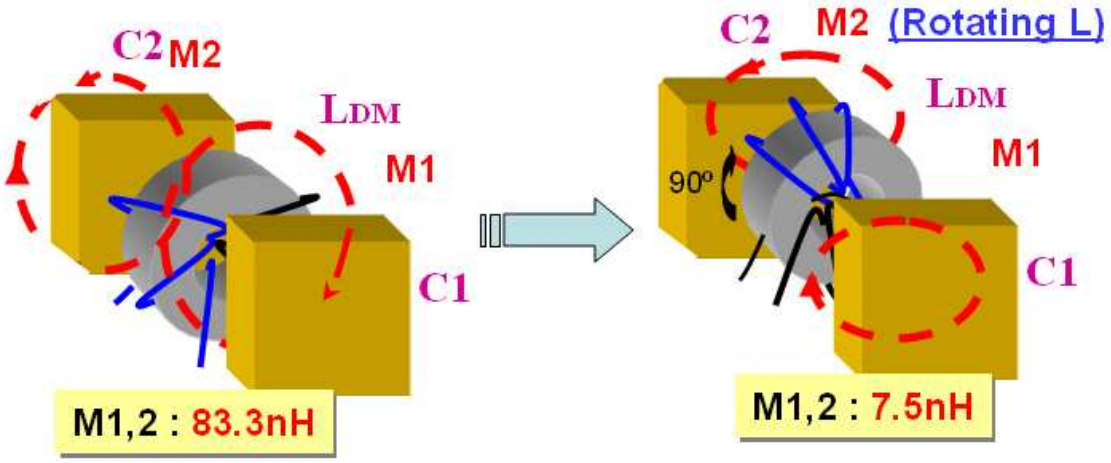

Figure 5.5: Decrease in mutual coupling M_1 and M_2 by rotating the winding of the inductor by 90° around the core.

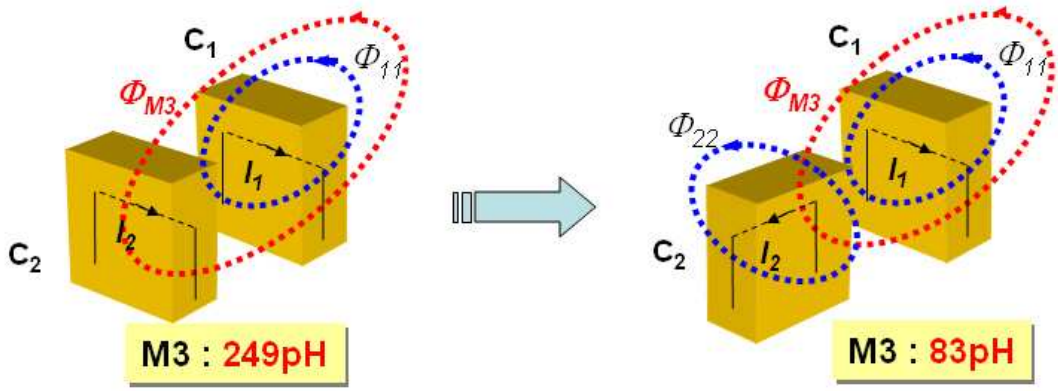

Figure 5.6: Decrease in mutual coupling M_3 between two discrete capacitors by rotating one of the capacitors.

5.3 Plane Wave Method

Shield design can also be undertaken from the traditional plane wave method. Although near-field regions do not exhibit strong plane wave behavior, some of the concepts are still valid. Much of the discussions in this section are found in [22, 64]. They are included in this work, however, for completeness and in order to acquire insight into the design process. Shielding effectivenss is defined by Eq. 5.15.

$$S = 20log\frac{H_0}{H_t} = A + R + B \tag{5.15}$$

where:

$H_0 \equiv$ Incident field strength

$H_t \equiv$ Field strength of transmitted wave out of the shield

$A \equiv$ Absorption loss

$R \equiv$ Reflection loss

$B \equiv$ Correction factor to account for multiple reflections

As the field strength, H, are difficult to measure experimentally, shielding effectiveness is found by the summation of absorption and reflection losses that are derived based on the material properties.

5.3.1 Absorption Loss

Absorption loss is the primary mechanism through which magnetic fields are attenuated. The decay of the field, H_0, in Fig. 5.7 is expressed by Eq. 5.16.

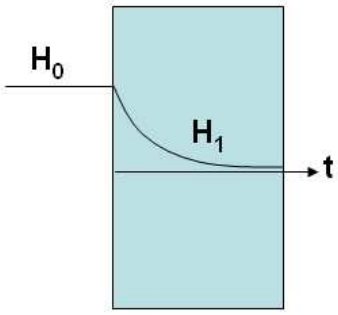

Figure 5.7: Magnetic field decays as it passes through the shield due to absorption loss.

$$H_1 = H_0 e^{-t/\delta} \tag{5.16}$$

where:

$H_1 \equiv$ Wave intensity at distance t within the medium

$\delta = \sqrt{\frac{2}{\omega\mu\sigma}} \equiv$ skin depth in meters

The decay in the medium occurs due to ohmic losses and heating from the induced eddy currents. The loss encountered, known as absorption loss, is given by Eq. 5.17.

$$\begin{aligned} A &= 20\left(\frac{t}{\delta'}\right) log_{10}(e) \\ &\approx 3.34t\sqrt{f\mu_r\sigma_r} \end{aligned} \tag{5.17}$$

where:

t and δ' are in inches

$\sigma_r \equiv$ relative conductivity in comparison to copper

5.3.2 Reflection Loss

Reflection of electromagnetic fields occur at the interfaces of two different medium, such as the air-shield or shield-air boundary, as shown in Fig. 5.8. A wave impedance and characteristic medium/shield impedance are defined by Eq. 5.18 and Eq. 5.19 respectively. Based on these two impedances, reflection loss is defined by Eq. 5.20. Reflection loss quantifies how much of the electromagnetic fields are attenuated via reflections occuring at the interfaces of the media. The intensity of the magnetic field inside the medium, H_1, and intensity of the field that has been transmitted through the medium, H_t, as shown in Fig. 5.8, are a function of characteristic medium impedances, Z_1 and Z_2.

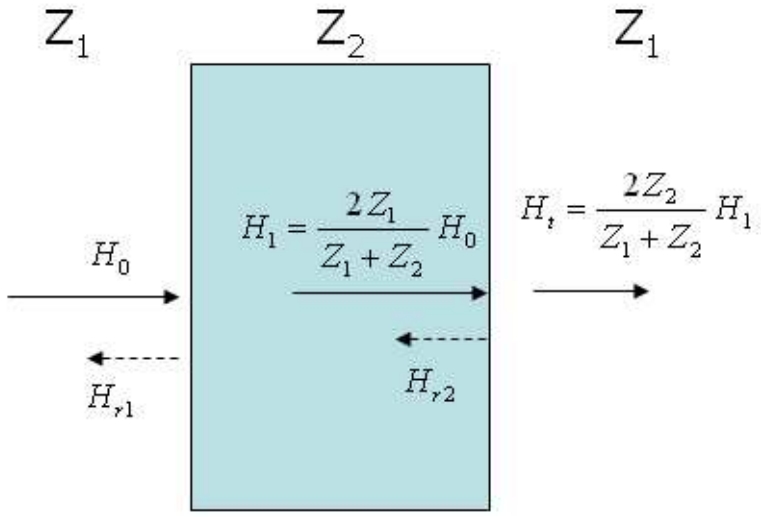

Figure 5.8: Magnetic fields encounter reflection at the interface of two different medium.

$$Z_w = \frac{E}{H} \tag{5.18}$$

$$Z_0 = \sqrt{\frac{j\omega\mu}{\sigma + j\omega\epsilon}} \tag{5.19}$$

$$R = 20log\frac{|Z_w|}{4\,|Z_s|}\ \text{dB} \tag{5.20}$$

where:

$Z_s \equiv$ Characteristic shield impedance

For the near field assumption, $r < \lambda/2\pi$, the wave impedance due to a point source of the magnetic field may be approximated as:

$$|Z_w|_m \approx 2\pi f\mu r \tag{5.21}$$

where:

$r \equiv$ distance from source to shield

Then the reflection loss for magnetic fields is expressed by Eq. 5.22.

$$R_m \approx 14.6 + 10log\left(\frac{fr^2\sigma_r}{\mu_r}\right) \tag{5.22}$$

where r is in meters

5.3.3 Correction Factor for Multiple Reflections

Most of the incidient magnetic fields pass through the air-to-shield interface in Fig. 5.8. This is because the characteristic impedance of the shield, Z_2, is typically much smaller than the characteristic impedance of the air, ($Z_1 \approx 377\ \Omega$), such that $H_1 \approx 2H_0$. The greatest amount of reflection of magnetic fields occur at the second boundary, or shield-to-air interface. So if the shield is thin enough, the field will not be adequately attenuated through absorption loss before it encounters the second boundary, upon which point, majority of the fields will reflect back to the first boundary. There at the first boundary, the field will be reflected back again for the same reason. In such a way, multiple reflections are encountered, as shown in Fig. 5.9.

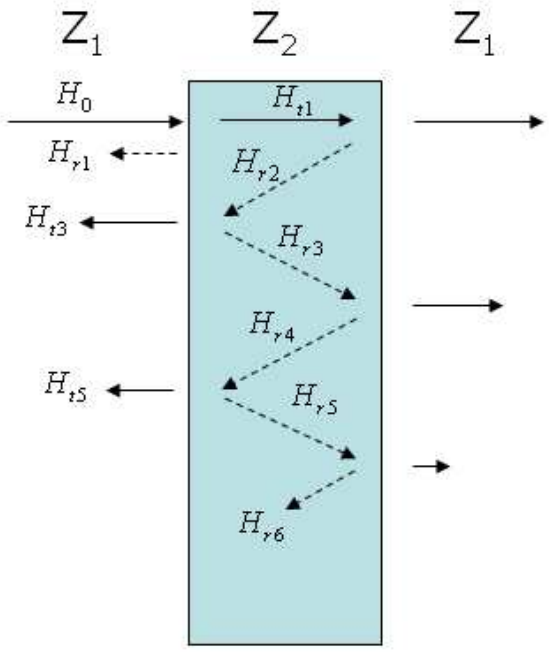

Figure 5.9: Multiple reflections are present due to thin shield and not adequate amount of absorption loss present.

In order to take the multiple reflections into account, the expression given

by Eq. 5.23 are added onto the absorption and reflection loss of previous two sections. However, if the absorption loss exceeds 9 dB, then the correction factor, B, is assumed to be negligible and multiple reflections do not need to be taken into account.

$$B = 20log\left(1 - e^{-2t/\delta}\right) \text{ dB} \tag{5.23}$$

5.4 Shielding Considerations

The primary objectives of a shield in this work are to adequately attenuate electromagnetic fields with the least amount of losses introduced by the shield and least amount of field distortions taking place in the shielded device. In order to meet these objectives, a study of potential shield materials is conducted.

When shielding lossy devices such as a transformer, the shielding structure should not only be able to attenuate and/or mitigate electromagnetic fields, but it should also facilitate in an efficient extraction of the high amount of heat that is generated by the transformer. One way of achieving this is by minimizing the number of different materials that exists between the transformer and the heat sink. The largest thermal resistance is encountered at the interfaces between two materials, due to poor mechanical or chemical adherence and thermal expansion mismatch that leads to debonding. Thus, ideally, the heat sink should be right next to the transformer, acting as a shield as well. However, in order to minimize the degree of conductive coupling with the other circuit components that are also sharing the heat sink, it may be necessary to introduce a separate material for shielding. If this should be necessary, then a material with the highest thermal conductivity should be selected.

In application, it is not possible to create a shield that encloses a device entirely, as slots and holes are required in order to establish connections to the rest of the circuit. So, the breaks in the shield have to be appropriately placed at locations where the least amount of field attenuation is required.

Further, slots and holes have to be sized as small as possible and well distributed such that their presence make the least amount of impact on the distribution of the induced eddy currents. Significant disruptions in the natural pathway of the eddy currents will result in an ineffective cancellation of the incident magnetic fields. This concept is depicted in Fig. 5.10. The introduction of a wide slot in the shield affects the path that the current would have taken in a solid shield.

By distributing the holes/slots, a more uniform current density can be achieved throughout the shield.

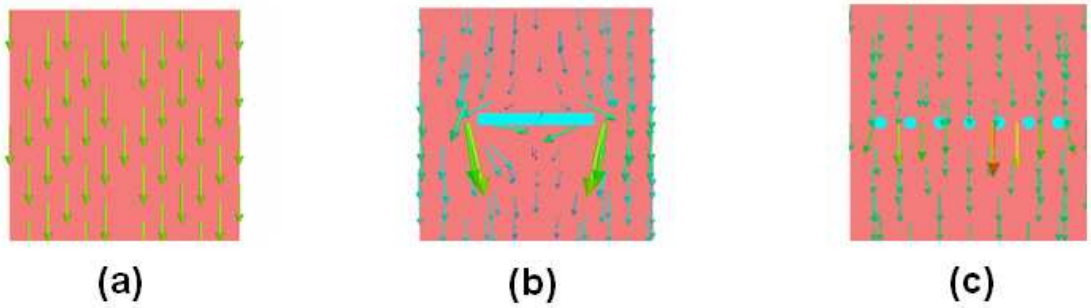

Figure 5.10: The induced current flow in a) a solid shield, b) a shield with a wide slot, and c) a shield with distributed holes.

5.5 Energy Distribution in a Shielded Transformer

Eddy current losses are not only introduced in the shield, but the presence of the shield also changes the losses in the shielded structure itself. The change in the eddy current losses is the result of the shield distorting the electromagnetic field distribution in the structure. So, when selecting a shield material, a study of the energy or loss distribution in the shield and among the conductive elements of the structure has to be undertaken.

The expression given by Eq. 5.24 is used in calculating the total energy in a one second period for a shielded transformer. The expression is derived under primary winding excitation at the rated current, with the other windings shorted. The current density and magnetic fields are given in RMS. The first term is the energy storage due to magnetic fields. The second and third terms are energy dissipated in the windings and the shield respectively. The first term may be negligible in comparison to the second and third terms, but it is included in the expression in order to observe the impact the shield has on the leakage reactance of the transformer. FEM is used in calculating the energy distribution as the field distributions are way too complex for accurate analytical calculations. The core-losses are not taken into account due to the fact that 1) the non-linear hysteresis loss is not modeled in most eddy-current FE solvers, and 2) the conductivity of the ferrite core is relatively much lower such that eddy current losses are negligible in comparison with the windings and the shield. Further, energy storage due to electric fields is also not included, as

most FE software do not have the capability to model both electric and magnetic energy storage.

$$U_{total} = \frac{1}{2}\int_{All} B \cdot H d\Omega + \frac{1}{2\sigma}\int_{Windings} J \cdot J^* d\Omega_W + \frac{1}{2\sigma}\int_{Shield} J \cdot J^* d\Omega_S \quad (5.24)$$

The eddy current losses in the shield due to proximity effect may also be calculated using Eq. 2.24 in combination with Eq. 2.32 by setting $H_{s2} = 0$, as the fields do not penetrate through the shield.

5.6 Case Study: Shield Design

5.6.1 Potential Shield Materials

Five metals are selected as potential shield material in Table 5.2. The copper is annealed and the aluminum is of the soft kind. Kovar is an alloy of primarily iron, nickel and cobalt, with very small percentage of carbon, silicon and manganese. The skin-depth of each of the five materials are evaluated at the operating frequency of 750kHz, along with other parameters that are critical in selecting an appropriate shield material.

Table 5.2: Listing of potential shield materials.

Material	σ_r	μ_r	Density	Thermal Cond.	δ (750 kHz)
Copper	1.00	1.00	8.96 g/cm^3	401 W/(m·K)	3 mils
Aluminum	0.61	1.00	2.70 g/cm^3	237 W/(m·K)	3.85 mils
Nickel	0.20	100	8.91 g/cm^3	91 W/(m·K)	0.67 mils
Iron	0.17	700 (1 MHz)	7.89 g/cm^3	80.4 W/(m·K)	0.28 mils
Kovar	0.035	700 (1 MHz)	8.36 g/cm^3	17.3 W/(m·K)	0.605 mils

5.6.2 Plane Wave Losses

The skin depth, δ, the absorption loss, A, and the reflection loss, R, of the five materials are plotted in Figs. 5.11, 5.12, and 5.13 respectively in terms of frequency of the incident wave. Absorption loss is, more or less, inversely proportional to the skin depth. Thus the iron seems to be the ideal choice for achieving the highest absorption loss, followed by kovar and nickel, and copper and aluminum. However, the order is pretty much reversed, with the exception of kovar, in achieving the

highest reflection loss. But as absorption is the primary mode of attenuation for magnetic fields, maximizing reflection loss is not a priority.

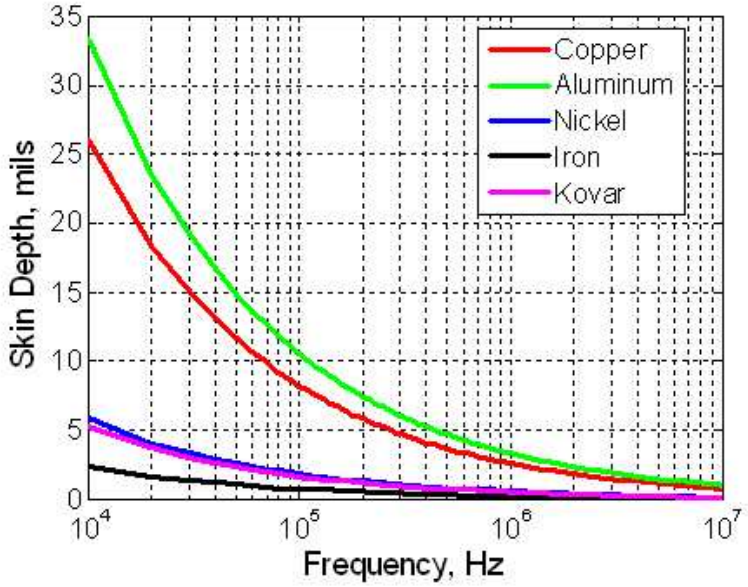

Figure 5.11: Skin depth vs. frequency of the five potential shield materials.

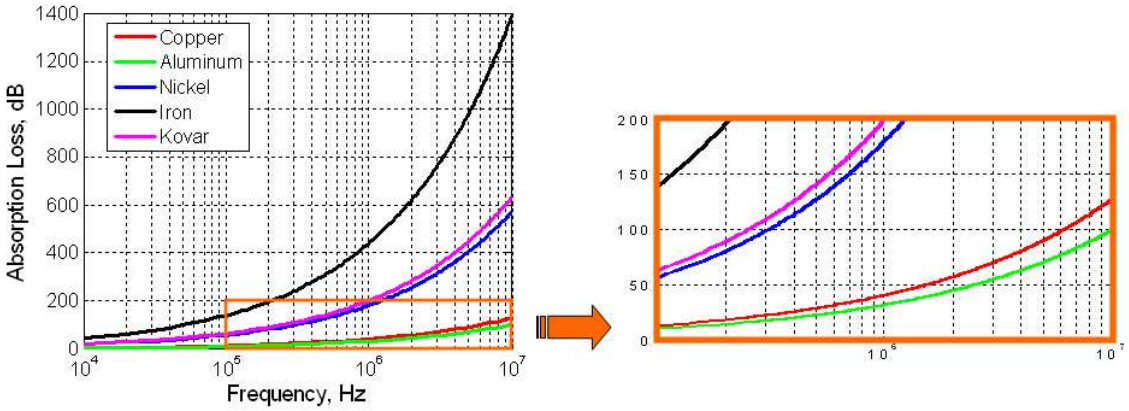

Figure 5.12: Absorption loss vs. frequency of the five potential shield materials at thickness $t = 12$ mils.

5.6.3 Eddy Current Losses Due to Shield Material

An enclosed box shield housing the three-winding planar transformer, as shown in Fig. 5.14, is simulated in Maxwell 3D using the Eddy Current solver. The primary

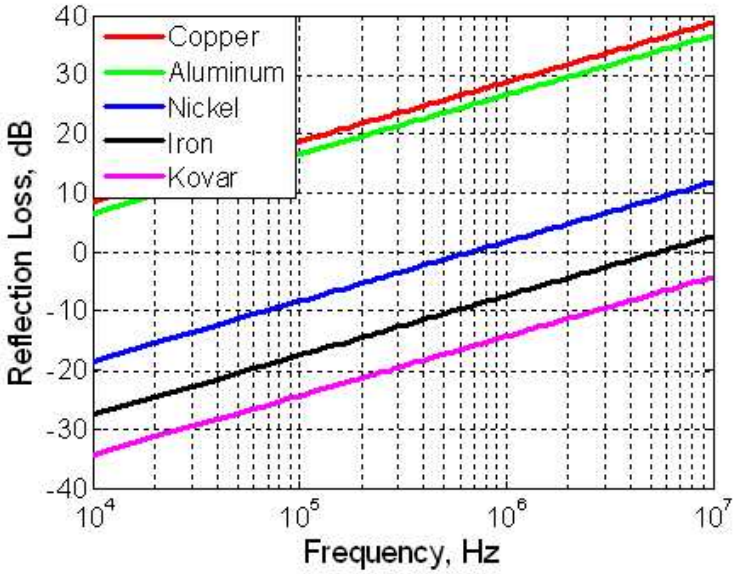

Figure 5.13: Reflection loss vs. frequency of the five potential shield materials at a shield distance of $r = 200$ mils.

objective is to determine what material causes the least amount of distortion and losses, and to see how the losses distribute between the windings and the shield. The shield is 20 mils thick, or about 5δ of aluminum at the rated frequency, to ensure that least amount of field penetration occurs through the shield among all five materials. Adequate room is allowed on top of the transformer in order to enclose a PCB circuit as well that interfaces the transformer with the rest of the converter.

The total energy in the transformer is a summation of stored magnetic energy, winding loss and shield loss as given by Eq. 5.24. Stored electric energy and core losses are not modeled in this solver. The energy distribution among the three entities is shown in Table 5.3 for the short circuit condition.

Maxwell 3D has trouble simulating the shorted condition within a 1% energy error for some of the materials because the number of tetrahedrons required for the problem exceed 400,000. To solve such a large sized problem is beyond the capability of the computing resources available to most designers. So the error tolerance is raised to 5% in the simulations for all five materials. The large amount of required tetrahedrons is due to the skin depth of some of the materials that are much smaller than the overall geometry of the mediums through which the fileds are propagating. As an example, the complexity and the size of the mesh used in solving the problem for the kovar shield is depicted by Fig. 5.15 which only shows the mesh

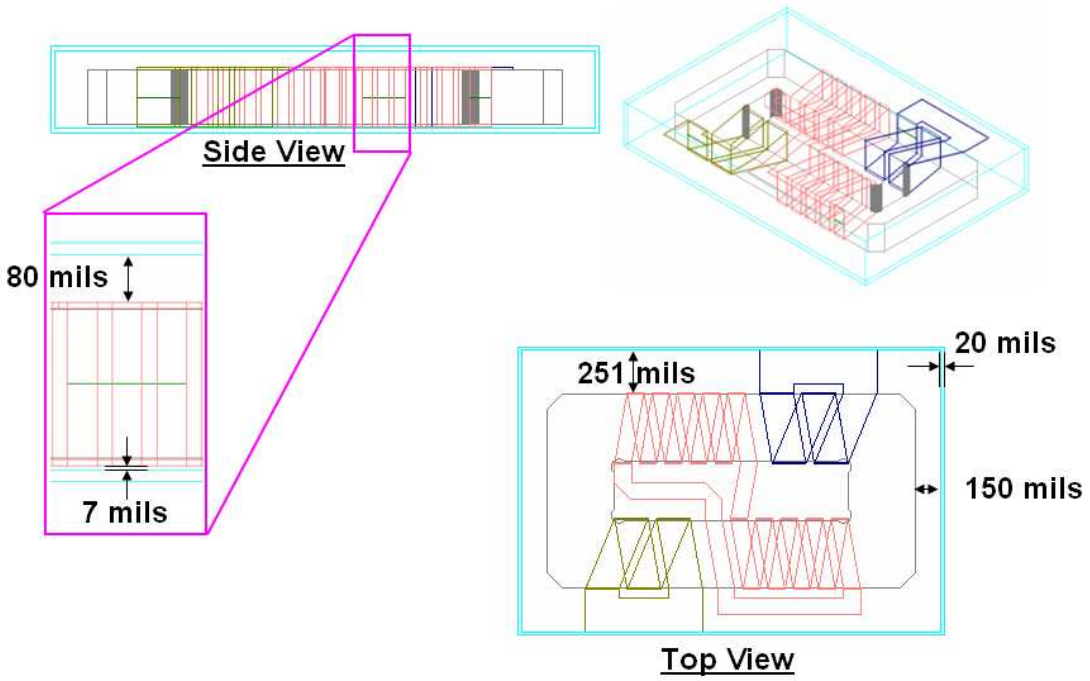

Figure 5.14: Enclosed box shield housing the planar transformer to study distortion, loss, and loss distribution due to each of the five shield materials in Maxwell.

Table 5.3: Loss distribution in presence of the enclosed shield for the five shield materials.

	Stored Energy	Winding Loss	Shield Loss
Copper	46.0 μJ	2.32 J	0.96 J
Aluminum	46.1 μJ	2.31 J	1.39 J
Nickel	111 μJ	3.64 J	5.63 J
Iron	280 μJ	9.59 J	2.94 J
Kovar	280 μJ	9.61 J	14.9 J
Total Magnetic Energy Error $< 5\%$			

on the outer shield surfaces. About 314000 tetrahedrons are used in solving the problem for the kovar shield within a 5% error.

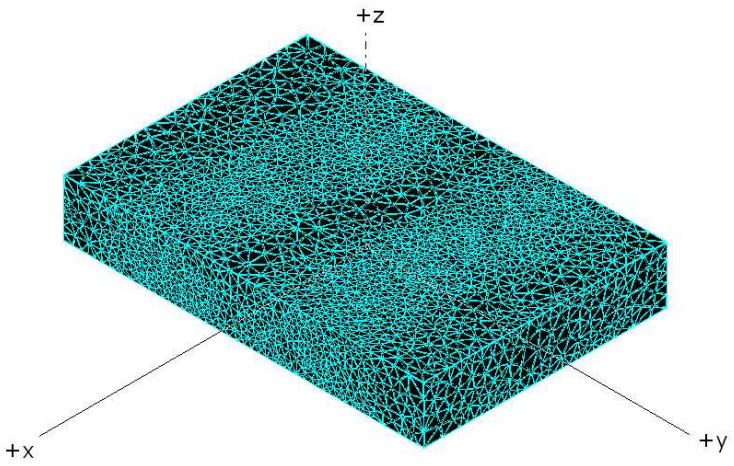

Figure 5.15: The plot of the mesh on the outer surfaces of the kovar shield.

The losses quoted in the table should not be taken as an actual loss in the shield and windings, but rather should be used as a quantitative comparison between the five materials. The energy error calculation in a FE eddy current solver is based on satisfying one of Maxwell's equations, $\nabla \cdot B = 0$. The software converges upon this expression without taking into account the energy dissipation due to eddy current losses. As a result, significant deviations in the losses could result with small changes in the magnetic energy error. For a consistent set of errors, comparisons between the results are still valid in order to evaluate the appropriateness of the shield material.

It is obvious from the table that copper and aluminum experience the least amount of energy loss. Pie and bar graphs are provided based on the table in order to present the data in a more coherent manner. The distribution of losses and total relative losses for the short circuit condition are shown in Fig. 5.16 and Fig. 5.17 respectively. In the pie graphs, the stored energy is included as part of the energy distribution, but it is visually negligible in comparison to the other two losses.

The pie graphs reveal that copper and iron have the best loss distribution, where the best distribution is defined as the one with relatively least amount of loss occuring in the shield. However, the bar graphs reveal that the highest total loss are encountered by kovar followed by iron.

The parameters of the transformer's extended cantilever model is provided in Table 5.4 for the five shield materials. The parameters without the presence of the shield is also listed in order to compare the degree to which the shield materials are

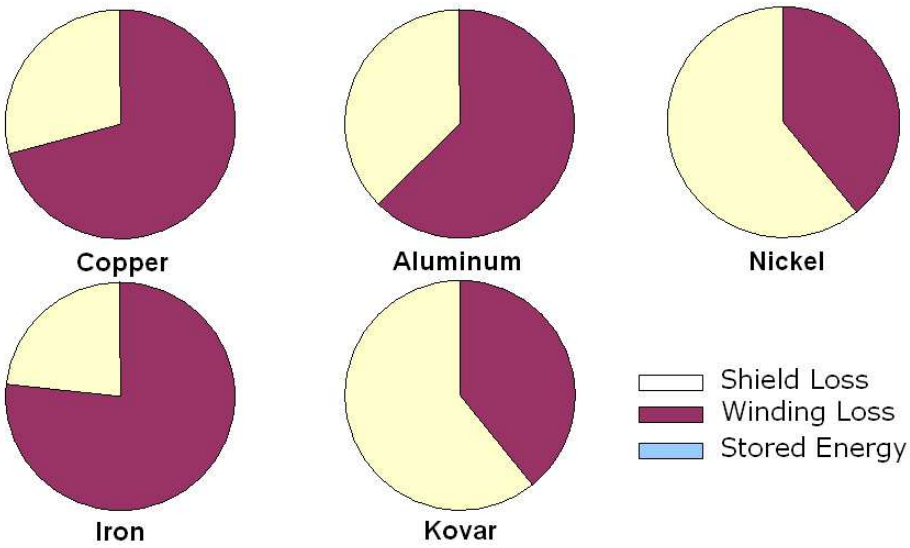

Figure 5.16: Loss distribution under short circuit condition for the five shield materials.

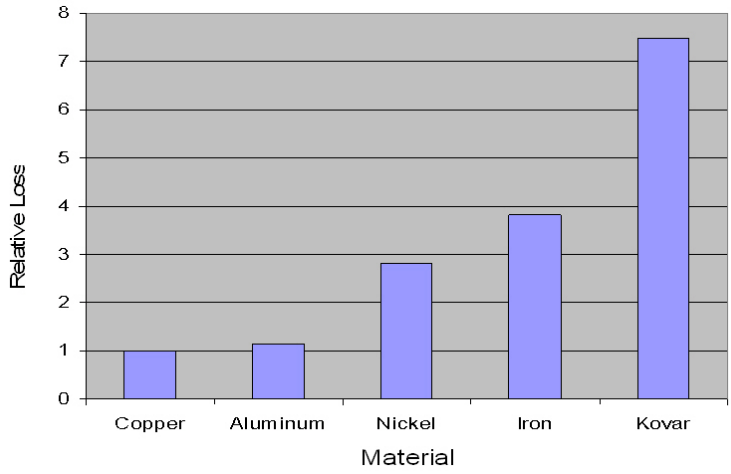

Figure 5.17: Total loss in the short circuit simulation relative to copper for each of the five shield materials.

distorting the magnetic fields.

Table 5.4: Effect of the enclosed shield on the parameters of the extended cantilever model with the five shield materials.

Ext. Param.*	L_{11}	l_{12}	l_{13}	l_{23}	$n_{2_{eff}}$	$n_{3_{eff}}$
No Shield	43.4	6.15	5.79	-47.8	0.194	0.195
Copper	42.9	1.98	1.88	-71.2	0.198	0.198
Aluminum	42.8	1.82	1.82	-35.5	0.198	0.198
Nickel	43.5	7.69	7.19	493	0.193	0.194
Iron	44.7	19.9	16.9	-833	0.183	0.186
Kovar	44.7	19.9	16.9	-833	0.183	0.186

*Unit is in μH

From the table, it is concluded that the copper and nickel shields have the least amount of impact on the parameters when compared against the no shield scenario. Iron and kovar both exhibit the exact same level of distortion because they are both simulated with the same value of permeability ($\mu_r = 700$).

After considering the five potential materials as a shield for the transformer, **copper** is selected as the optimal choice. The five materials were considered for their capability in attenuating high frequency magnetic fields, their effect on interwinding coupling fields, the loss distribution and amount of total ohmic losses.

5.6.4 Field Concentration on the Shield Surfaces

A knowledge of the field concentration on and around the shield is useful in order to determine appropriate placement of other noise-sensitive circuit components around the transformer. For instance, it would be highly undesirable to place a current sensor at a location where the magnetic fields radiating from the transformer may influence or distort the readings.

A logarithmic plot of the magnitude of the H-field is plotted on the surfaces of the copper shield in Fig. 5.18. From the figure it is clear that the least amount of field is observed on the XZ faces of the box shield. The field concentration is relatively pretty high on the rest of the four faces of the shield. So in order to minimize coupling with the transformer, circuit components should be placed in front of the XZ faces, or in the direction of the Y-axis for the coordinate system shown.

To quantify the role played by the XZ faces of the shield, those two faces are taken away as portrayed in Fig. 5.19. The energy distribution is given by Table 5.5 and compared against the energy distribution of the case in Fig. 5.18 with the

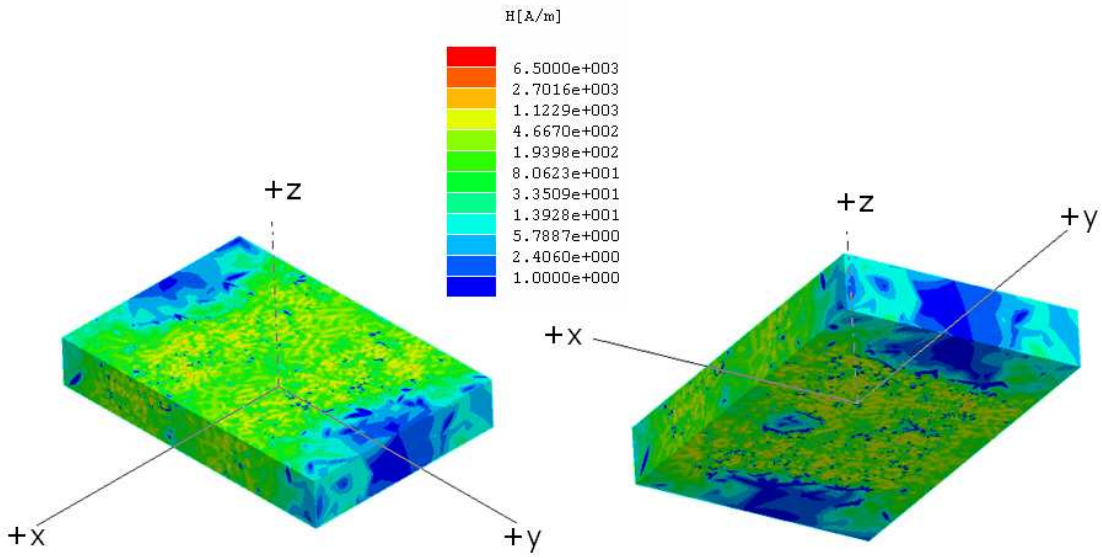

Figure 5.18: Field concentration on the surfaces of the copper shield.

faces intact. The change in the total energy, and energy distribution is relatively negligible with and without the XZ faces.

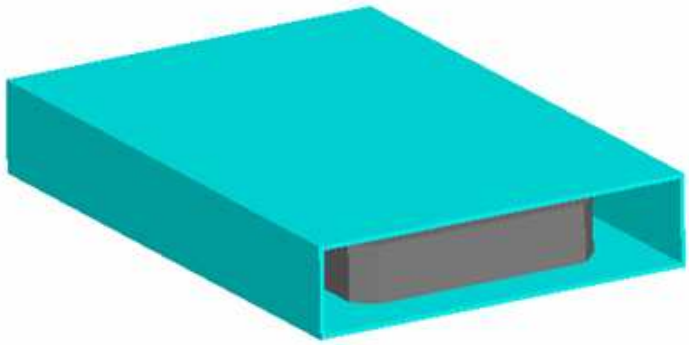

Figure 5.19: The box shield without the XZ faces.

5.6.5 Eddy Current Losses Due to Shield Dimension

A parametric study usinng FEM is conducted on the size of the shield in order to observe the impact that the dimension has on the energy distribution. A coordinate system with the origin at the volumetric center of the core window is shown in Fig. 5.20 with the box shield. The study is conducted on a copper shield by increasing the shield dimensions in increments on all three axis while keeping the

Table 5.5: Energy distribution with and without the XZ faces on the copper box shield.

Case	Stored Energy	Winding Loss	Shield Loss
With XZ faces	44.5 μJ	3.14 J	1.51 J
Without XZ faces	44.6 μJ	3.09 J	1.47 J
			Energy Error $< 1\%$

shield thickness constant. The dimension shown in Fig. 5.14 is taken as the base condition with $\Delta x = 0$, $\Delta y = 0$, and $\Delta z = 0$. The increments are added equally on both sides of an axis. In other words, for $\Delta x = 10$ mils, 5 mils is added on $+x$ side, and 5 mils on the $-x$ side.

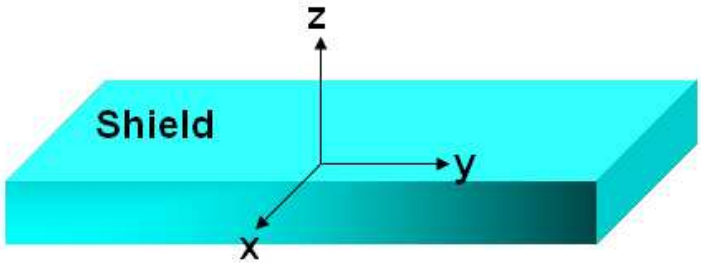

Figure 5.20: The coordinate system used in the shield design.

The model is simulated within 1% energy error, as the copper shield's skin depth is high enough for this to be possible. For the X- and Z-axis, increments of 10, 20, 100 and 200 mils are added. For the Y-axis, increments of only 100 and 200 are used, as the field concentration on the XZ faces of the shield is negligible as observed in the previous section. The results of the simulations are manifested by Table 5.6-5.8.

Table 5.6: Parametric study of the shield dimension on the X-axis

Δx	Stored Energy	Winding Loss	Shield Loss	Total Energy
0	44.7 μJ	3.00 J	1.39 J	4.39 J
10	44.8 μJ	3.07 J	1.44 J	4.51 J
20	45.1 μJ	3.05 J	1.39 J	4.44 J
100	46.8 μJ	2.93 J	1.23 J	4.16 J
200	48.1 μJ	2.95 J	1.23 J	4.18 J

Table 5.7: Parametric study of the shield dimension on the Y-axis

Δy	Stored Energy	Winding Loss	Shield Loss	Total Energy
0	44.7 μJ	3.00 J	1.39 J	4.39 J
100	44.5 μJ	3.15 J	1.48 J	4.63 J
200	44.5 μJ	3.10 J	1.51 J	4.61 J

Table 5.8: Parametric study of the shield dimension on the Z-axis

Δz	Stored Energy	Winding Loss	Shield Loss	Total Energy
0	44.7 μJ	3.00 J	1.39 J	4.39 J
10	46.3 μJ	3.21 J	1.39 J	4.60 J
20	48.6 μJ	3.14 J	1.25 J	4.39 J
100	60.7 μJ	3.27 J	0.92 J	4.19 J
200	73.3 μJ	3.58 J	0.73 J	4.31 J

From these three tables, it can be concluded that, in general, the total eddy current losses decrease as the shield size is increased. The size increase in the x-direction yields decrease in the shield loss, with negligible decrease in the winding loss. The decrease in shield loss is attributed to the fact that in the near-field region, the magnetic field is proportional to either $1/r^2$ (when electric field is dominant) or $1/r^3$ (when magnetic field is dominant) of the distance from the source. So farther the shield is from the source, less loss it experience due to eddy currents induced by the incident magnetic fields.

The size increase in the y-direction actually results in increase of the losses. This is attributed to the fact that although there are negligible field concentration on the XZ faces of the shield, by increasing the shield on the y-direction, the total area of all the other faces increases. Thus the volume occupied by the magnetic fields increases for a given skin depth, resulting in greater losses.

In the z-direction, although the winding loss in general is increasing, the losses in the shield are steadily decreasing. As the largest losses are occuring in the XY faces of the shield, the most significant decrease in the shield loss is encountered by increasing the shield in the z-direction. The winding loss is converging upon the value of 5.04 J as calculated, without the presence of any shield, in Table 2.1. The total loss barely changes, but the energy distribution has been significantly impacted.

Thus it can be concluded that the shield in the y-direction should be kept as small as possible, while the dimension should be maximized, depending on the

design constraints, in the other two directions.

5.6.6 Use of Magnetic Material for Further Shielding

Further field attenuation can be achieved by employing thin layers of ferrite-types directly on top and bottom of the transformer windings. The two materials that will be studied are,

1. Ferrite Polymer Composite (FPC) distributed by EPCOS
2. Ferrite, with similar properties as the core

The FPC is modeled in FEM with relative permittivity, $\epsilon_r = 100$, relative permeability, $\mu_r = 17$, and conductivity, $\sigma = 0.08$ S/m. The ferrite is modeled with the same properties as the transformer core ($\epsilon_r = 1$, $\mu_r = 595$, and $\sigma = 0.1$ S/m). The planar dimensions of the two materials are portrayed in Fig. 5.21 which are the same as the core. The FPC material, however, does not have a window. The thickness of both materials are 3 mils. There is an air separation of 2 mils between the windings and the materials in the model.

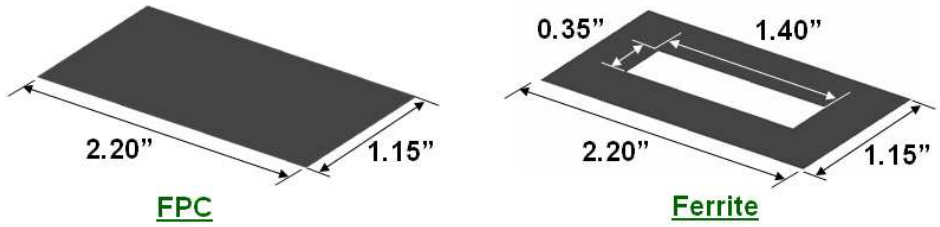

Figure 5.21: The dimensions of the two ferrite-types used to provide additional shielding.

The primary mode of field attenuation in these two magnetic materials is through shunting or guiding, as eddy current losses are negligible. This is due to the fact that the skin-depth of these materials are much larger than the actual dimension of the materials. The general expression for the skin depth is given as,

$$\delta = \frac{1}{\omega\sqrt{\frac{\mu\epsilon}{2}\left[\sqrt{1+\left(\frac{\sigma}{\omega\epsilon}\right)^2}-1\right]}} \tag{5.25}$$

For materials with,

$$\frac{\sigma}{\omega\epsilon} >> 1 \tag{5.26}$$

The skin-depth is approximated with,

$$\delta = \frac{1}{\sqrt{\pi f \mu \sigma}} \tag{5.27}$$

So for the FPC, the skin depth is calculated to be 75.3 mm or about 3 inches, and for the ferrite, the skin depth is 498 mm, or about 20 inches. These numbers are much larger than the 3 mils thickness of the materials. Thus, attenuation is achieved through guiding the fields away from the regions where they are not desired.

Using a copper shield with the dimension given by Fig. 5.14, the two materials are applied one at a time. Four simulations are conducted. The first one comprised of applying the FPC only to the windings on top of the transformer. In the second simulation, the FPC is applied to the windings on both top and bottom of the transformer. Similar process is repeated for the ferrite in setup 3 and 4. The field concentration on the materials, and on the surfaces of the shield are depicted by Figs. 5.22- 5.25. The summary of the energy distributions from the four simulations, and the base case without the additional shielding is provided in Table 5.9.

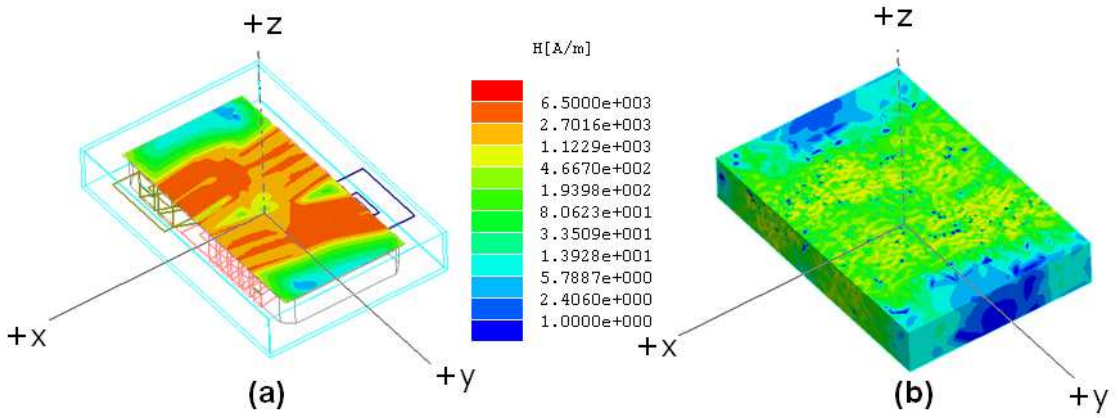

Figure 5.22: Setup 1: Field concentrations on a) surface of the FPC and b) surfaces of the shield, with FPC applied to windings on top of the transformer only.

From observing the four plots and the energy distribution given in the table, it can be concluded that the FPC material makes a negligible impact on attenuating magnetic fields and subsequently in reducing shield losses. The ferrite makes the largest impact, but the winding loss significantly goes up. Further, the addition of the ferrite on the bottom of the transformer in setup 4 does not reduce the shield loss

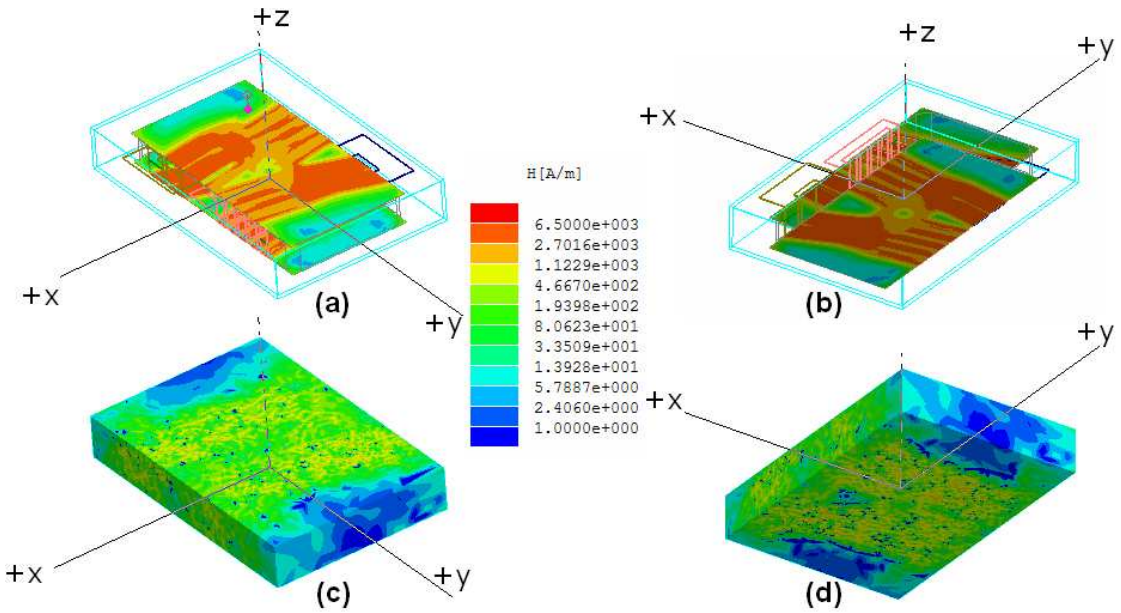

Figure 5.23: Setup 2: Field concentrations on a) surface of the top FPC, b) surface of the bottom FPC, c) surfaces of the shield around the top side, and d) surfaces of the shield around bottom side, with the FPC applied to windings on both top and bottom of the transformer.

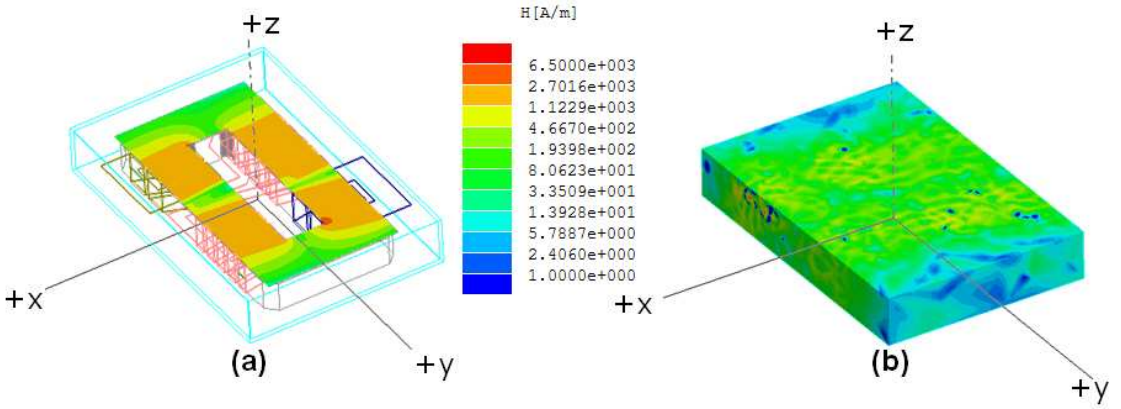

Figure 5.24: Setup 3: Field concentrations on a) surface of the ferrite and b) surfaces of the shield, with the ferrite applied to windings on top of the transformer only.

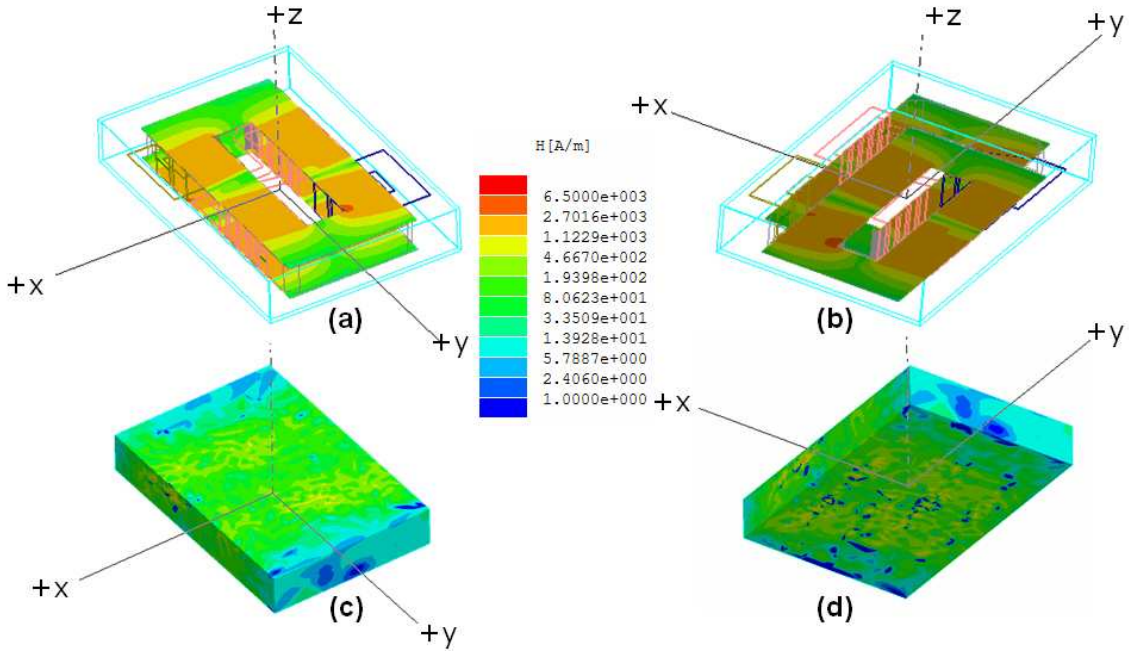

Figure 5.25: Setup 4: Field concentrations on a) surface of the top ferrite, b) surface of the bottom ferrite, c) surfaces of the shield around the top side, and d) surfaces of the shield around bottom side, with the ferrite applied to windings on both top and bottom of the transformer.

Table 5.9: Energy distribution of the four simulations.

Setup	Stored Energy	Winding Loss	Shield Loss	Total Energy
Without FPC/Ferrite	44.5 μJ	3.14 J	1.51 J	4.65 J
1	51.3 μJ	3.17 J	1.41 J	4.58 J
2	58.7 μJ	3.36 J	1.25 J	4.61 J
3	151 μJ	6.06 J	0.840 J	6.90 J
4	267 μJ	8.07 J	0.601 J	8.67 J

with the same order as observed for setup 3. From a thermal perspective, addition of ferrite type material on the bottom where the heat sink will be mounted is also not a good idea because thermal conductivity of ferrite is only 3 to 5 W/mK, and the two additional interfaces introduced by ferrite could significantly raise the thermal resistance.

So in conclusion, a magnetic material with the higher permeabilty at the intended frequency range provides the better field attenuation at the cost of a higher winding loss. The material should only be applied to the top of the transformer. The leakage energy also increases significantly in setup 3 and 4, but it is still smaller than the transformer without any shield at all as modeled in Chapter 4.

5.6.7 Shield Structure

Based on the study, two shield structures are proposed to provide electromagnetic shielding as depicted in Fig. 5.26. The first one encloses the interfacing PCB circuit, while the second one has the PCB board external to the shielded structure. The second structure has essentially the same internal configuration as the first one.

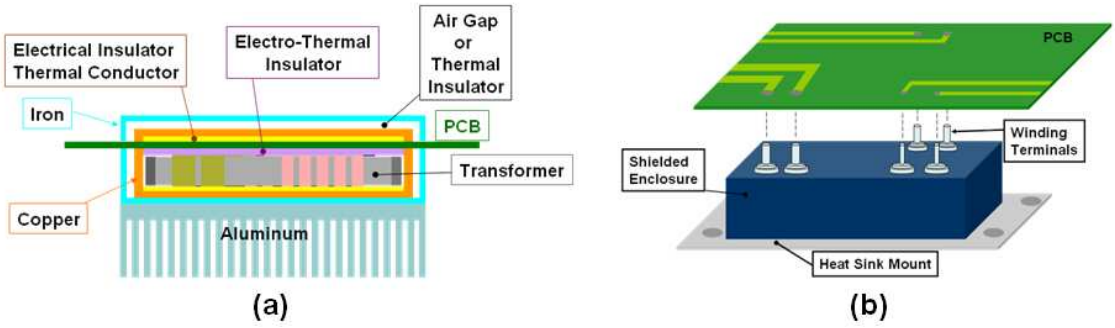

Figure 5.26: Shield structure that a) encloses the transformer and the interfacing PCB circuit and b) encloses only the transformer.

The copper layer forms the first line of defense that seeks to attenuate as much of the electromagnetic fields as possible. An optional iron layer shunts and absorbs any low to high frequency fields that manage to penetrate through the copper layer. As the iron layer will only come in cotact with relatively small amount of high frequency fields, the ohmic losses will be minimal. If static to low frequency magnetic radiation is not an issue, then the iron layer is not required. An air gap or thermal insulator is placed between the copper and iron layer in order to prevent heat from

diffusing onto the iron and downrating its magnetic properties. The layering also introduces multiple boundaries, subsequently raising reflection loss.

Shielding is also employed at the bottom of the transformer in order to mitigate the amount of fields from penetrating through to the aluminum heat sink. Such a penetration is undesirable as there may be other circuit components utilizing the same heat-sink that may start coupling with the transformer through the heat-sink. However, from a thermal management perspective, it would be best if the heat sink also served as a shield because that would reduce the number of material interfaces, subsequently reducing thermal resistances.

A material that acts as an electrical insulator and a thermal conductor is placed at the bottom of the transformer, between the windings and the copper shield. The material keeps the windings on the transformer electrically insulated from the shield while simultaneously allowing heat to be extracted to the heat sink through the shield. The same material is also found on the other side of the transformer, between the PCB and the copper shield in Fig. 5.26a. Once again, the material extracts heat from the copper traces on the PCB to the copper shield. As copper has an excellent thermal conductivity, it carries the heat to the aluminum heat sink.

An electro-thermal insulating layer is placed between the transformer and the PCB in Fig. 5.26a. This material keeps the PCB electrically insulated from the transformer, except for the necessary terminal connections, and also impedes the heat generated in the transformer from diffusing onto the PCB.

For the structure in Fig. 5.26b, thermal conductor is only required at the bottom of the transformer, between the windings and the shield, so that heat only flows in one direction.

An electro-thermal continuity is maintained between the top and the bottom half of the shields of the first structure through multiple through-hole vias on the PCB, which are not shown in the figure.

While the shield design was undertaken from a magnetic perspective, the structure is also fully capable of attenuating electric fields. One major addition required for electric field shielding is the grounding of the copper shield layer. The grounding of the copper layer does not affect the shield's capability in attenuating magnetic fields [22, 23].

Chapter 6
Directly Depositing Windings onto the Core
6.1 Existing Winding Technologies

Over the years, three major winding technologies have been widely utilized in creation of the disk-type planar magnetic structures. Some efforts have been made to adapt these technologies for the tube-type structures [65], but their practicality is questionable. These technologies are:

1. **Stamped Copper Foil** [4]
    - low cost
    - windings of any copper thickness
    - high window area utilization
    - insulation required separately
    - difficult to achieve low and consistent leakage inductance sample to sample
    - folds in windings increase thermal resistance
2. **PCB** [4, 66, 67]
    - suitable for mass production
    - low current carrying capability
    - consistent performance sample to sample
    - low window utilization factor
    - requires vertical connectors to achieve electrical continuity
3. **Flexible Printed Circuits** [4, 68]
    - etching process utilized
    - insulation provided by the substrate (i.e. Kapton)
    - interconnections required to establish electrical continuity
    - improved window utilization factor compared to PCB

- folds in windings increase thermal resistance

Stamped copper foil is ideal for applications that require high current carrying capability with a high window utilization factor at a low cost. This type of winding is shown in Fig. 1.4(b). Downside of this winding scheme is that insulation has to be provided separately. Achieving consistent values of parasitic from sample-to-sample is also difficult as the structures are hand-wound and the windings tend to shift around. Thus, this is an inadequate solution for designs that rely heavily on leakage values.

The multi-layer PCB winding technology is most popular for the disk-type designs as the windings constitute part of the circuit board with holes for core insertion [4, 66, 67]. When applied to the tube-type design, vertical connectors are required whose attachment unnecessarily increases AC resistance [4] and mandates additional labor. So the possibility of acquiring efficient, low cost, mass produced tube-type PCB structure is not very good. Refer to US patent 6,952,153 B2 issued to Raytheon for an example of this type of winding scheme.

Flexible printed circuits are another popular winding solution for the tube-type structures that addresses some issues raised by stamped copper foil, and introduces some of its own. The windings are etched through standard 2-D planar processes and are then folded around the core. Due to utilization of the etching process, windings are accurately formed and leakage parameters are consistent from sample to sample. The insulation is automatically provided by the substrate used during the etching process. This technology also increases window utilization factor when compared against PCB, as layer stacking is easily achieved. However, interwinding connections are still required to establish electrical continuity. An example of flex circuit for the tube-type application is shown in Fig. 6.1 [65]. Similar to the stamped copper foil, folding of the conductors in a flex circuit create increased thermal resistances that results in local hot spots. Unlike stamped copper foils, the flex circuits are incapable of handling large amount of current due to the limitation of processes in creating relatively thick windings.

Each of the winding technologies have their own advantages and disadvantages so trade-offs are expected to be made during design process. However, what if an alternate solution was explored that would combine some of the best features of these three major winding technologies?

Thus, feasibility and practicality of *directly* etching windings onto a core is explored in this chapter. Similar work have been undertaken by others, through

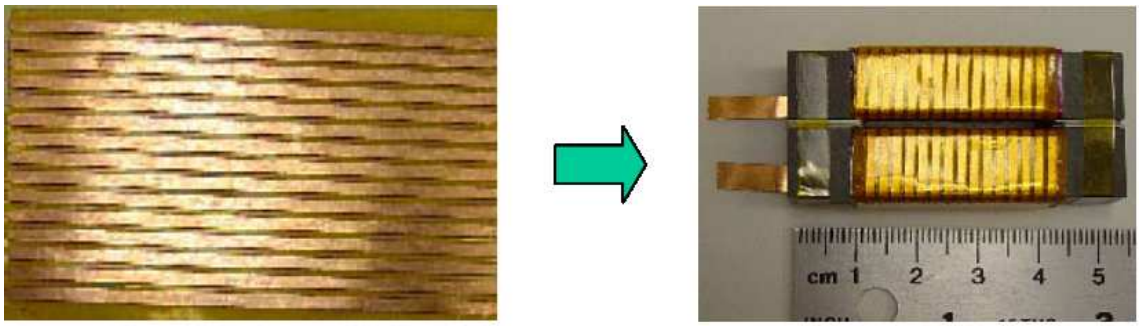

Figure 6.1: Creation of tube-type structure using flex circuit technology.

thick film, thin film or electroplating, but the focus has been primarily in 2-D etching for relatively low power applications [69, 3, 70, 71, 72, 7].

6.2 Direct Etching of Windings

The 3D etching process is undertaken after a conductive layer of adequate thickness has been applied to the areas of the core where the windings will be situated. In order to establish electrical isolation between core and winding, a thin layer of insulating material is applied to the core. The conductive layer can be formed in many different ways, such as electroplating or with adhesive backed conductive foil wrapped around the core legs.

There are multiple potential advantages apparent in directly etching the windings onto a core. The 3D etching process ensures that no inter-connections are required. The terminal connections to the rest of the circuit are the only necessary connection. The etching process assures that a consistent geometry is developed from one sample to another leading to tightly controlled parasitic values. Higher window utilization factor is achieved through layering. If electroplating is used to create the conductive layer, no folding of the conductor is necessary, which minimizes thermal resistances. The entire fabrication process is suitable for automation, obviating manual labor, as much of the processing steps can be undertaken in an assembly-line like fashion.

However, the solution is not without its share of disadvantages. The etching process is faced with difficulties as much of the existing lab equipment are tailored for 2-D planar processes. Due to the inadequacy of present 2-D processes and equipment to handle 3-D geometries, samples are created with a lower yield. If the electroplating route is taken for creation of conductive layer, the thickness of

the layer is limited by present technology. Long process time are also encountered throughout the whole process.

Putting all the obstacles aside, should this vision be fully realized, an end-product similar to Fig. 6.2 can be the result.

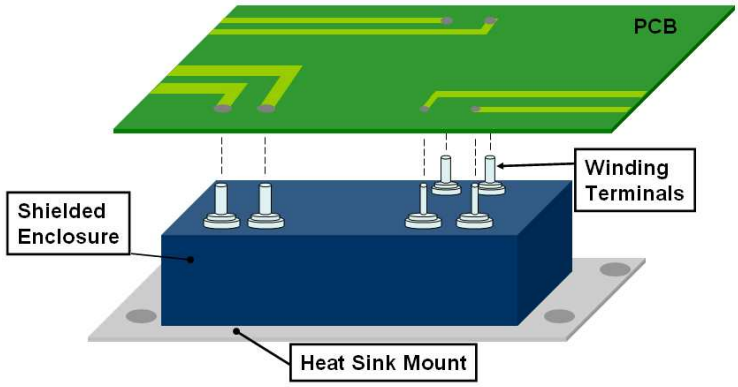

Figure 6.2: Enclosed magnetic structure: a potential end-product of this work.

The device would have the following advantages:

1. Highly similar parasitic values, sample-to-sample
2. High power density
3. High efficiency
4. Low profile
5. Better thermal management
6. Stand-alone structure that can be tested and measured separately

6.3 Direct Etching Overview

The steps in fabricating a tube-type planar magnetics structure through direct etching of windings on the core are outlined in this chapter. Major issues are highlighted and where applicable, a solution, if not implemented, is proposed.

The general procedure for creating the windings on the core is:

1. Apply solder mask
2. Sputter titanium and copper

3. Electroplate copper
4. Apply photo mask to establish winding patterns
5. Etch the copper
6. Etch the titanium

6.4 Core Selection

Plethora of literature exist that support the use of soft ferrite for high frequency power application. The core selection process was thus begun directly at Ferroxcube's website where they list wide range of ferrite materials for such an application. The two major requirements for a core material in this work are:

1. High curie temperature.
2. Wide frequency bandwidth (1-2 MHz for this work)

Thus, 3F45 was the ideal choice, as it offered both the widest bandwidth and highest curie temperature. The core is custom made by Elna Magnetics and is shown in Fig. 6.3.

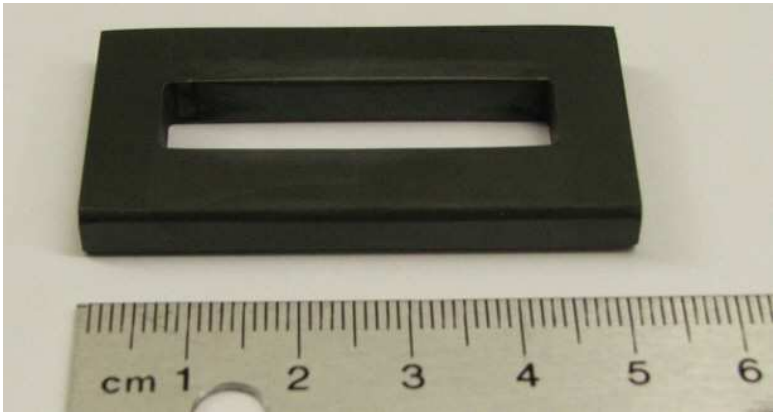

Figure 6.3: 3F45 ferrite core used in the design.

6.5 Applying Solder Mask

Before the solder mask is applied, the ferrite must be cleaned well of any particles and organic residues such as oil from fingertips. The cleaning is achieved

through a chemical bath process involving acetone, ethyl or propenyl alcohol, and de-ionized water. The ferrite is first dipped into acetone to remove particles and organics. Before the acetone evaporates, the ferrite is dipped into propenyl to prevent organics from drying on the ferrite. The ferrite is then immediately rinsed with de-ionized water to remove all substance and solutions. De-ionized water must be used as ionized molecules attract floating particles from the air. This process is repeated twice.

The ferrite is wet from water at this point so it is dried with nitrogen from a compressed tank. It is not a good idea to dry the material with machine-compressed gas, as the compressed air will contain oil/grease residue of the machine. It should be noted that all handling of the material, during any point in the process, must be done with gloves in order to keep the sample clean and to provide self-protection from acidic and harmful chemicals.

The liquid photoimageable solder mask system is based on proper mixing of two chemicals: Enthone DSR-3241BQ and DSR-3241A-GQ. The former is a very thick white chemical, while the latter is a more fluid green chemical. The solder mask is created by mixing one part DSR-3241BQ and four part DSR-3241A-GQ (1 : 4). The two chemicals are hand stirred, although machine mixing is ideal. Once a nice smooth texture is acquired and the individual chemicals are indistinguishable, the solder mask is ready to be applied. The solder mask is photo sensitive. However, because it needs to be applied evenly on the entire surface area of the core, protection from UV light is not necessary.

The solder mask is applied on one side of the core first, as smoothly as possible. A spin coater may be used in order to improve homogeneity and smoothness. The problem with using spin coaters found in most standard packaging lab is that they are designed for flat plate type structures such as ceramic substrates. A vacuum suction at the center of the spinner is used to keep the substrate from flying off the spinner as it is spun up to 1800 RPM. However, the center of mass for a core is at the center of the core window. Thus the vacuum has nothing to hold on to of the material. For this reason, an adapter of a sort is created for the spin coater.

The adapter comprises of a soft aluminum plate with drilled holes. The process of drilling causes the soft metal to wrap itself around the drill bit as it goes through the plate. Bits of the metal stay attached to the plate, as shown in Fig. 6.4. These circular metal 'columns' that encircle the holes are used as barriers. The holes are strategically drilled such that the columns isolate and keep the core from moving around. In the case in Fig. 6.4, the holes keep the outer diagonal corners of the

ferrite in place. The spin coater's vacuum holds the plate in place, which in turn holds the core.

Figure 6.4: Adapter that enables ferrite core to be used in the spin coater.

Once the solder mask is applied smoothly to one side, the core is placed on a heater at 70°C for 20 minutes. The side that the solder mask was not applied to is placed on the heater. The core is left to cool back down to room temperature on its own. This process hardens the solder mask. The solder mask is applied to rest of the remaining surface area and placed on the heater again. It is a good idea to elevate the core from the heater with something like metal washers placed at the four corners in order to avoid direct contact between the heater and the previously applied solder mask.

Figure 6.5: The core after applying solder mask.

The sample shown in Fig. 6.5 is ready to be cured. Curing ensures that the

solder mask will remain unaffected by temperature change or chemical exposure up to a certain limit. The curing is performed in an oven with a heating profile depicted by Fig. 6.6. The parameters R_i, T_i, and H_i are ramping rate, plateau temperature, and duration of the plateau respectively. The heating profile described by these three parameters are entered directly onto the oven's setting.

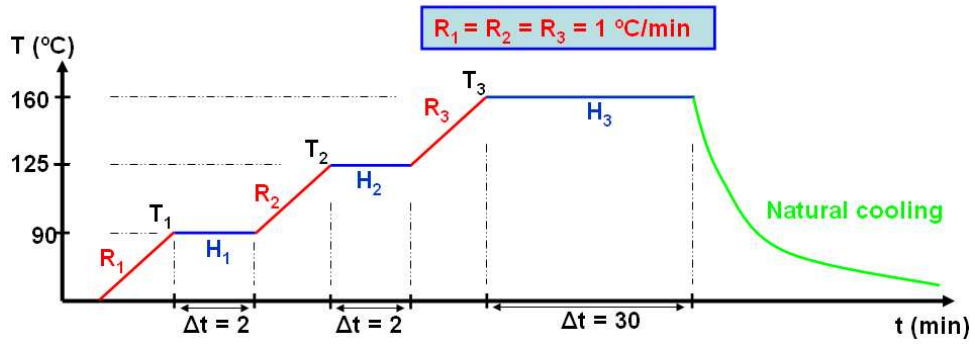

Figure 6.6: The heating profile for the curing of solder mask.

6.6 Vapor Deposition

Before copper is electroplated onto a material, there needs to be a seed layer of copper on the material. The seed layer acts as the cathode in attracting the copper cations. Physical vapor deposition (PVD) or physical sputtering is used to establish the seed layer by depositing a thin layer of metal onto the core. The seed layer is typically in the order of nanometers.

Edwards Auto 306 Vacuum Coater with diffusion pumping system is used for the sputtering. For this machine, titanium sputtered for half an hour results in 50-60 nm thick metalization, while copper sputtered for half an hour typically yields 500-600 nm thickness. Titanium is sputtered first as the adhesion or buffer layer because it has a stronger bonding capability than copper when sputtered onto other materials [73, 74, 75, 76]. Titanium is sputtered for 30 minutes on each of the two planar sides of the core. Due to the core's low profile structure, the insides and outsides of the core are automatically metalized during the sputtering of the top and the bottom.

Once titanium is metalized on the entire surface area of the core, copper is sputtered in a similar fashion. Refer to Appendix A for details on the operation of the sputtering machine. Fig. 6.7 shows the core after sputtering.

Figure 6.7: The core after a) sputtering titanium, and b) sputtering copper.

6.7 Electroplating

Electroplating increases the metalization layer that was initiated by the sputtered seed layer. A conductive frame holds the sample for electroplating. An autocad drawing, shown in Fig. 6.8 of the frame is created. Using *Quickcircuit 5000*, a milling machine used for PCB circuit creation, the frame is cut out of an FR4 board. FR4 boards are comprised of copper layer bonded to an insulating substrate and are typically used in creation of PCB circuits. The insulating material of these boards are made with a resin epoxy composite with a woven fiberglass mat. The copper layer establishes an electrical contact between the core (the substrate) to the electroplating machine. The insulating layer of FR4 provides structural support to the frame. A solid copper may be used, but handling and shaping of solid copper at the desired rigidity level is difficult. Two long strips of copper foil are soldered onto the top portion of each of the two FR4 cutout's copper layer. The bottom portions of the two cutouts are held together by piece of Kapton tape. The core is then held by the frame as shown in Fig. 6.9.

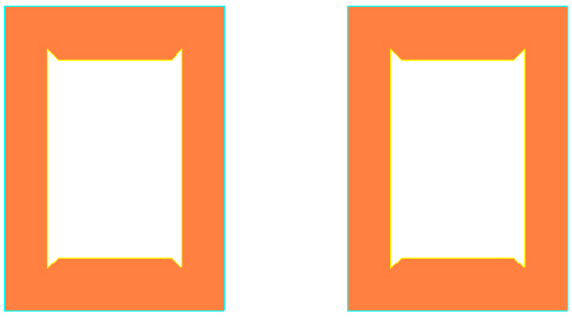

Figure 6.8: CAD drawing of a frame that will house the core for electroplating.

The electroplating machine, Heraeus PGG 10, available in the CPES packaging

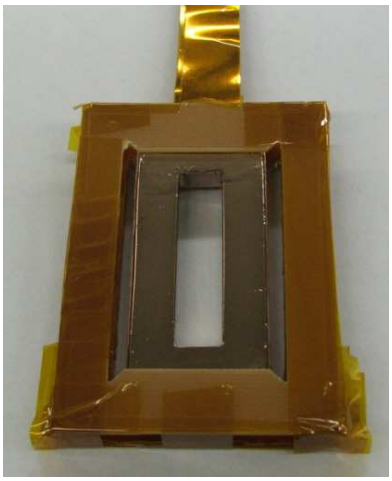

Figure 6.9: The frame housing the core for electroplating.

lab is designed for 2-D double sided electroplating. The core at hand, however, will have windings all around the two core legs, not just on two surfaces. Thus, a little modification is necessary in order to electroplate on all four sides of the two core legs. A frame made of bent aluminum strips is created in order to hang copper anodes from the other two sides that the machine does not support. Conductive foil is used to electrically connect the aluminum strip frame to the machine so that the anodes hanging off the frame are part of the electroplating circuit. The setup used for the electroplating is shown in Fig. 6.10.

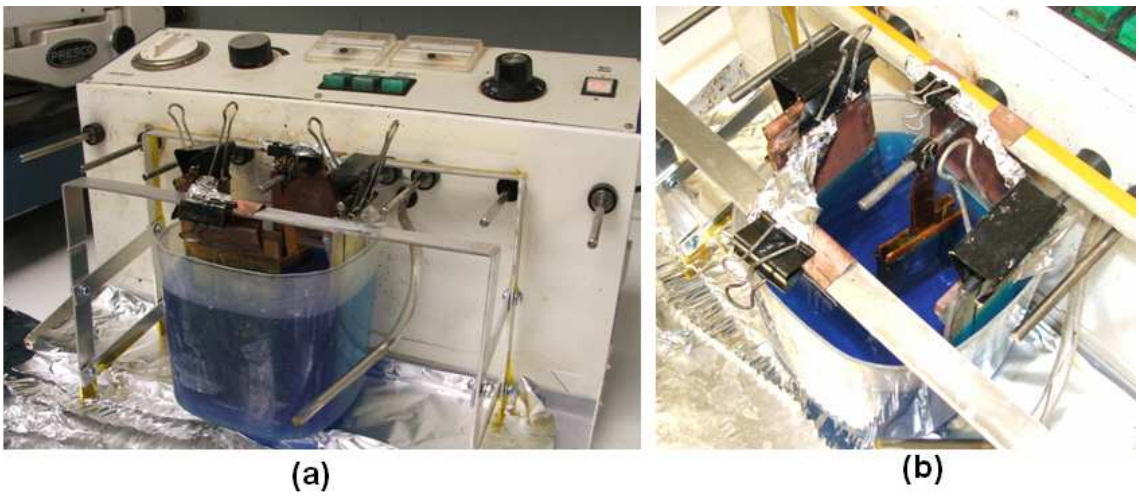

Figure 6.10: Electroplating setup with a) machine and aluminum strip frame holding two additional copper anodes, and b) sputtered core as the cathode in the center surrounded by four copper anodes.

The deposition rate is directly proportional to plating current density. The higher deposition rate yields faster deposition but with greater stresses. And the lower deposition rate results in harder deposit but lengthy process time. Thus, an optimal plating current density must be found that minimizes both time and stress. So, a plating current density of 20 A/ft^2 is selected to provide a deposit rate of 1 mil/hr. For the core under consideration, with the dimension shown in Fig. 6.11, the actual current value is calculated as:

$$\begin{aligned} A_{Total} &= 5.48 \text{ in}^2 \\ &= 0.0381 \text{ ft}^2 \end{aligned}$$

$$\begin{aligned} I &= 20 \text{ A/ft}^2 \cdot 0.0381 \text{ ft}^2 \\ &= 0.76 \text{ A} \end{aligned}$$

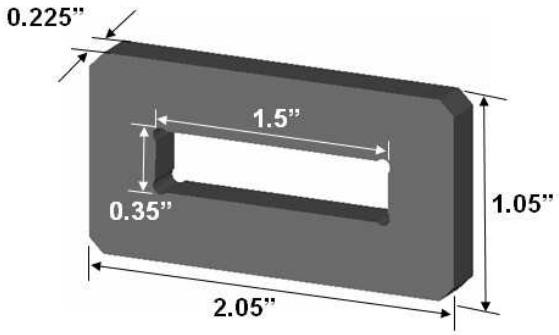

Figure 6.11: The dimension of the core used in creating a tube-type transformer.

So in order to electroplate 1 mil thick copper, the process should run for an hour. In order to demonstrate the concept, copper is electroplated onto the core for four hours in order to yield a 4 mils thick layer.

6.8 Applying Photo Mask

Before the windings can be etched onto the core, a mask must be made so that it can protect the parts of the copper layer that will form the windings. A photoimageable etch resist (blue) is utilized for creation of the mask. The etch resist protects the copper layer from the copper etchant. The areas that are covered

eventually form the windings. The etch resist is Photrak ETP240/1694. This is a negative etch resist, which means that etch resist not exposed to UV light dissolves in the photo developing solution.

The ends of the core are protected from the etch resist by wrapping Kapton tapes around them such that only the core leg regions where the windings will be is exposed. This is to minimize the amount of area that needs to be masked off during the UV exposure of the etch resist. The etch resist is applied exactly like the solder mask on the core legs. The etch resist chemical is less viscous compared to the solder mask, so care must be taken in applying a smooth, even layer. The spin coater may be used once again to achieve greater homogeneity with the adapter shown in Fig. 6.4. The core is placed on a heater to harden the etch resist for 35 min. The procedure is then repeated on rest of the remaining surface area of the core legs. Care must be taken not to expose the sample to UV light, otherwise the etch resist will develop incorrectly.

The photo masks shown in Fig. 6.12 is printed onto an adhesive-backed transparency. The masks are then cut out around the outer perimeter from the transparency sheet, and wrapped as tightly as possible around each of the core legs. The core is then placed in a UV chamber, and exposed to UV lights for 10 minutes on each of the sides. The insides cannot be exposed at a direct line-of-sight to the UV lamps because the core structure is a single piece with no air gaps and so cannot be separated. Thus, they are exposed indirectly when top, bottom and outsides are exposed.

Figure 6.12: Photo mask used in UV exposure of the etch resist.

After the UV exposure, the photo masks are peeled off and the core is dunked into a photo developing solution. The photo developer is created by mixing one part D-4000 Liquid Developer Concentrate, and twenty part water (1 : 20). Using a soft brush, the etch resist materials are brushed off from the regions that were not

exposed to the UV light (the parts that were covered by the photo mask). Over exposure to photo developer is not a good idea as it may strip off areas of etch resist that are protecting the winding geometry. The resulting sample is shown in Fig. 6.13. The etch resist do not bond well to sharp corners, so nail polish is used to cover any exposed areas that are part of the winding geometry.

Figure 6.13: The core after applying the etch resist.

6.9 Etching

Copper is etched using an etching machine containing heated ferric chloride solution. Etching is done in five minute intervals to avoid overexposure to the highly corrosive acid. Overexposure can lead to undesired etching and undercutting of the traces. The sample is hung from an insulated wire to ensure that the etchant does not pool for too long at any one spot on the sample. Once all the exposed copper have been removed, the sample is rinsed using DI water to remove any remaining traces of the ferric chloride solution. At this point, titanium is exposed on areas not covered by the etch resist. Etching of titanium is done by mixing one part Titanium Etchant TFT solution with twenty part water ($1:20$). The sample is dunked into a beaker containing the titanium etch solution. A soft brush is used to carefully rub off the exposed titanium. The light brushing speeds up the process of etching in order to avoid overexposure to the highly toxic titanium etch solution. Once all exposed titanium is removed, the green solder mask should be visible. The sample is rinsed off with DI water to wash away the etch solution.

6.10 Sample Preparation for Measurement

Removal of the etch resist in order to reveal the winding traces is achieved by the use of acetone. It is not a good idea to dip the whole sample into acetone

as the solder mask will start warping and dissolving upon lengthy exposure to the acetone. So, instead the etch resist is rubbed off with care using a cotton-tipped swab soaked in acetone. The sample is rinsed with DI water once all the remaining etch resist have been cleared off. The process of etching windings onto an insulated core is complete and the resulting core with the windings is shown in Fig. 6.14.

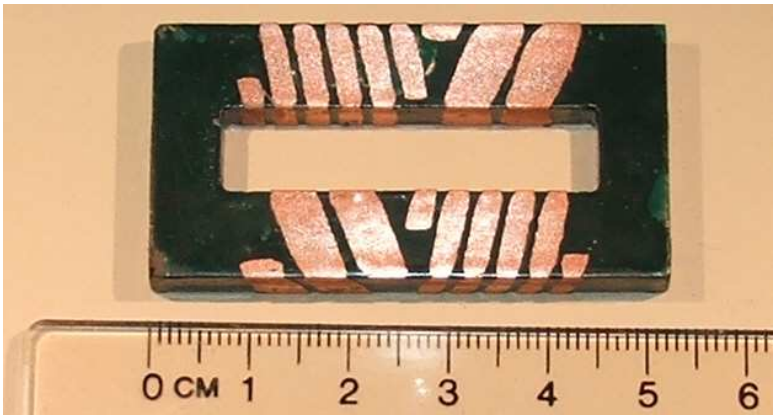

Figure 6.14: The core with windings directly etched onto it.

External connectors such as pins or copper foil are soldered onto the winding terminals for measurement purpose.

Chapter 7
Conclusion
7.1 Summary

Accurate electromagnetic modeling methodologies applied to planar transformers are presented in this work. The focus is on transformers with planar windings wrapped around the core legs of a low profile. The modeling is undertaken based on an accurate derivation of the electromagnetic field distribution in and around the transformer structure. Both finite element modeling and analytical methods are employed in deriving the field distribution.

Chapter 2: Frequency-Dependent Modeling

Background information on issues and phenomena that are apparent in high-frequency transformers are briefly outlined. Understanding of these phenomena are necessary in order to gain insight into the results acquired through the various modeling tools.

Analytical and numerical means in calculating the losses in the windings due to the eddy current effects are presented. The analytical method is restricted to planar windings due to the various assumptions that were made in reducing the order of complexity. The losses in a non-magnetic shield can also be calculated using the derived analytical expressions.

Analytical expressions are given for the core loss calculations. Because FE software do not have the ability to model the non-linear behavior of the core in most eddy current solvers, the analytical expressions are vital in predicting the total losses in power inductors and transformers. The losses occuring in the core is primarily due to hysteresis and eddy current effects. The classical Steinmetz equation is not valid for calculating hysteresis core loss in most DC-DC converter applications, as the core experiences non-sinusoidal excitations. Thus, a set of modified hysteresis core loss equations are presented that take into account the effect of non-sinusoidal waveforms. The losses due to the eddy currents are calculated by a simple equation under the assumption that the flux density is uniformly distributed throughout the cross-section of the core.

The sensitivity of the magnetic material properties to machining processes,

the final core structure and the frequency of excitation is described and the means to determine the proper relative permeability of a core is provided.

Appropriate thermal modeling is critial in identifying maximum temperature gradients in a device such that appropriate measures can be taken in order to ensure that the temperature does not exceed material limitations. A simple 1-D thermal modeling is described to predict the maximum temperature of a transformer.

The various losses in the core and windings raise the device temperature, reduce efficiency and power density. Thus, a methodology to optimize the performance of planar passive magnetic devices is described. The methodology employs the concept of complex permeability in order to obtain the expression for core loss. The expression of the winding loss relies on DC resistance of the conductor for some average value of current density. In neither the core or the winding loss expressions are the effects of eddy currents taken into account. However, if the equivalent thickness of the windings and the value of the average current density is selected appropriately, the eddy current effects in the windings can be included to a degree.

Chapter 3: Modeling of Electrodynamics

Due to the shapes of the windings, the high frequency magnetic fields present, and eddy current effects taking place, a time-varying electric field exists along the windings of a transformer. The time-varying electric field induce what is known as displacement current that exhibit a high frequency behavior equivalent to charge displacement taking place in capacitors. Thus, transformer winding impedances are often modeled with the inclusion of distributed capacitances similar to transmission lines. An analytical methodology is provided for calculating the winding capacitances. Schwarz-Christoffel conformal mapping is used in the derivation of capacitance between adjacent winding turns. Although the method has been widely popular in extracting capacitance between adjacent thin-film conductive strips deposited on a high dielectric substrate, it does not directly apply when modeling capacitances along a transformer winding. Thus, the approach is modified slightly in this work. The capacitance that exists between the planar windings and the core is derived based on the classical parallel plate capacitor method. Results from the analytical approach are compared with FEM and experimental measurements and are found to be in good accord.

Chapter 4: Leakage Reactance and Cross-Coupling

Significant amount of magnetic coupling take place among the windings, and between the windings and adjacent circuit devices. The former is the primary mode through which a transformer functions. The latter is due to leakage reactance. The magnetic flux contributing to the leakage reactances are one of the prime factors in performance degradation due to losses, poor load regulation and cross-regulation of multiple outputs. Both numerical and analytical methodologies are explored in modeling the reactive nature of a transformer. Method of images coupled with approximations regarding the 3-D distribution of the magnetic fields are applied in deriving the leakage reactance. The result through this approach is found to be acceptably accurate when compared with FEM and experimental measurements.

Extended cantilever model is employed in predicting the cross-coupling of the windings. The model is extracted through two different numerical approaches using a FEM software. The first method employs similar procedure as the experimental method outlined in the paper by Erickson but modified slightly for numerical extraction. The second method utilizes the self and mutual inductance matrix to derive the parameters. Both methods are found to be accurate when compared against experimental measurements. However, when the window utilization factor is significantly higher, the first method yields higher accuracy.

Chapter 5: Shield Design

One of the biggest drawbacks of structures with the windings exposed to the environment is the significant increase in electromagnetic radiation. Large leakage flux can couple with the adjacent devices leading to increased losses, overheating, and can introduce noise in the circuit. Thus, electromagnetic shielding becomes a necessity in order to mitigate the level of coupling. A simple near-field electromagnetic shield design method is presented. The design is conducted from both magnetoquasistatic (MQS) and classical plane wave perspective. Several potential shield materials are studied and compared in terms of their shielding effectiveness and the additional losses that they might respectively bring about. FEM is used to study the losses encountered in the windings and shield for the different shield materials. A potential shield structure is proposed based on the study.

Chapter 6: Directly Depositing Windings onto the Core

The use of the planar tube-type magnetics pose different set of challenges in terms of winding scheme because the mature 2-D planar manufacturing process

enjoyed by the disk-type structures is not directly applicable to the 3-D tube-types. The current state-of-the-art winding schemes are described and their drawbacks are discussed. A new winding scheme is proposed in which the copper windings are directly deposited onto the core. A procedure for fabricating such a device is outlined using standard packaging lab equipment. Benefits and drawbacks of this winding scheme is desribed as well.

7.2 Future Work

The prime motivation towards using analytical tools and algorithms is to cut down on time and modeling complexity so that a company does not have to spend valuable resources in training a green employee in the use of complex FEM software. Further, analytical tools circumvent the need for expensive computing resources necessary in order to reduce lengthy simulation time required by FEM software. So in light of these considerations, the next logical step in continuation of this work would be to put together the various analytical modules into one complete package with a friendly graphical user interface (GUI) to control them. At the moment, the analytical algorithms are able to calculate losses, parasitics, etc. of the magnetics in a relatively short amount of time, but they are still too complex to use in their native mathematical forms. Thus, an interface, similar to the one shown in Fig. 7.1, is required to faciliate data entry and viewing of the results in a simple and easy manner.

The software shown in the figure was created for a thermal project that required prediction of the potential temperature distribution on the stator of a modular motor. Similarly, all the analytical and FEM methodologies presented in this work can be combined together in a modular fashion using Matlab and Comsol Multiphysics (a FEM software) to create a complete analytical and numerical tools package.

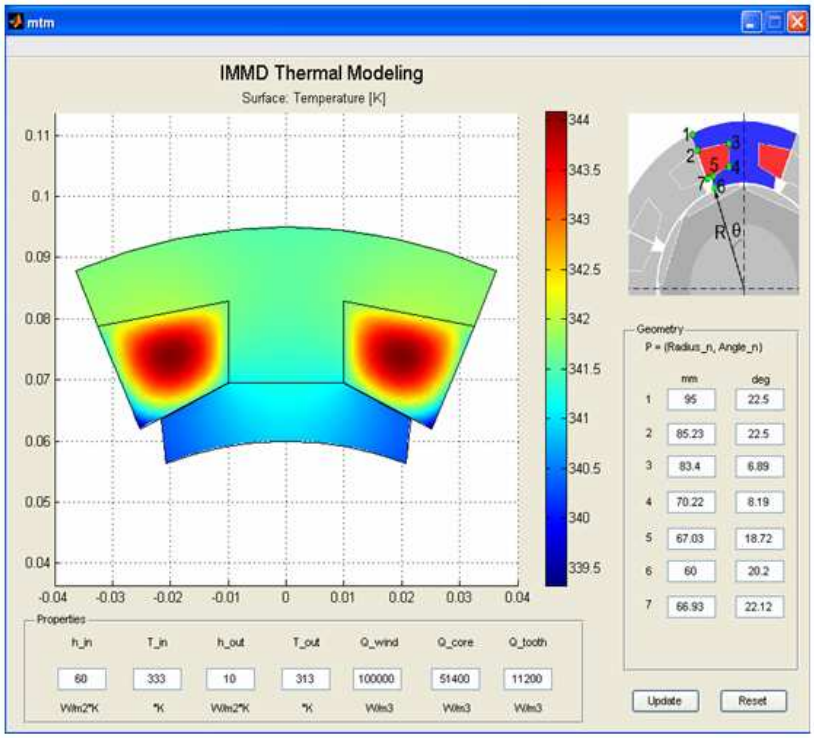

Figure 7.1: GUI Interface for analytical and numerical modules used in calculating temperature distribution of a stator.

Appendix A

Using the Sputtering Machine

Edwards Auto 306 Vacuum Coater with diffusion pumping system is shown in Fig. A.1. The sample is placed in the vacuum chamber. Chamber controls are used to control the conditions in the chamber. RF power controls are used to control the input power going into the sputtering machine through the rf power ports. The gas pressure is also controlled through these control panels.

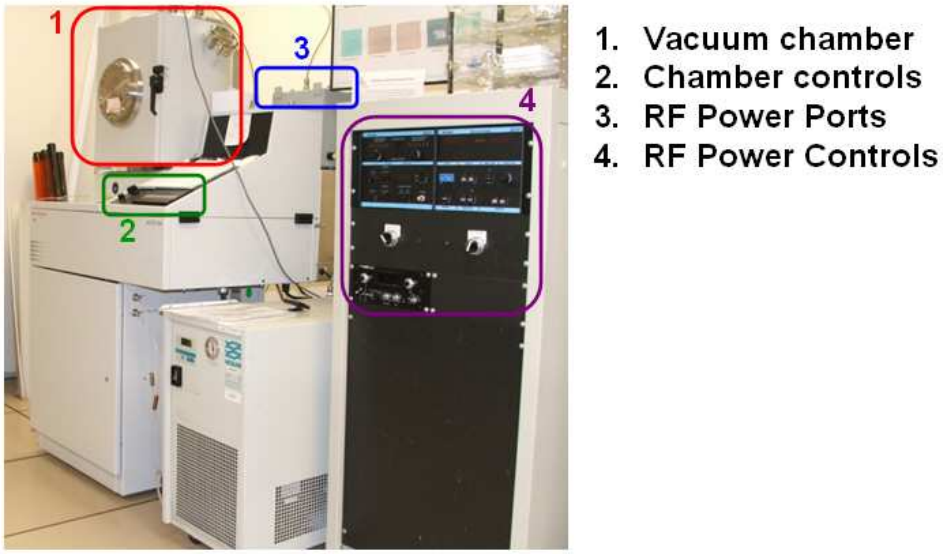

Figure A.1: Machine used in physical vapor deposition through sputtering.

The primary goal of this appendix is to outline the steps taken in sputtering titanium, Ti, and copper, Cu, onto the ferrite core using this particular PVD machine.

A.1 Basic Theory of Sputtering

Sputtering is a type of physical vapor deposition (PVD) technique in which high energy ions are used to dislodge atoms from a source material such as a piece of copper or titanium, and through a low pressure region, sputter the dislodged atoms onto a substrate such as the core.

RF power is used to excite argon atoms causing them to lose their valence

electrons and become high energy ions (or plasma) that bounce around at a very high velocity. The ions act similar to a cue ball in billiard to strike group of atoms on the piece of copper or titanium and subsequently dislodge them. The ejected atoms travel through a low pressure region and condense on the substrate. As these atoms are neutrally charged, they are not affected by the electromagnetic force due to the argon ions. Vacuum is pulled in the chamber in order to reduce amount of impurities.

A.2 Sputtering Procedure

The basic outline of the sputtering procedure is: 1) sputter titanium on both sides of the core first, then 2) sputter copper on both sides of the core.

1. **Chamber on standby**. The chamber should be empty and the chamber control panel should indicate "FINE PUMPING." Fine pumping is to create a vacuum in the chamber. This should be the natural state of the machine when not in use.

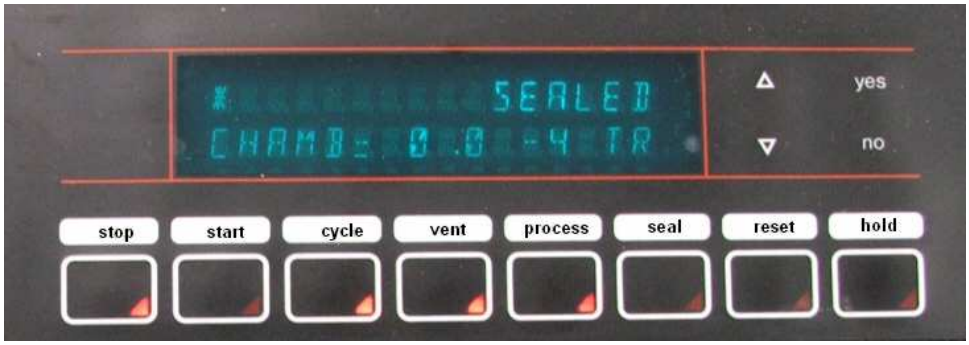

Figure A.2: Control panel of the sputtering chamber.

2. **Vent & Place**.

   (a) Open the valve all the way on the nitrogen, N_2, tank.

   (b) Push the *Vent* button on the chamber control panel depicted in Fig. A.2.

   (c) The chamber's control display should read "CHAMBER VENT."

   (d) When the pressure has reached 7.6×10^2 Torr on the display, try opening the chamber door. If the chamber door does not open, wait one more minute, and try again. Keep waiting and trying. When the pressure is high enough in the chamber, the door will open.

(e) Push the *Seal* button on the chamber control panel. This stops the flow of N_2.

(f) Close the valve on the N_2 tank tightly.

(g) Place the core on the hanging sample tray.

(h) Make sure that both titanium and copper targets are installed.

(i) Rotate the tray so that the sample is right below the titanium target.

(j) Close the chamber door.

3. **Pump**. Push the *Cycle* button on the chamber control panel. The chamber display will indicate that it is roughly pumping at first. However, after a minute, "FINE PUMPING" should appear on the display. Wait for few hours.

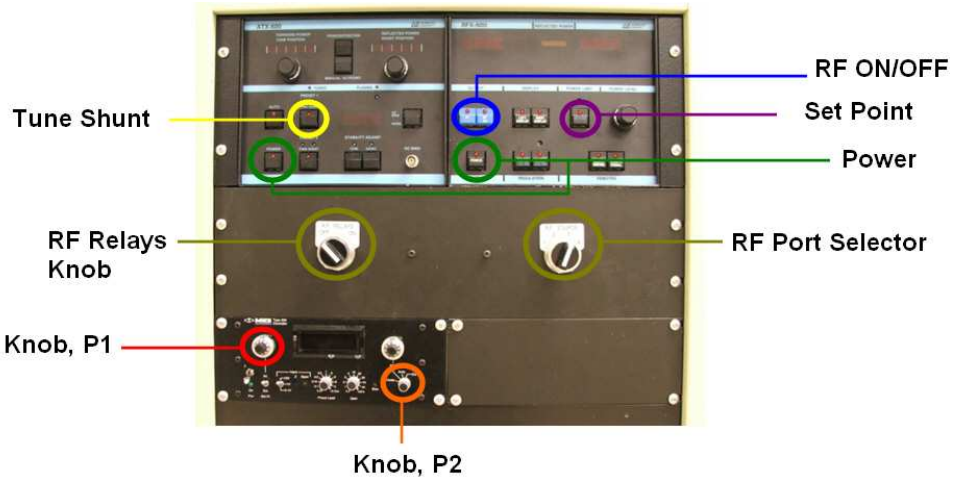

Figure A.3: Control Panels for the RF Power.

4. **Purge**.

(a) Wait until a pressure of 2×10^{-6} Torr is shown on the control panel display.

(b) Open the valve on the Argon gas tank.

(c) Push *Process*, and then *Hold*. The buttons are bit hard, so exert adequate force.

(d) The light on the *Hold* button should be blinking. The display should indicate "PLASMA PROCESS."

(e) On the bottom left of the RF control panel, turn the dial knob, marked 'P1' in Fig. A.3, to a pressure of 25 Torr.

(f) Turn the other knob, marked 'P2', from *Close* to *Auto*.

(g) Wait 30 minutes, while gas is cycled and tubes and chamber is purged of impurities.

5. **Pump**.

(a) Turn the knob 'P2' from *Auto* to *Close*.

(b) Push the *Hold* button on the chamber control panel. The light below it should stop blinking.

(c) The chamber should eventually display "FINE PUMPING" again.

(d) Wait until the pressure is back to 2×10^{-6} Torr again.

6. **Prepare to Sputter Ti**.

(a) Connect the cable leading to the titanium target to Port 3, or whatever RF port is currently working (Port 1-4).

(b) Make sure that the core is right below the titanium target.

(c) Push *Process*, and then *Hold*. The light underneath the Hold button starts blinking. The chamber display should indicate "PLASMA PROCESS."

(d) Turn the knob 'P2' from *Close* to *Auto*.

(e) Push the two *Power* buttons on the top two RF control panels, indicated in Fig. A.3.

(f) Turn the *RF Relays* knob to *ON*.

(g) Ensure that *RF Source* knob is selected to the port that is connected to the titanium (Port 3).

(h) Push the *Set Point* button on the top right RF control panel shown in Fig. A.3. Observe that the Set Point value should be around 100.

(i) Push and hold the *Tune Shunt* button couple of times.

7. **Sputter Ti**.

(a) Push the *RF ON* button in Fig. A.3.

(b) Turn the knob 'P1' from 25 to 10 Torr.

(c) Blue light should be apparent through the sputtering chamber window.

(d) Sputter for 30 minutes.

8. **End Sputtering**.

   (a) Push the *RF OFF* button indicated in Fig. A.3.

   (b) Turn the *RF Relays* knob to *OFF*.

   (c) Turn the knob 'P1' from 10 to 25 Torr.

9. **Stop Sputtering**.

   (a) Turn the knob 'P2' from *Auto* to *Close*.

   (b) Push the *Hold* button. The light below it should stop blinking.

   (c) Close the valve tightly on the Argon tank.

   (d) Turn off the two *Power* button Fig. A.3.

10. **Repeat Steps 2-8**. Repeat the steps again in order to sputter titanium on the other side of the core. However, do not repeat Step 9 the second time around, but skip ahead to Step 11.

11. **Cool down**. Allow 5 minutes for the chamber and the substrate to cool down.

12. **Prepare to Sputter Cu**.

    (a) Rotate the tray so that the core is right below the Copper target.

    (b) Connect the cable attached to the copper target to RF Port 3.

    (c) Turn the *RF Relays* knob to *ON*.

    (d) Push the *Set Point* button. Set point value of around 100 should be observed on the RF display panel.

    (e) Push and hold the Tune Shunt button couple of times.

13. **Sputter Cu**.

    (a) Push the *RF ON* button.

    (b) Turn the pressure knob 'P1' from 25 to 10 Torr.

    (c) Blue light should be observed through the window inside the sputtering chamber.

(d) Sputter for 30 minutes.

14. **End Sputtering**.

    (a) Push the *RF OFF* button.

    (b) Turn the *RF Relays* knob to *OFF*.

    (c) Turn pressure knob 'P1' from 10 to 25 Torr.

15. **Stop Sputtering**.

    (a) Turn the knob 'P2' from *Auto* to *Close*.

    (b) Push the *Hold* button. The light below it should stop blinking.

    (c) Close the valve on the Argon gas tank.

    (d) Turn off both *Power* buttons on the RF control panel.

16. **Repeat Steps 2-9**. Repeat steps 2-9 one more time in order to sputter copper on the other side of the core. Make the necessary changes to the steps in order to sputter copper instead of titanium.

17. **Repeat Step 2**. Repeat step 2 in order to take the finished sample out of the chamber.

18. **Final State**. Close the chamber door, and push *Cycle* button in order to keep the chamber in "FINE PUMPING" standby.

Appendix B

Analytical Matlab Modules

The analytical leakage inductance is calculated through the Matlab modules described in Fig. B.1. The matlab codes used in creating the modules is listed in this appendix.

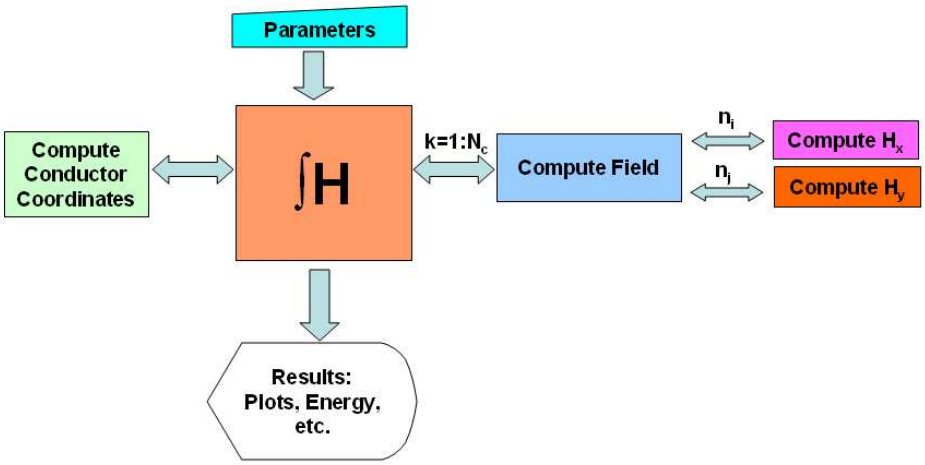

Figure B.1: Data flow between Matlab modules created to calculate energy and field distribution in a core window.

Int_H()

```
clear
time = cputime;

%Set the parameters, and declare them as global
Param_Decl;

%Compute the centers of each conductor inside the window
P_Centers = Compute_P_Centers();

if(nsc > 0)
    S_Centers = Compute_S_Centers();
else
    S_Centers = -inf;
end
```

```
if(ntc > 0)
    T_Centers = Compute_T_Centers();
else
    T_Centers = -inf;
end

%Area of integration
xorg = 0;
xend = cww;
yorg = 0;
yend = cwh;

%Number of intervals
M = 30;
N = ceil(cwh/cww*M);
%step size
xstep = (xend-xorg)/(M-1);
ystep = (yend-yorg)/(N-1);

%Create a structure to store data in
Hmag = cell(M,N);

x = xorg;
for i = 1:M
    y = yorg;
    for j = 1:N

    H_Primary = Compute_Field(x,y, P_Centers,pcw, pch, npc, ...
        cww, cwh);
    H_Secondary = Compute_Field(x,y, S_Centers, scw, sch, nsc, ...
        cww, cwh);
    H_Tertiary = Compute_Field(x,y, T_Centers, tcw, tch, ntc, ...
        cww, cwh);

    Hx = H_Primary(1) - npc/(nsc+ntc)*H_Secondary(1) ...
        - npc/(nsc+ntc)*H_Tertiary(1);
    Hy = H_Primary(2) - npc/(nsc+ntc)*H_Secondary(2) ...
        - npc/(nsc+ntc)*H_Tertiary(2);

    Hmag(i,j) = {sqrt(Hx^2 + Hy^2)};

    y = y + ystep;
```

```
    end
    x = x + xstep;
end
     H = cell2mat(Hmag)';

     xplot = xorg:xstep:xend;
     yplot = yorg:ystep:yend;
     figure(1);
     contour(xplot,yplot,H,50);
     colorbar;
     xlabel('Distance, m');
     ylabel('Distance, m');
     Title('Field Distribution');
     grid;

    %Calculate Energy
    Sum = 0;
    for i=2:N
        for j=2:M
             Sum = Sum + ((H(i,j)^2+H(i-1,j)^2+H(i,j-1)^2 ...
             +H(i-1,j-1)^2))/4;
        end
    end
   EnergyXY = Sum*0.5*pi*4e-7*xstep*ystep
   Energy = EnergyXY*(2*clw+2*clh+2*pi*(it+pcw))*2

    figure(2);
    plot(xplot,H(ceil(N/2),:),'LineWidth',3);
    grid;
    xlabel('Distance along x, m');
    ylabel('Field Strength, A/m');
    title('Field distribution using analytical method');

    figure(3);
    plot(yplot,H(:,ceil(M/2)),'LineWidth',3);
    grid;
    xlabel('Distance along the y, m');
    ylabel('Field Strength, A/m');
    title('Field distribution using analytical method');

sim_time = cputime-time
```

Compute_P_Centers()

```
function P_Centers = Compute_P_Centers()
Param_Decl;

for i=1:ceil(npc/2)
    P_Centers(i,1) = pcw/2 + it;
    P_Centers(i,2) = pch/2 + (i-1)*(pch+pcs) + dep;
end

for j=(ceil(npc/2)+1):npc
    P_Centers(j,1) = cww - it - pcw/2;
    P_Centers(j,2) = cwh - dep - pch/2 - ...
        (j - ceil(npc/2) - 1)*(pch+pcs);
end



end
```

Compute_S_Centers()

```
function S_Centers = Compute_S_Centers()
Param_Decl;

for i=1:nsc
    S_Centers(i,1) = scw/2 + it;
    S_Centers(i,2) = cwh - des - sch/2 ...
        - (i-1)*(sch + scs);
end


end
```

Compute_T_Centers()

```
function T_Centers = Compute_T_Centers()
Param_Decl;

for i=1:ntc
    T_Centers(i,1) = cww - tcw/2 - it;
    T_Centers(i,2) = tch/2 + dety + (i-1)*(tch + tcs);
end
```

```
end
```

Compute_Field()

```
function H_Field = Compute_Field(xp,yp, Centers, cw, ch, ...
    nc, cww, cwh)

% Param_Decl;
a = cw/2;
b = ch/2;
ur = 1000;
Hxt = 0;
Hyt = 0;

if(nc > 0)
for i = 1:nc

    xc = Centers(i,1);
    yc = Centers(i,2);

    x = xp - xc;
    y = yp - yc;

    Hx = ComputeX(x,y,a,b);
    Hy = ComputeY(x,y,a,b);



       %West Image
        xi = x+2*xc;

        Hxw = (ur-1)/(ur+1)*ComputeX(xi,y,a,b);
        Hyw = (ur-1)/(ur+1)*ComputeY(xi,y,a,b);


        %East Image
         xi = x-2*(cww-xc);

        Hxe = (ur-1)/(ur+1)*ComputeX(xi,y,a,b);
        Hye = (ur-1)/(ur+1)*ComputeY(xi,y,a,b);

        %North Image
```

```
yi = y-2*(cwh-yc);

Hxn = (ur-1)/(ur+1)*ComputeX(x,yi,a,b);
Hyn = (ur-1)/(ur+1)*ComputeY(x,yi,a,b);


%South Image
yi = y+2*yc +;

Hxs = (ur-1)/(ur+1)*ComputeX(x,yi,a,b);
Hys = (ur-1)/(ur+1)*ComputeY(x,yi,a,b);


%Northwest Image
xi = x+2*xc ;
yi = y-2*(cwh-yc);

Hxnw = -(ur-1)/(ur+1)*ComputeX(xi,yi,a,b);
Hynw = -(ur-1)/(ur+1)*ComputeY(xi,yi,a,b);

  %Northeast Image
xi = x-2*(cww-xc);
yi = y-2*(cwh-yc);
Hxne = -(ur-1)/(ur+1)*ComputeX(xi,yi,a,b);
Hyne = -(ur-1)/(ur+1)*ComputeY(xi,yi,a,b);


%Southeast Image
xi = x-2*(cww-xc);
yi = y+2*yc;

Hxse = -(ur-1)/(ur+1)*ComputeX(xi,yi,a,b);
Hyse = -(ur-1)/(ur+1)*ComputeY(xi,yi,a,b);


%Southwest Image
xi = x+2*xc;
yi = y+2*yc;
Hxsw = -(ur-1)/(ur+1)*ComputeX(xi,yi,a,b);
Hysw = -(ur-1)/(ur+1)*ComputeY(xi,yi,a,b);


Hxt = Hxt+Hx+Hxw+Hxe+Hxn+Hxs+Hxnw+Hxne+Hxse+Hxsw;
```

```
        Hyt = Hyt+Hy+Hyw+Hye+Hyn+Hys+Hynw+Hyne+Hyse+Hysw;
end   %Close for i=1:npc

H_Field = [Hxt Hyt];
else
    H_Field = [0 0];
end

end  %close function
```

ComputeX()

```
function Hxc = ComputeX(x,y,a,b)
Hxc = 1/8/pi/a/b*(-(b-y)*(atan((a-x)/(b-y))+atan((a+x)/(b-y)))...
    +(b+y)*(atan((a+x)/(b+y))+atan((a-x)/(b+y)))...
    +(a-x)*log(sqrt((a-x)^2+(b+y)^2)/sqrt((a-x)^2+(b-y)^2))...
    +(a+x)*log(sqrt((a+x)^2+(b+y)^2)/sqrt((a+x)^2+(b-y)^2)));
end
```

ComputeY()

```
function Hyc = ComputeY(x,y,a,b)
Hyc = 1/8/pi/a/b*((a-x)*(atan((b-y)/(a-x))+atan((b+y)/(a-x)))...
    -(a+x)*(atan((b-y)/(a+x))+atan((b+y)/(a+x)))...
    +(b-y)*log(sqrt((a-x)^2+(b-y)^2)/sqrt((a+x)^2+(b-y)^2))...
    +(b+y)*log(sqrt((a-x)^2+(b+y)^2)/sqrt((a+x)^2+(b+y)^2)));
end
```

Appendix C

Experimental Setup

The extended cantilever model parameters were extracted experimentally as outlined in [44]. The setup used for the measurements of the model parameters and leakage inductance is shown in Fig. C.1. The equipment marked in the figure is listed in Table C.1.

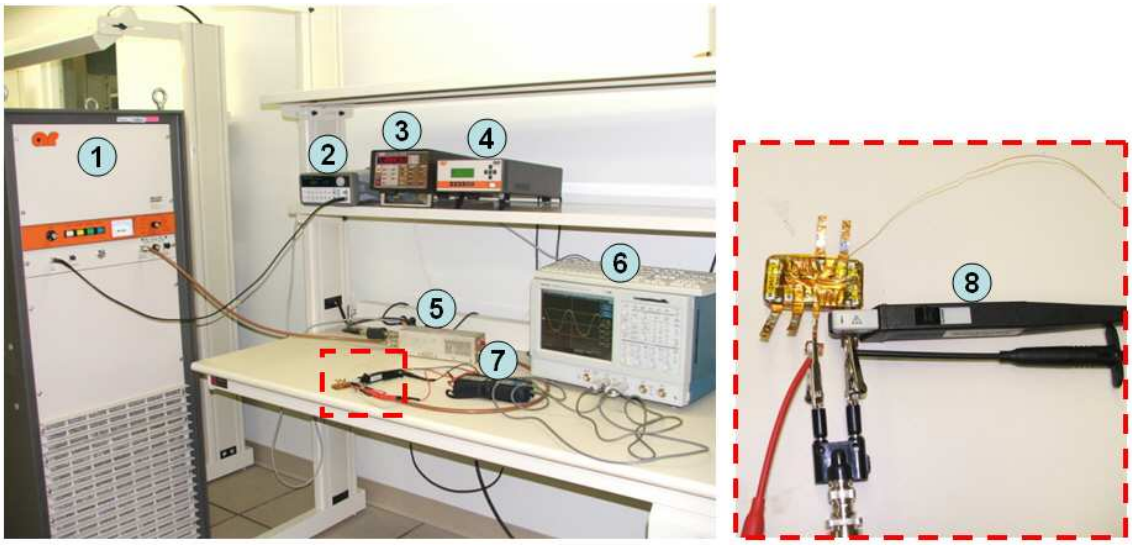

Figure C.1: Experimental setup used in extracting the parameters of the extended cantilever model.

Table C.1: List of major equipment used in the experiment.

Number	Equipment	Description
1	AR 1000L	Amplify Input Signal
2	Agilent 33120A	Generate Input Signal
3	Keithley 740	Monitor Core Temperature
4	AR PM2002	Monitor Amplifier Output Power
5	AR DC2500	Coupler to Sample Output Power
6	Tektronix TDS5054	Observe and measure waveforms
7	Tektronix P5205	Differential Voltage Probe
8	Tektronix TCP202	Current Probe

The equivalent circuit of the setup is given by Fig. C.2. A high-frequency amplifier was employed for the experimental measurements in order to ensure that

the ferrite core is excited at the rated operating condition of the transformer. Inadequate excitation leads to reduced effective permeability of the core, and subsequent decrease in inductance and magnetic coupling. However, saturation from overexcitation is also not desirable as it leads to a short-circuit condition of the core resulting in excessive losses. Further, the general rise in temperature also significantly impacts magnetic properties of the core. For these reasons, monitoring of the core temperature is done using a thermometer, and output power level of the amplifier using a power meter. A directional coupler is used to provide the scaled-down sample of the output power to the power meter.

Extreme care must be taken when using the RF amplifier. The amplifier is designed to supply any type of load, no matter how poor. Incorrect use can lead to damage to the equipment and personnel. So when using a transformer as the load, it is essential to verify that the load limit of the amplifier and cables is not exceeded. It might be necessary to place a resistive power load in series with the reactive load to ensure extreme voltages and currents are not encountered.

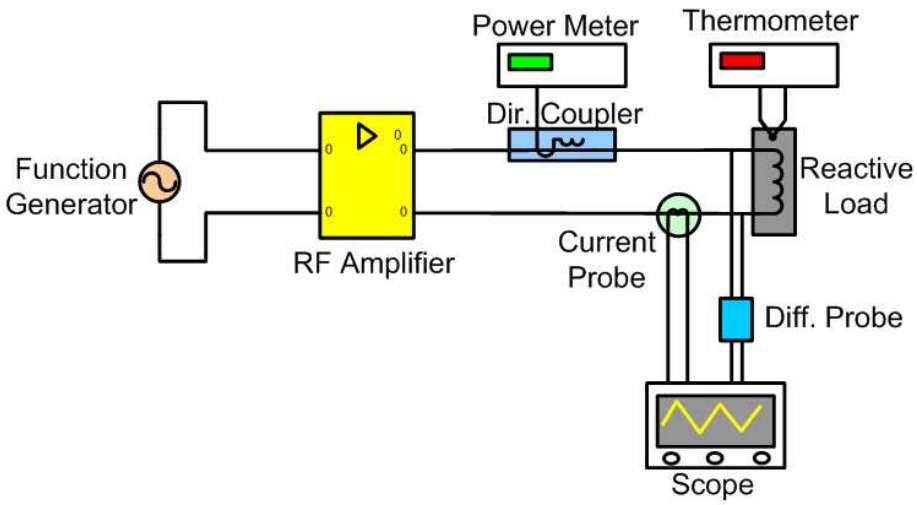

Figure C.2: The equivalent circuit configuration of the experimental setup.

The winding capacitance and small-signal leakage inductance was measured using the Agilent 4294A impedance analyzer with the 16047E test fixture, as depicted by Fig. C.3. The impedance analyzer has a rated bandwidth of 40Hz to 110MHz. The tests were performed with 20mA perturbations. The device connectors were kept as short as possible to minimize the amount of device-external parasitics from influencing the high-frequency measurements.

Figure C.3: Agilent 4294A with 16047E text fixture.

BIBLIOGRAPHY

[1] A. W. Lotfi and M. A. Wilkowski, "Issues and advances in high-frequency magnetics for switching power supplies," in *Proceedings of the IEEE*, vol. 89, pp. 833–845, June 2001.

[2] W. Chen, G. Hua, D. Sable, and F. C. Lee, "Design of high efficiency, low profile, low voltage converter with integrated magnetics," in *Proc. of IEEE Applied Power Electronics Conference and Exposition*, vol. 2, pp. 911–917, Feb 1997.

[3] J. A. Cobos, M. Rascon, L. Alvarez, S. Ollero, M. de Graf, and W. Waanders, "Low profile and low output voltage dc/dc converters for on-board power distribution using planar magnetics," in *Proc. of IEEE Industrial Application Society Conference*, vol. 2, pp. 1153–1158, Oct 1997.

[4] N. Dai, A. W. Lofti, C. Skutt, W. Tabisz, and F. C. Lee, "A comparative study of high-frequency, low-profile planar transformer technologies," in *Proc. of IEEE Applied Power Electronics Conference and Exposition*, vol. 1, pp. 226–232, Feb 1994.

[5] M. Gerber, J. A. Ferreira, I. W. Hofsajer, and N. Seliger, "A high-density heat-sink-mounted inductor for automotive applications," *IEEE Transactions on Industry Applications*, vol. 40, pp. 1031–1038, July 2004.

[6] R. Prieto, O. Garcia, R. Asensi, J. A. Cobos, and J. Uceda, "Optimizing the performance of planar transformers," in *Proc. of IEEE Applied Power Electronics Conference and Exposition*, vol. 1, pp. 415–421, March 1996.

[7] M. T. Quirke, J. J. Barrett, and M. Hayes, "Planar magnetic component technology-a review," *IEEE Transactions on Components, Hybrids, and Manufacturing Technology*, vol. 15, pp. 884–892, 1992.

[8] S. Ramakrishnan, R. L. Steigerwald, and J. A. Mallick, "A comparison study of low-profile power magnetics for high-frequency, high-density switching converters," in *Proc. of IEEE Applied Power Electronics Conference and Exposition*, vol. 1, pp. 388–394, Feb 1997.

[9] M. Sippola, *Developments for the high frequency power transformer design and implementation*. PhD thesis, Helsinki University of Technology, Espoo, Finland, 2003.

[10] M. Rascon, R. Prieto, O. Garcia, J. A. Cobos, and J. Uceda, "Design of very low profile magnetic components using flex foils," in *Proc. of IEEE Applied Power Electronics Conference and Exposition*, vol. 2, pp. 561–567, Feb 1997.

[11] C. Xiao, *Investigation of Fundamental Frequency Limitations of Passive Components for Very High Frequency Power Conversion*. PhD thesis, Virginia Polytechnic Institute and State University, Blacksburg, VA, July 2006.

[12] C. Quinn, K. Rinne, T. O'Donnell, M. Duffy, and C. O. Mathuna, "A review of planar magnetic techniques and technologies," in *Proc. of IEEE Applied Power Electronics Conference and Exposition*, vol. 2, pp. 1175–1183, March 2001.

[13] W. G. Odendaal, *A Generic Approach for the Modelling of High Power Density Magnetic Components*. PhD thesis, Rand Afrikaans University, 1997.

[14] W. J. Creamer, *Elements of Electrical Engineering*. McGraw-Hill Book Co., 1948.

[15] K. Wallace, "Multiple output planar transformer," *IBM Technical Disclosure Bulletin*, vol. 24, pp. –, Jan 1982.

[16] Anon., "Split plate transformer," *IBM Technical Disclosure Bulletin*, vol. 28, pp. 625–626, July 1985.

[17] Anon., "New magnetic structure for a low profile planar transformer," *IBM Technical Disclosure Bulletin*, pp. 4245–4247, March 1986.

[18] A. Estrov, "Power transformer design for 1 mhz resonant converter," *High Frequency Power Conversion Proceedings*, pp. 36–54, May 1986.

[19] R. Petkov, "Optimum design of a high-power high-frequency transformer," *IEEE Trans. on Power Electronics*, vol. 11, pp. 33–42, Jan 1996.

[20] W. A. Roshen, R. L. Steigerwald, R. Charles, W. Earls, G. Claydon, and C. F. Saj, "High efficiency, high density mhz magnetic components for a low profile converter," in *Proc. of IEEE Applied Power Electronics Conference and Exposition*, pp. 674–683, Feb 1992.

[21] W. G. Odendaal, J. Azevedo, G. W. Bruning, and R. M. Wolf, "A high-efficiency magnetic component with superior caloric performance for low-profile high-density power conversion," *IEEE Trans. on Industry Applications*, vol. 40, pp. 1287–1293, Oct. 2004.

[22] H. W. Ott, *Noise Reduction Techniques in Electronic Systems*. John Wiley and Sons, 2nd ed., 1988.

[23] K. L. Kaiser, *Electromagnetic Shielding*. Taylor and Francis Group, 2006.

[24] S. J. Chapman, *Electric Machinery and Power Systems Fundamentals*. Boston: Mc Graw Hill, 2002.

[25] P. G. Blanken and J. J. L. M. van Vlerken, "Modeling of electromagnetic systems," *IEEE Trans. on Magnetics*, vol. 27, pp. 4509–4515, Nov. 1991.

[26] R. W. Buntenbach, "Analogs between magnetic and electrical circuits," *Electronic Products*, pp. 108–113, Oct 1969.

[27] J. J. L. M. van Vlerken and P. G. Blanken, "Lumped modeling of rotary transformers, heads and electronics for helical-scan recording," *IEEE Trans. on Magnetics*, vol. 31, pp. 1050–1055, March 1995.

[28] A. Schellmanns, P. Fouassier, J. P. Keradec, and J. L. Schanen, "Equivalent circuits for transformers based on one-dimensional propogation: Accounting for multilayer structure of windings and ferrite losses," *IEEE Trans. on Magnetics*, vol. 36, pp. 3778–3784, Sep. 2000.

[29] B. Cogitore, J. P. Keradec, and J. Barbaroux, "The two-winding transformer: an experimental method to obtain a wide frequency range equivalent circuit," *IEEE Trans. on Instrumentation and Measurement*, vol. 43, pp. 364–371, April 1994.

[30] P. G. Blanken, "A lumped winding model for use in transformer models for circuit simulation," *IEEE Trans. on Power Electronics*, vol. 3, pp. 445–460, May 2001.

[31] F. Blache, J. P. Keradec, and B. Cogitore, "Stray capacitances of two winding transformers: equivalent circuit, measurements, calculation and lowering," in *Proc. of IEEE Industry Applications Society*, vol. 2, pp. 1211–1217, Oct. 1994.

[32] L. Dalessandro, W. G. Odendaal, and J. W. Kolar, "Hf characterization and non-linear modeling of a gapped toroidal magnetic structure," in *Proc. of IEEE Power Electronics Specialists*, pp. 1520–1527, June 2005.

[33] B. D. H. Tellegen, "The gyrator, a new electric circuit element," *Phillips Res. Rep.*, vol. 3, pp. 81–101, April 1948.

[34] R. W. Erickson and D. Maksimovic, "A multiple-winding magnetics model having directly measurable parameters," in *Proc. of IEEE Power Electronics Specialists Conference*, pp. 1472–1478, May 1998.

[35] Q. Chen, F. C. Lee, J. Z. Jiang, and M. M. Jovanovic, "A new model for multiple-winding transformer," in *Proc. of IEEE Power Electronics Specialists Conference*, vol. 2, pp. 864–871, June 1994.

[36] P. L. Dowell, "Effects of eddy currents in transformer windings," in *Proc. of Inst. Elect. Eng.*, vol. 113, pp. 1387–1394, Aug. 1966.

[37] A. D. Podoltsev, I. N. Kucheryavaya, and B. B. Lebedev, "Analysis of effective resistance and eddy-current losses in multiturn winding of high frequency magnetic components," *IEEE Trans. on Magnetics*, vol. 39, pp. 539–548, Jan. 2003.

[38] J. P. Keradec, E. Laveuve, and J. R. Roudet, "Multipolar development of vector potential for parallel wires. application to the study of eddy currents effects in transformer windings," *IEEE Trans. on Magnetics*, vol. 27, pp. 4242–4245, Sep. 1991.

[39] C. R. Sullivan, "Computationally efficient winding loss calculation with multiple windings, arbitrary waveforms, and two-dimensional or three-dimensional field geometry," *IEEE Trans. on Power Electronics*, vol. 16, pp. 142–149, Jan. 2001.

[40] J. A. Ferreira, "Appropriate modelling of conductive losses in the design of magnetic components," in *Proc. of Power Electronics Specialist Conference*, pp. 780–785, June 1990.

[41] J. Ferreira, "Analytical computation of ac resistance of round and rectangular litz wire windings," in *Proc. of IEE*, vol. 139, pp. 21–25, Jan 1992.

[42] G. R. Skutt and F. C. Lee, "Characterization of dimensional effects in ferrite-core magnetic devices," in *Proc. of Power Electronics Specialists Conference*, vol. 2, pp. 1435–1440, June 1996.

[43] B. Carsten, "High frequency conductor losses in switchmode magnetics," in *Tech. Papers of the 1st Int. High Frequency Power Conversion Conf.*, pp. 155–176, May 1986.

[44] R. W. Erickson and D. Maksimovic, *Fundamentals of Power Electronics*. Kluwer Academic Publishers, 2nd ed., 2001.

[45] P. Nakmahachalasint, K. D. T. Ngo, and L. Vu-Quoc, "Thermal behavior of a dynamic domain-wall motion model for hysteresis in power ferrites," *IEEE Trans. on Magnetics*, vol. 41, pp. 140–143, Jan. 2005.

[46] Ferroxcube, *Data Sheet: 3F45 Preliminary material specification*, Sep 2004.

[47] S. A. Mulder, "Loss formulas for power ferrites and their use in transformer design," tech. rep., Philips Components, Eindhoven, 1994.

[48] M. Albach, T. Durbaum, and A. Brockmeyer, "Calculating core losses in transformers for arbitrary magnetizing currents: a comparison of different approaches," in *Proc. of IEEE Power Electronics Specialists Conference*, vol. 2, pp. 1463–1468, June 1996.

[49] M. N. Ozisik, *Heat Conduction*. New York: John Wiley & Sons, 2nd ed., 1993.

[50] Ferroxcube, *Ferrite Materials Survey*, Sep 2004.

[51] M. T. Johnson and E. G. Visser, "A coherent model for the complex permeability in polycrystalline ferrites," *IEEE Trans. on Magnetics*, vol. 26, pp. 1987–1989, Sept. 1990.

[52] T. A. Driscoll and L. N. Trefethen, *Schwarz-Christoffel Mapping*. Cambridge University Press, 2002.

[53] H. Urkowitz, "Capacitance between thin film conductors deposited on a high-dielectric-constant substrate," in *Proc. of IRE*, vol. 50, pp. 2142–2143, - 1962.

[54] L. Zhao and J. D. van Wyk, "Wideband modeling of integrated power passive structures: The series resonator," *IEEE Trans. on Power Electronics*, vol. 19, pp. 523–530, March 2004.

[55] Texas Instruments, *Magnetics Design Handbook*, 2001.

[56] D. A. de Wolf, *Essentials of Electromagnetics for Engineering*. Cambridge, UK: Cambridge University Press, 2001.

[57] K. J. Binns, P. J. Lawrence, and C. W. Trowbridge, *The Analytical and Numerical Solution of Electric and Magnetic Fields*. John Wiley and Sons, 1992.

[58] J. A. Ferreira, *Electromagnetic Modelling of Power Electronic Converters*. Boston: Kluwer Academic Publisher, 1989.

[59] D. Magot, X. Margueron, and J. P. Keradec, "Peec-like analytical calculation of static leakage inductance of h.f. transformers," in *Proc. of IEEE Industry Applications Society Conference*, vol. 1, pp. 538–545, Oct. 2004.

[60] D. Maksimovic, R. Erickson, and C. Griesbach, "Modeling of cross-regulation in converters containing coupled inductors," in *Proc. of IEEE Applied Power Electronics Conference*, pp. 350–356, Feb 1998.

[61] Ansoft Corporation, *Maxwell Online Help System*, 1995-2004.

[62] S. Wang, R. Chen, J. D. van Wyk, F. C. Lee, and W. G. Odendaal, "Developing parasitic cancellation technologies to improve emi filter performance for switching mode power supplies," *IEEE Trans. on Electromagnetic Compatibility*, vol. 47, pp. 921–929, Nov. 2005.

[63] S. Wang, F. C. Lee, W. G. Odendaal, and J. D. van Wyk, "Improvements of emi filter performance with parasitic coupling cancellation," *IEEE Trans. on Power Electronics*, vol. 20, pp. 1221–1229, Sept. 2005.

[64] R. B. Schulz, V. C. Plantz, and D. R. Brush, "Shielding theory and practice," *IEEE Trans. on Electromagnetic Compatability*, vol. 30, pp. 187–201, Aug 1988.

[65] S. Wang, "Modeling and design of planar integrated magnetic components," Master's thesis, Virginia Polytechnic Institute and State University, Blacksburg, VA, July 2003.

[66] J. T. Strydom, J. A. Ferreira, J. D. van Wyk, I. W. Hoffajer, and E. Waffenschmidt, "Power electronic subassemblies with increased functionality based on planar sub-components," in *Proc. of IEEE Power Electronics Specialists Conference*, vol. 3, pp. 1273–1278, June 2000.

[67] D. van der Linde, C. A. M. Boon, and J. B. Klaassens, "Design of a high-frequency planar power transformer in multilayer technology," *IEEE Transactions on Industrial Electronics*, vol. 38, pp. 135–141, 1991.

[68] K. D. T. Ngo, R. P. Alley, and A. J. Yerman, "Fabrication method for a winding assembly with a large number of planar layers," *IEEE Transactions on Power Electronics*, vol. 8, pp. 55–61, Jan 1993.

[69] K. I. Arshak, A. Ajina, and D. Egan, "Development of screen-printed polymer thick film planar transformer using mn-zn ferrite as core material," *Microelectronics Journal*, vol. 32, pp. 113–116, 2001.

[70] P. M. Gradzki and F. C. Lee, "Design of high-frequency hybrid power transformer," in *Proc. of IEEE Applied Power Electronics Conference and Exposition*, pp. 319–326, Feb 1988.

[71] A. Lotfi, R. B. V. Dover, L. Schneemeyer, and M. Steigerwald, "Microtransformer devices using thin-film electroplated deposition," in *Proc. of IEEE Power Electronics Specialists Conference*, vol. 2, pp. 1511–1515, May 1998.

[72] M. Xu, T. M. Liakopoulos, C. H. Ahn, S. H. Han, and H. J. Kim, "A microfabricated transformer for high-frequency power or signal conversion," *IEEE Transactions on Magnetics*, vol. 34, pp. 1369–1371, July 1998.

[73] Y. Taniguchi, T. Yoshihara, and T. Tsukada, "Copper/titanium dioxide thick film and application for through-hole," in *Proc. of Electronics Components Conference*, pp. 589–595, May 1988.

[74] A. Sakamoto, S.-C. Chen, H. Tamura, M. Yoshimaru, and M. Ino, "Limitation of sputtered adhesion layer thickness for blanket cvd w in very high aspect contact filling," in *Proc. of VLSI Multilevel Interconnection Conference*, pp. 338–340, June 1991.

[75] M. Modi and S. K. Sitaraman, "Effects of adhesive layer properties on interfacial fracture in thin-film high-density interconnects," in *Proc. of Electronic Components and Technology Conference*, pp. 847–853, May 2002.

[76] M. Ueki, M. Hiroi, N. Ikarashi, T. Onodera, N. Furutake, N. Inoue, and Y. Hayashi, "Effects of ti addition on via reliability in cu dual damascene interconnects," *IEEE Trans. on Electron Devices*, vol. 51, pp. 1883–1891, Nov 2004.

Vita

Anish Prasai was born in the small, mountainous country of Nepal on December 3, 1981. He moved with his family to the State of Virginia when he was about 9 years old. The author's attraction to engineering was made apparent at an early age when he was observed breaking open his toys in order to figure out how they functioned. It was not until much later that he eventually figured out how to put them back together in a working order again.

The author's affinity towards electrical engineering developed academically in the latter half of his high school years. Upon entry to Virginia Tech in Fall of 2000, his attraction towards the field electrical engineering was at full bloom. The author completed his B.S. degree in Electrical Engineering in the Spring of 2004. Through his electives, he chose to specialize in the field of power electronics. He decided to continue his studies towards a Master's degree in Electrical Engineering in Fall of 2004 with the Center for Power Electronics System at Virginia Tech.